Dissertation

submitted to the

Combined Faculty of Natural Sciences and Mathematics

of Heidelberg University, Germany

for the degree of

Doctor of Natural Sciences

Put forward by

Niklas Müller

born in Heilbronn

Oral examination: 30.7.2020

Multimodal microscopy in mid-infrared

via flexible pulse shaping

Referees: Prof. Dr. Annemarie Pucci

PD Dr. Robert Moshammer

Abstract:

In this thesis, mid-infrared (MIR) pulses with arbitrary temporal and spectral shape are generated via a difference-frequency process for application in a non-linear Raman microscope. Solely by shaping the sub 10 fs driving pulses, the broadband spectra of the MIR pulses are switched to narrowband and tuneable ones. In MIR transmission spectroscopy, these narrowband MIR spectra allow for investigating molecular vibrations from 1250 to 3250 cm^{-1} with spectral resolutions below 20 cm^{-1}. Furthermore, MIR transmission microspectroscopy is combined with coherent-anti-Stokes Raman scattering (CARS) to provide a direct comparison of spectra and images obtained in one spot of the sample. Sum-frequency (SF) microspectroscopy is an additional technique, which complements the toolbox of this non-linear Raman microscope with the potential to investigate non-centrosymmetric systems. The flexibility of the pulse shaper allows for implementing two different SF-methods. Whereas the heterodyne multiplex method acquires the whole SF spectrum by imprinting only three different phase functions, the homodyne MIR-scanning method generates a high SF intensity directly linked to one vibrational mode. In all applications, the phase of MIR pulses must be well-known. This phase is determined in the focal plane of the microscope over more than 1000 cm^{-1} via two methods based on the dispersion-scan.

Zusammenfassung:

Diese Arbeit behandelt die Erzeugung von Mittelinfrarotimpulsen (MIR-Impulsen) mit beliebig einstellbarer zeitlicher und spektraler Form mittels eines Differenzfrequenzprozesses und ihre Anwendung in einem nichtlinearen Ramanmikroskop. Nur durch das Umformen der sub 10 fs Erzeugerimpulse mithilfe eines Impulsformers wird aus dem breitbandigen Spektrum der MIR-Impulse ein schmalbandiges und durchstimmbares. In der MIR-Transmissionsspektroskopie ermöglicht dieses schmalbandige MIR Spektrum die Untersuchung von Molekülvibrationen in einem Bereich von 1250cm^{-1} bis zu 3250 cm^{-1} mit einer spektralen Auflösung unter 20 cm^{-1}. Des Weiteren gelingt durch die Kombination der MIR-Transmissionsmikrospektroskopie mit kohärenter anti-Stokes Raman Streuung (CARS) der direkte Vergleich von Spektren und Bildern, da diese an der gleichen Probenstelle aufgenommen werden. Das Hinzufügen der Summenfrequenz- (SF) Mikrospektroskopie erweitert das Repertoire dieses nichtlinearen Ramanmikroskops um die Option auch nichtzentrosymmetrische Proben zu untersuchen. Die Flexibilität des Impulsformers ermöglicht die Implementierung zweier unterschiedlicher SF-Methoden. Wohingegen die heterodyne-multiplex-Methode das ganze SF-Spektrum beim Anlegen von nur drei unterschiedlichen Phasenfunktionen detektiert, erzeugt die homodyne MIR-scanning-Methode eine hohe SF-Intensität, welche direkt auf eine Vibrationsbande zurückgeführt werden kann. Für alle Anwendungen muss die Phase der MIR-Impulse vorab bekannt sein. Diese wird in der Fokalebene des Mikroskops in einem Bereich von mehr als 1000 cm^{-1} mittels zweier unterschiedlicher Methoden bestimmt, die beide auf der Dispersions-Scan-Methode beruhen.

Contents

I. Motivation and introduction

Since its invention in the 17th century, microscopy has been the foundation of an enormous number of applications in various research fields. These applications have been accompanied by the continuous development of new techniques improving the visualisation of increasingly smaller objects as well as improving the sensitivity to more and more specimens.

The invention of fluorescence microscopy was a milestone, especially in life sciences, because it offers unprecedented access to the individual building blocks of various samples. Fluorescence microscopy is done by staining each building block with a specific fluorescent label and detecting the high intensities of the emitted fluorescent light (Figure I.1a) [4]. These labels also allow for improved spatial resolution beyond the Abbe limit via the stimulated emission depletion method (STED) [5] or the stochastic optical reconstruction microscopy method (STORM) [6]. Recently, a resolution of 1 nm was even achieved [7].

Fluorescence microscopy is broadly applied for the investigation of samples whose building blocks and their behaviours in the staining process are well-known. However, applying this type of microscopy to new samples is more challenging since the information how to stain all the different building blocks is missing. Furthermore, it is possible that samples may be distorted during the labelling process. The use of fluorescent labels can be overcome by exploiting the intrinsic properties of the sample itself, which provide not only a contrast in imaging but also the potential to detect small structural changes of their molecules.

Vibrational spectroscopy permits label-free access to molecules either through the direct excitation of vibrational modes in mid-infrared (MIR) transmission spectroscopy or by Raman spectroscopy, which probes the vibrational modes in an inelastic scattering (Figure I.1b & c) [8, 9]. Both methods provide access to vibrational modes over a broad spectral range via their linear interaction. Furthermore, information about the vibrational modes can also be obtained with spatial resolution when using Raman microscopy, as shown in various applications [10-12]. Recently, even MIR transmission microscopy has been implemented using novel light sources and sophisticated techniques [13-15]. However, both methods have several drawbacks. Poor spatial resolution and technical difficulties such as the lack of intense light sources are the main handicaps in MIR transmission, while the low signal levels in Raman spectroscopy prevent fast data acquisition.

Coherent Raman anti-Stokes scattering (CARS) is a powerful tool for providing vibrational contrast as well as high signals [16, 17]. This spectroscopic technique gives access to the information about molecular vibrations via coherent Raman excitations in a four-wave mixing process (Figure I.1d). In contrast with Raman, CARS benefits from several advantages such as the generation of much higher signal levels, which have even led to imaging with video frame rate [18]. Furthermore, the application of CARS in microscopy offers high spatial resolution and the potential to represent objects in 3D due to the generation of CARS signals only within a small spatial volume [19]. Another principal advantage of CARS microscopy is that other nonlinear signals are simultaneously generated in this small spatial volume. Despite having no access to spectral information, each of these

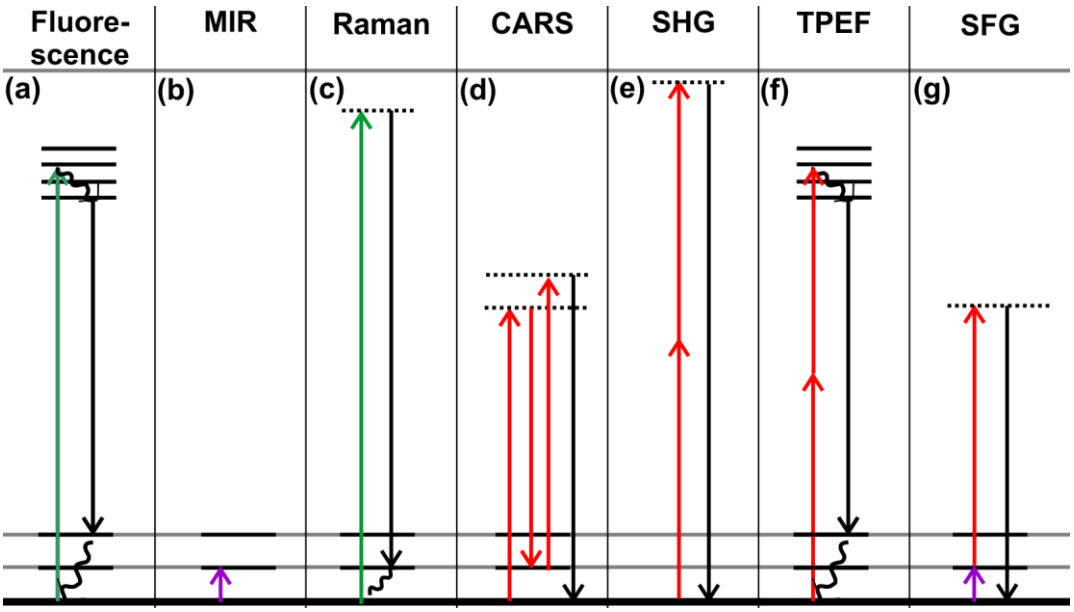

Figure I.1 Energy diagrams of the most common linear and non-linear interactions in spectroscopy and microscopy. The light emitting transitions are depicted in black. The transitions driven by light with a wavelength in the NIR and MIR range are depicted in red and purple, respectively. The transitions in the visible are shown in green. (SHG: second-harmonic generation, TPEF: two-photon excited fluorescence, SFG: sum-frequency generation)

signals provides essential information in microscopy by imaging specific types of molecules. Second-harmonic and two-photon excited fluorescence light, for example, are only generated by non-centrosymmetric systems and chromophores, respectively (Figure I.1e & f). The combination of all information obtained from these different signals is called multimodal microscopy [20, 21].

The success of multimodal microscopy has increased tremendously in the last years. Several applications in life sciences have been developed, such as determining skin diseases using a compact CARS tomography setup [22]. Another example is the tracking of neural activities in the brain by widefield multimodal microscopy [23]. Furthermore, the potential for providing real-time imaging during surgeries has been shown by endoscopes that can simultaneously acquire CARS, second-harmonic, and two-photon excited fluorescence images [24].

The crucial experimental issue in multimodal microscopy is the implementation of CARS because the other signals are additionally generated without any further effort. CARS microscopy is usually done using two different laser pulses with narrowband spectra in the near-infrared (NIR) range. The two pulses have slightly detuned spectra to generate the CARS signal of a specific vibrational mode. In order to acquire the whole CARS spectrum, one of the two NIR spectra is shifted. These laser pulses are generated either by optical parametric oscillators (OPO) or by fibre laser systems, which have both experienced great technical progress in the last years [25-28]. Recently developed OPO systems allow even for tuning the wavelength within milliseconds [29]. However, these setups are quite complex and static. Special care, for example, is required in order to provide a stable temporal synchronisation and a perfect spatial overlap of the two laser pulses. Furthermore,

a change of the spectral tuning range is only accomplished by replacing the whole OPO or fibre system.

A way to overcome these drawbacks is by applying a different laser source to excite all molecular vibrations and nonlinear interactions without any wavelength tuning. Sub 10 fs laser pulses are the key in this regard due to their broad spectra spanning over 3000 cm^{-1}, which gives access to all molecular vibrations ranging from the fingerprint region up to the CH stretching. Furthermore, all nonlinear interactions benefit from the high instantaneous power of the ultrashort laser pulses. For spectroscopy, however, these laser pulses cannot be used without any further effort due to the indistinguishability and spectral overlap of the generated signals.

The spectral resolution is accomplished by inserting a programmable pulse shaper inside the setup and shaping these ultrabroadband laser pulses (Figure I.2a). In pulse shaping, arbitrary phase and amplitude functions are imprinted on the laser pulses to adjust their spectral and temporal distribution. These shaped laser pulses are exploited in CARS spectroscopy in order to control the excitation of vibrational modes [30-32]. With the appropriate phase function, the excitation of many vibrations can be narrowed down to only one specific mode. A simple switch of the phase function is enough to tune this narrowband excitation. In recent years, several methods have been developed to flexibly adapt the laser pulses for specific tasks. The sensitivity to vibrational modes with a small cross section, for example, is significantly increased by using a heterodyne detection method [33]. Other methods have demonstrated phase-sensitive [34], time-resolved [35, 36], and multiplex [37] CARS spectroscopy. Moreover, the combination of several non-linear interactions benefits from flexible pulse shaping. Pulse shaping can adapt the laser pulses simultaneously to all

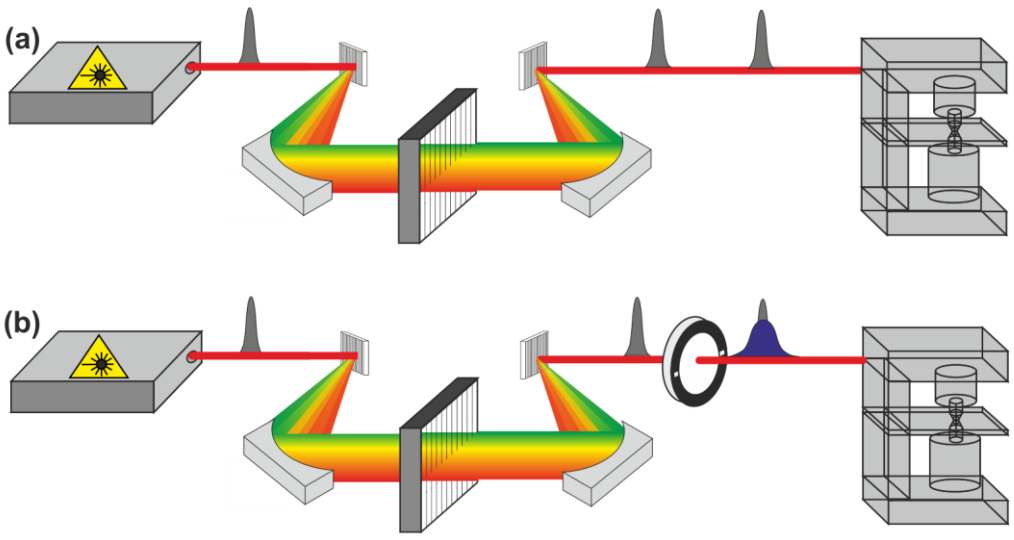

Figure I.2 Flexible pulse shaping for multimodal microscopy. (a) CARS, second-harmonic and two-photon excited fluorescence imaging is provided by using arbitrary shaped, ultrabroadband NIR pulses in a microscope. The programmable pulse shaper controls the non-linear processes by tailoring the laser pulses. (b) An additional non-linear crystal allows the generation of shaped MIR pulses in a difference-frequency (DF) process by the shaped NIR pulses. By guiding both laser pulses inside the microscope, MIR transmission and SF microspectroscopy is possible.

interactions by tailoring its different spectral parts. One spectral part, for example, generates high second-harmonic signals with short pulses and the other part achieves spectral resolution in the CARS [35].

Despite its great success, multimodal microscopy in general, and its shaper-based implementation in particular, has been faced with several challenges. One of the main challenges is the acquisition of CARS spectra in the important fingerprint region due to the small cross sections of the vibrational modes in that region. Furthermore, the nonlinearity of the CARS process generates a non-resonant background, which distorts vibrational modes through interferences. This non-resonant background is highly dependent on the experimental setup used and therefore hinders a direct comparison of the CARS spectra obtained under different experimental conditions.

In this thesis, a new MIR light source is developed which addresses each of the drawbacks in CARS by exploiting new spectroscopic techniques. MIR transmission microspectroscopy, for example, makes it possible to investigate molecular vibrations without any background. In contrast to CARS, a direct comparison of these background-free spectra to the vast number of references in the literature is possible. Furthermore, the MIR transmission microspectroscopy is much more sensitive and provides a determination of vibrational modes in the fingerprint region via the broad spectral range of the new MIR light source.

Another highlight of this new MIR light source is its potential to provide a variety of different MIR pulses in a robust and complex setup. This is accomplished by generating the MIR pulses in a difference-frequency (DF) process using shaped NIR pulses. By controlling the MIR generation, MIR pulses with arbitrary spectral and temporal distributions can be generated with nothing more than an additional nonlinear crystal (Figure I.2b). Therefore, the spectroscopic repertoire in this shaper-based setup is complemented without any loss of simplicity. In particular, this has the advantage of combining the MIR transmission and CARS microspectroscopy. Spectra and images obtained with both methods at the same position in the sample can be directly compared.

Sum-frequency (SF) microspectroscopy is an additional vibrational sensitive method, which completes the toolbox of this shaper-based microscopy setup (Figure I.1g). This method has the potential to obtain information about molecular vibrations in non-centrosymmetric systems using NIR and MIR pulses. In contrast to CARS, the structure of samples such as monolayers, interfaces, and crystals can be determined without the interference of the dense isotropic surrounding [38-41]. Furthermore, it overcomes the low spatial resolution of MIR microscopy with its dependence on the NIR laser pulse [42-45]. The advantages of SF microscopy are usually obtained at the price of a more complex setup, as it uses two different laser pulses. However, the arbitrary pulse shaping in this shaper-based setup enables simple and flexible implementation, which allows for controlling the excitation in SF spectroscopy.

The development and application of the new MIR light source in a multimodal microscopy setup is a crucial step towards developing a laser tool which can drive all kinds of non-linear interactions in shaper-based multimodal microscopy. This thesis presents this new MIR light source in the following chapters:

- In **chapter II,** the basic concepts about laser pulses and pulse shaping are summarised. Furthermore, the theoretical backgrounds of MIR generation, CARS, and SF spectroscopy are introduced. Finally, pulse shaping in non-linear spectroscopy and the spectral focusing concept generating a narrowband excitation in CARS are introduced.
- The flexible pulse shaping is demonstrated in a nonlinear microscopy setup, which consists of a laser, pulse shaper and microscope (see Figure I.2a). This is experimentally realised in this work by a Ti:Sa oscillator and a liquid crystal pulse shaper as described in **chapter III**. Especially, the implementation of the pulse shaper in a 4f setup and its operation principle is explained.
- In **chapter IV**, the generation of MIR pulses with broadband and narrowband MIR spectra are discussed. Furthermore, the tuning range and spectral width of these narrowband spectra are experimentally determined and compared to simulations.
- As described in **chapter V**, the NIR and MIR laser pulses can be applied in combined CARS and MIR microspectroscopy. This is demonstrated by detecting the vibrational resonances of polymers and alkynes. Furthermore, the potential of CARS and MIR microscopy is demonstrated using an example from the life sciences. Finally, the spatial resolution of the new MIR light source is determined.
- In **chapter VI**, SF microspectroscopy is implemented via two different shaping methods. In a homodyne MIR-scanning method, narrowband MIR spectra are exploited to acquire SF spectra and vibrational resonant SF images. By contrast, the whole SF spectrum is obtained in only three shots using the heterodyne multiplex method.
- The success of flexible pulse shaping is highly dependent on the knowledge of the spectral phase. The recently developed d-scan method [46] has the potential to retrieve this phase, as has already been shown in many applications. However, it has not been applied in the MIR range. In order to accomplish a MIR phase retrieval, two different d-scan based method are presented in **chapter VII**.
- The potential of arbitrary pulse shaping for the MIR generation and multimodal microscopy is summarised in **chapter VIII**. This chapter highlights the advantages of the new MIR light source and discusses several potential improvements for future development.

II. Concepts in pulse shaping and nonlinear spectroscopy

This chapter gives information about the theoretical background, which is essential to understand the presented concepts and experiments of this work. At the beginning, the principles of ultrashort laser pulses are summarized and a general approach of pulse shaping is explained (section 1).

In section 2, the fundamentals of non-linear optics are described and the theoretical background of MIR generation is discussed with respect to phase matching and conversion efficiency. Furthermore, the spectroscopic techniques SF and CARS are introduced in detail.

Section 3 presents the implementation of non-linear spectroscopy using ultrashort laser pulses. Solely by shaping these laser pulses, a spectral resolution is gained. One powerful shaping concept is spectral focusing. Aside its theory, the implementation of this concept in different setups is discussed, and an extension called tailored spectral focusing is introduced.

1. Ultrashort laser pulses

1 i. Description of laser pulses

The application of nonlinear spectroscopy have increased tremendously by the technical progress of pulsed laser sources [20, 47, 48]. Nowadays, there is a broad range of laser sources with different specifications in wavelength, pulse length and power. The wavelength ranges from the XUV down to the THz regime and a temporal width of the laser pulses from the picosecond down to the attosecond regime is available [49-51]. Recently, even peak powers of 2 GW have been demonstrated for 200 fs mid-infrared (MIR) laser pulses [52].

Laser pulses with a linear polarization are described by an real electric field $E(t)$ having a slowly varying envelope $E_0(t)$, a carrier angular frequency ω_0 and a phase factor $\phi(t)$. [53]:

$$E(t) = \mathrm{Re}\{\tilde{E}(t)\} = \mathrm{Re}\left\{E_0(t)e^{i(\omega_0 t - \phi(t))}\right\}. \qquad \text{II.1}$$

Beside its description in time domain, the equivalent information is provided by the electric field in frequency domain. The Fourier transform transfers the electric field $\tilde{E}(t)$ from time representation into the frequency space $\tilde{E}(\omega)$ (eq. II.2). The inverse Fourier transform (II.3) permits a transformation back into the time domain (eq. II.3):

$$\tilde{E}(\omega) = \mathcal{F}\left(\tilde{E}(t)\right) = \frac{1}{\sqrt{2\pi}} \int \mathrm{d}t\, \tilde{E}(t)\, e^{-i\omega t}, \qquad \text{II.2}$$

$$\tilde{E}(\mathrm{t}) = \mathcal{F}^{-1}\left(\tilde{E}(\omega)\right) = \frac{1}{\sqrt{2\pi}} \int \mathrm{d}\omega\, \tilde{E}(\omega)\, e^{i\omega t}. \qquad \text{II.3}$$

An important quantity to characterize a laser pulse is the product of the temporal and spectral width, which is called time-bandwidth product. It is often described by the full-width-half-maximum of the intensity (FWHM: Δ_t: time and Δ_ω frequency) and is limited downwards by the threshold $2\pi \cdot c_B$ due to the uncertainty limit. This threshold depends with the parameter c_B on the shape of the intensity distribution and reaches its minimum for a sech-shaped pulse ($c_B \approx 0{,}315$). In order to achieve short laser pulses, the spectral width must be large. Therefore, a laser pulse in the sub 10 fs regime can only be provided by a spectrum with a width $\Delta_\omega \geq 0{,}2\,\frac{1}{\mathrm{fs}} = 2\pi \cdot 31{,}5$ THz. This corresponds to a FWHM above 70 nm for a spectrum centred at 800 nm [53].

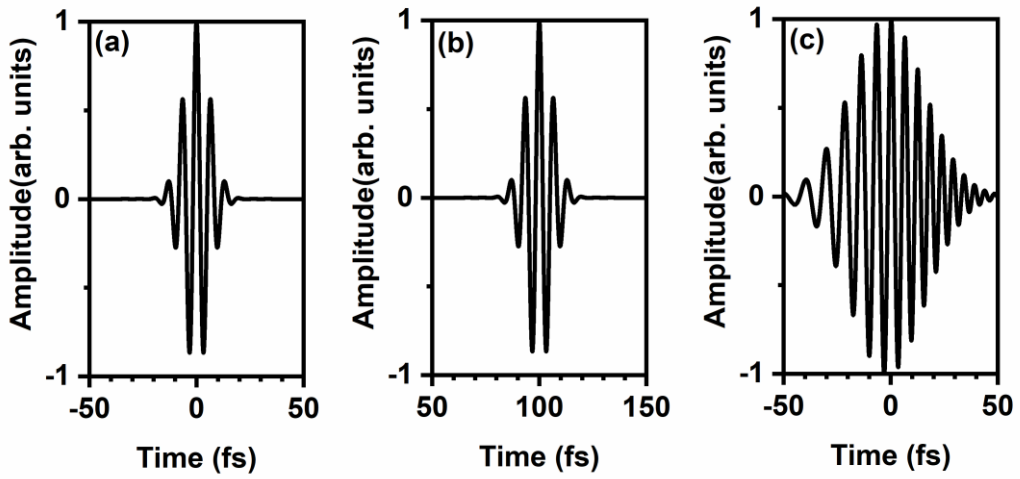

Figure II.1 Impact of the phase on the temporal shape of laser pulses: (a) The Gaussian shaped transform-limited 10 fs laser pulse with a carrier wavelength at 2 µm is as short as possible with respect to the time-bandwidth product. (b) A linear phase with the slope τ_{group} = 100 fs shifts the laser pulse linearly in time without changing its temporal envelope. (c) By imprinting a chirp of GDD = 100 fs^2, frequencies are ordered linearly in time and the pulse is temporally stretched.

However, a broad spectrum does not lead inevitably to a short laser pulse. The time-bandwidth product reaches the threshold only for so called transform-limited pulses, whose phase derivative $\frac{\partial\phi(t)}{\partial t}$ is constant (see eq. II.9). For a finite $\frac{\partial\phi(t)}{\partial t}$, the pulse is stretched in time and the time-bandwidth product increases $\Delta_t\Delta_\omega > 2\pi c_B$.

The impact of the phase can be analysed in frequency domain by the complex electric field $\tilde{E}(\omega)$ with its amplitude $E_0(\omega)$ and phase $\varphi(\omega)$ (eq. II.4). The spectral phase $\varphi(\omega)$ is described by a Taylor series and has three main factors (eq. II.5): the carrier envelope phase $CEP = \varphi(\omega_0)$, the group delay $\tau_{group} = \frac{\partial\varphi}{\partial\omega}\Big|_{\omega_0}$ and the group-delay-dispersion $GDD = \frac{\partial^2\varphi}{\partial^2\omega}\Big|_{\omega_0}$:

$$\tilde{E}(\omega) = E_0(\omega)e^{i\varphi(\omega)}, \qquad \text{II.4}$$

$$\varphi(\omega) = \sum_{i=0}^{\infty} \frac{1}{n!}\frac{\partial^n\varphi}{\partial\omega^n}\Big|_{\omega_0}(\omega-\omega_0)^n \approx CEP + \tau_{group}(\omega-\omega_0) + \frac{1}{2}GDD(\omega-\omega_0)^2. \qquad \text{II.5}$$

The *CEP* shifts only the oscillating electric field within its unchanged envelope. In contrast, the linear phase term $\frac{\partial\varphi}{\partial\omega}\Big|_{\omega_0}\cdot(\omega-\omega_0)$ shifts the envelope of the laser pulse in time with the group delay τ_{group} (Figure II.1a&b). The quadratic term GDD orders the frequencies linearly in time ($\omega(t) \propto t$) and stretches the laser pulse temporally. This is illustrated in Figure II.1c by a laser pulse, whose temporal width is stretched from 10 fs to roughly 60 fs and the frequency at negative times are smaller than at positive ones. In accordance with the analogy between this frequency dependence and a birdsong, the quadratic phase is called up and down chirp for a positive and negative GDD, respectively.

A GDD is usually imprinted on laser pulses by inserting a glass substrate with the thickness *L* into the beam path. The glass substrate has a refractive index $n(k)$ and modifies the dispersion relation between frequency and wave vector k (eq. II.6). This results in a material specific phase velocity $c_M(k)$, which is smaller than the light velocity in vacuum c and imprints the phase $\Delta\varphi$ on the laser pulse (eq. II.7):

$$\omega(k) = c_M(k)\cdot k = \frac{c}{n(k)}k, \qquad \text{II.6}$$

$$\Delta\varphi(\omega) = (n(\omega)-1)\frac{\omega}{c}L. \qquad \text{II.7}$$

In order to observe the quadratic dependence in eq. II.7, the spectral shape of the refractive index must be taken into account. This is provided by the empirical derived Snellmeier equation and shows for many materials a strong quadratic dependence [54]:

$$n^2(\lambda) = 1 + \sum_{i=1}^{3} \frac{B_i \lambda^2}{\lambda^2 - C_i}. \qquad \text{II.8}$$

The parameters of this equation (B_i, C_i) yield a positive chirp for all materials in the visible and NIR region. In contrast, materials with positive (e.g. germanium) as well as negative (e.g. fluorides) amounts of chirp are available in the MIR region. The dispersion of a specific material is usually expressed in literature by the group-velocity-dispersion (GVD), which is the GDD per unit length.

While in many applications the imprinted phases should be as small as possible, the phase is modified actively for many applications. Several phase shaping concepts are introduced in the following section.

1 ii. Pulse shaping

Pulse shaping is the manipulation of a laser pulse via its amplitude and phase. In general, every optical element can be interpreted as a pulse shaper by multiplying a transfer function

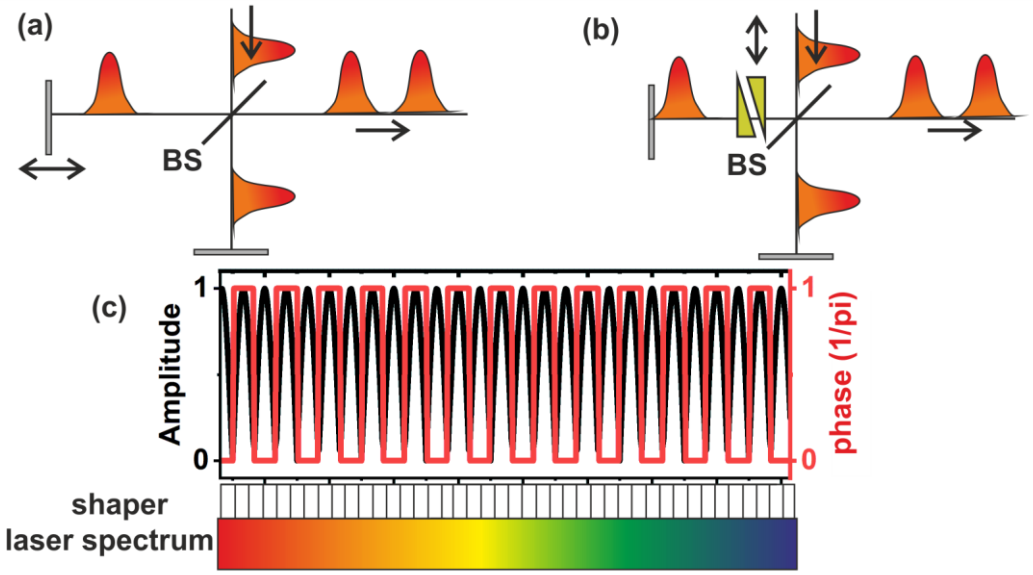

Figure II.2 (a&b) Two identical laser pulses can be obtained by a Michelson interferometer. A single laser pulse is split into two pulses by a beam splitter (BS) and the time delay of these pulses is adjusted by using a movable mirror (a) or a pair of glass wedges (b). (c) Flexible pulse shaping can also generate the double pulses by imprinting the specific transfer function via the pulse shaper on the laser spectrum. The transfer function consists of a spectral phase and amplitude.

$M(\omega)$ on the incoming electric field E_{in} of the laser pulse (eq. II.9). A coloured glass or a filter, for example, are simple elements for amplitude shaping by their potential to cut the spectrum or to reduce the intensity. Phase shaping is also accomplished by every inserted substrate in the beam path since it disperses the laser pulses [55]:

$$E_{out}(\omega) = M(\omega) \cdot E_{in}(\omega). \qquad \text{II.9}$$

The different types of pulse shaping are exemplarily shown on the generation of two laser pulses with an arbitrary time delay τ. This is usually accomplished by a Michelson interferometer, which splits the laser pulse on a substrate in two replicas (Figure II.2a). Whereas one of the laser pulses passes a static beam path, the path length of the other one is varied by a moveable mirror. In order to analyse the Michelson interferometer in accordance with pulse shaping, it is separated in an amplitude shaping provided by the beam splitter and an phase shaping, which is described by a linear phase affecting the time delay (see eq. II.10 and Figure II.1b):

$$M(\omega) = \left(1 + \mathrm{e}^{i\omega\tau}\right). \qquad \text{II.10}$$

This Michelson interferometer can be modified by inserting a pair of glass wedges in one of the beam paths (Figure II.2b). The glass wedges imprint an additional phase on the laser pulse, which disperses and delays the laser pulse. A time delay of 1 ps can be obtained, for example, by changing the thickness of a BK7 glass ($n_g \approx 1{,}52$) around 500µm [1]. The dispersion of such a small variation is negligible ($GDD \approx 20$ fs^2). Therefore, the glass wedges are another method to accomplish the time scan, as usually exploited in multi-dimensional time-resolved spectroscopy [56].

On their downsides, Michelson interferometers are static and restricted to one specific task. Extensions or modifications of the setup are only possible by rebuilding the setup mechanically. The solution is a programmable pulse shaper, which can address each problem by tailoring the laser pulses arbitrary. Flexible pulse shaping is provided by imprinting a spectral phase $\varphi(\omega)$ and amplitude $A(\omega)$ function on the laser pulse via the transfer function $M(\omega)$ (eq. II.11):

$$M(\omega) = A(\omega)e^{i\varphi(\omega)}. \qquad \text{II.11}$$

The two pulses with a variable time delay τ are simply accomplished by splitting eq. II.10 in the phase and amplitude contributions as shown on eq. II.12 and Figure II.2c. The successful implementation of double pulses via a shaper has even shown a temporal resolution of zeptoseconds (10^{-21}s) for interferometry [57]:

[1] $L = \frac{\tau \cdot c}{n(\omega)-1}$ [L substrate thickness; τ: time delay]

$$M(\omega) = A(\omega)e^{i\varphi(\omega)} = \left|\cos(\omega\frac{\tau}{2})\right| e^{ia(\omega)} \qquad \text{II.12}$$

$$\text{with } a(\omega) = \begin{cases} 0 & \text{if } \cos\left(\omega\frac{\tau}{2}\right) \geq 0 \\ \pi & \text{if } \cos\left(\omega\frac{\tau}{2}\right) < 0 \end{cases}.$$

There are a lot of different experimental realisations of flexible pulse shaping. Most of them use spatial masks, which vary the optical thickness spatially on a broad window. In order to imprint a spectral phase on the laser pulse, the spectrum of the laser pulse is spatially dispersed on this window by a 4 f setup. This is discussed in detail for the used liquid crystal pulse shaper in section III.2

2. Nonlinear spectroscopy

2 i. Nonlinear optics

Dispersion and absorption can be described by the Lorentz oscillator model in linear optics. It assumes a bound electron with the charge $-e$ and the mass m in the interaction with light. The electric field $\tilde{\boldsymbol{E}}(t)$ of the light deflects the electron out of the equilibrium and the restoring force $\boldsymbol{F_R}$ moves it back. While the electric field $\tilde{\boldsymbol{E}}(t)$ is well below the intramolecular bounding forces $\boldsymbol{E_{atom}}$, the restoring force ($\boldsymbol{F_R} = m{\omega_0}^2\boldsymbol{x}$; $F_{NL} = 0$) has only a linear dependence on the displacement $\boldsymbol{x}$ and the electron acts as a harmonic oscillator, which is damped by $-2\gamma\dot{\boldsymbol{x}}$ (in eq. II.13 & II.14)[54].

However, this model does not work for intense light. If light induces forces in the order of the intra-atomic forces, the electron movement is perturbed by non-linear force $\boldsymbol{F_{NL}}$ (eq. II.14) and additional electric fields are emitted. For a non-linear potential up to the second order (eq. II.15; $\boldsymbol{e}_x$ unit vector in direction of $\boldsymbol{x}$), for example, the electron motion drives the emission of a DC and a frequency doubled electric field (Figure II.3):

$$m\,\ddot{\boldsymbol{x}} = \boldsymbol{F_R} - 2\gamma\dot{\boldsymbol{x}} - e\tilde{\boldsymbol{E}}(t), \qquad \text{II.13}$$

$$\boldsymbol{F_R}(\mathbf{x}) = -\mathrm{m}\omega_0^2\boldsymbol{x} + \boldsymbol{F_{NL}}(\boldsymbol{x}), \qquad \text{II.14}$$

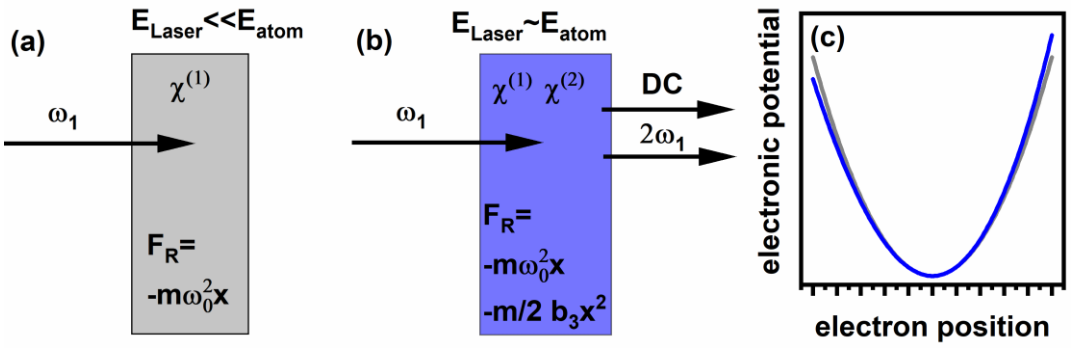

Figure II.3 Demonstration of the linear (a) and non-linear (b) light-matter. (a) If light with a small electric field and the frequency ω_1 incidents a material, the light is dispersed and absorbed. (b) If the electric field of the incoming light is in the order of the interatomic electric field, a DC field and light with the doubled frequency (2 ω_1) is generated. (c) The dispersion and absorption can be descripted microscopically by an electron movement in a harmonic potential. This symmetric potential is disturbed by higher order terms.

$$\boldsymbol{F_{NL}} = -\frac{m\, b_3}{2}|\boldsymbol{x}|^2 \boldsymbol{e_x}. \qquad \text{II.15}$$

In order to describe the nonlinear interaction, the microscopic movements of the electrons can be summed up over all electrons (number N) to the polarization $\boldsymbol{P_{tot}} = -N\mathrm{e}\sum_n \boldsymbol{x}^{(n)}$, which is divided into a linear and non-linear part:

$$\boldsymbol{P_{tot}} = \boldsymbol{P_{linear}} + \boldsymbol{P_{non-linear}}. \qquad \text{II.16}$$

The strength of the polarization is described by the susceptibility of the specific order n $\chi^{(n)}$ and the electric field E:

$$\boldsymbol{P_{tot}} = \epsilon_0 \left(\boldsymbol{\chi^{(1)}E} + \boldsymbol{\chi^{(2)}E^2} + \boldsymbol{\chi^{(3)}E^3}\right) + \mathcal{O}(\boldsymbol{E}^4). \qquad \text{II.17}$$

The susceptibility $\boldsymbol{\chi^{(n)}}$ decreases rapidly with increasing order *n*. Thus, only the polarization and susceptibility 2nd order ($\left|\boldsymbol{\chi}^{(2)}\right| \sim 10\,\frac{\mathrm{pm}}{\mathrm{V}}$) and 3rd order ($\left|\boldsymbol{\chi}^{(3)}\right| \sim 100\,\frac{\mathrm{pm}^2}{\mathrm{V}^2}$) are usually taken into account.

It is important to note that the susceptibility is a tensor. The susceptibility 2nd order, for example, is the sum of 12 individual tensors, whereas each one consists of 27 individual components by the 3 different spatial polarizations and 3 interacting electric fields. Fortunately, the number of independent tensors entries can be reduced up to 18 by taking the symmetry and properties of electro-magnetic waves into account [58].

In the following section, the susceptibility 2nd order for second-harmonic generation and difference-frequency (DF) generation is explained in consideration of the phase matching and the conversion efficiency. Furthermore, MIR generation and SF spectroscopy are introduced as two applications of the 2nd order nonlinear process. Finally, the susceptibility 3rd order is considered by CARS spectroscopy (section 2 iii).

2 ii. 2nd order nonlinear susceptibility: principle of MIR generation and sum-frequency spectroscopy

In order to describe the impact of the first term of the nonlinear polarization ($\propto \boldsymbol{\chi^{(2)}}\,\boldsymbol{E^2}$), monochromatic light with the electric fields $\boldsymbol{E_1}(t)$ and $\boldsymbol{E_2}(t)$ and the corresponding frequencies ω_1 and ω_2 are considered (eq. II.18). The generated polarization $\boldsymbol{P_3}$ has five different contributions: a DC field, two contributions with a doubled frequency $2\omega_1$ and $2\omega_2$ and two additional contributions with the sum and difference frequency $\omega_1 \pm \omega_2$ (eq. II.19). The polarization drives the light emission at these frequencies due to the energy conservation:

$$\boldsymbol{E}(t) = \boldsymbol{E_1}(t) + \boldsymbol{E_2}(t) = \mathrm{Re}\left(\boldsymbol{E_{1,0}} e^{\mathrm{i}\omega_1 t} + \boldsymbol{E_{2,0}} e^{\mathrm{i}\omega_2 t}\right), \tag{II.18}$$

$$\begin{aligned} \boldsymbol{P_3}(t) &\propto \boldsymbol{\chi^{(2)}} \boldsymbol{E}(t)^2 \\ &\propto \boldsymbol{\chi^{(2)}} \cdot \left(\frac{1}{2} \left\{ \boldsymbol{E_{1,0}}^2 e^{\mathrm{i}2\omega_1 t} + \boldsymbol{E_{2,0}}^2 e^{\mathrm{i}2\omega_2 t} \right\} + \left|\boldsymbol{E_{1,0}}\right|^2 + \left|\boldsymbol{E_{2,0}}\right|^2 \right. \\ &\quad + \left(\boldsymbol{E_{1,0}} \quad \boldsymbol{E_{2,0}} \quad e^{\mathrm{i}(\omega_1+\omega_2)t} \right. \\ &\quad \left. \left. + \boldsymbol{E_{1,0}} \quad \boldsymbol{E_{2,0}}^* e^{\mathrm{i}(\omega_1-\omega_2)t} \right) \right). \end{aligned} \tag{II.19}$$

The emitted light with its electric field $\boldsymbol{E_3}(t)$ and frequency ω_3 is derived by inserting $\boldsymbol{P_3}(t)$ into the wave equation and solving it. An analytical solution can only be obtained under special assumptions. By considering the same magnitude of the incoming electric fields and the propagation of all beams collinear in z-direction (reduction to 1D), the intensity ($I_3 \propto |E_3|^2$) of the generated electric field is expressed similar for all contributions of P_3 (eq. II.20). It depends linearly on the incoming intensities $I_1 \propto |E_1|^2$ and $I_2 \propto |E_2|^2$ as well as quadratically on the crystal length L. In addition, it depends on the product of the crystal length and the wave-vector mismatch Δk appearing inside the sinc-function. It should be stressed out at this point, that Δk is scalar here due to the propagation in z-direction of all beams:

$$I_3 \propto I_1 I_2 \mathrm{sinc}^2 \left(\frac{\Delta k \, L}{2} \right) L^2. \tag{II.20}$$

By taking the argument of the sinc-function into account, an efficient non-linear process is only possible for $\Delta k \cdot L \approx 0$. Consequently, the wave-vector mismatch should be as small as possible to promote a high intensity I_3 in non-linear crystals with a large L.

2 ii a. Phase matching

The condition $\Delta k \approx 0$ is called phase matching and can be interpreted as momentum conservation for the SF (eq. II.21) and DF (eq. II.22) process (using the wave vectors k_1, k_2, and k_3):

$$\Delta \mathrm{k} = k_1 + k_2 - k_3 \approx 0, \tag{II.21}$$

$$\Delta \mathrm{k} = k_1 - (k_2 + k_3) \approx 0. \tag{II.22}$$

These conditions are not fulfilled in isotropic media and require birefringent materials, whose refractive index is different in dependence on the axis (eq. II.23). The polarization

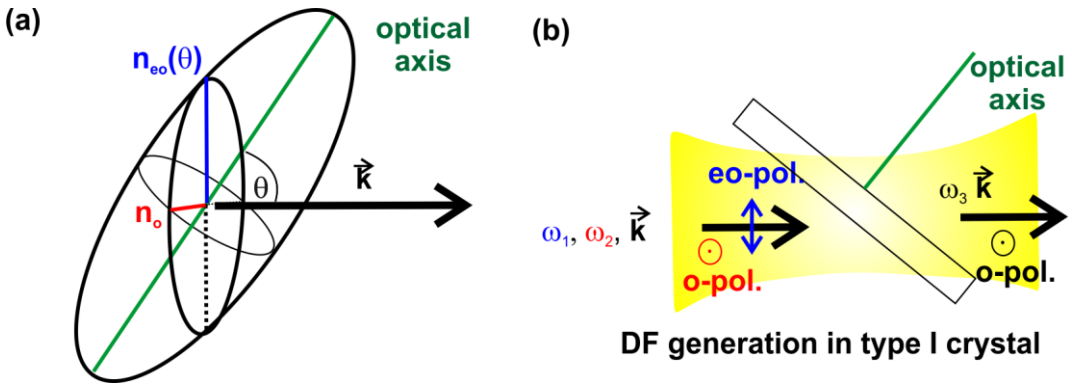

Figure II.4 (a) The refractive indices of birefringent crystals are described by an index ellipsoid consisting of a constant ordinary refractive index n_o and extraordinary refractive index $n_{eo}(\theta)$ which depends on the angle between wave vector k and optical axis. For $\theta = 0$, $n_{eo}(\theta)$ is equal to n_o. By increasing θ, the optical axis is tilted and $n_{eo}(\theta)$ increases. (b) For an efficient (collinear) DF generation in Type I crystals, the blue-detuned $E(\omega_1)$ is polarized in the plane spanned by the optical axis and the direction of the incoming light. The red-detuned electric field $E(\omega_2)$ is orthogonal to this plane. The generated electric field $E(\omega_3)$ has a polarization parallel to $E(\omega_2)$.

of the light is aligned along the axis to adjust the wave vectors by the specific refractive index[1]; Whereas the wave vector of an electric field polarized perpendicular to the optical axis is affected by the ordinary refractive index n_o, the extraordinary refractive index n_{eo} affects the wave vector, whose electric field is polarized in the plane spanned of the wave vector and the optical axis (see Figure II.4a). In addition, this extraordinary refractive index $n_{eo}(\theta)$ depends on the angle θ between the wave vector and the optical axis. It can be tuned from n_o at $\theta = 0$ to n_{eo} at θ = 90° and is adjusted to fulfil the phase matching condition. In accordance, this angle is called phase matching angle. In order to clarify the nomenclature, it should be noted that $n_{eo}(\theta = 90°, \omega) = n_{eo}(\omega)$ in eq. II.23:

$$\frac{1}{n_{eo}{}^2(\omega\ ,\theta)} = \frac{\cos^2(\theta)}{n_0{}^2(\omega\ )} + \frac{\sin^2(\theta)}{n_{eo}{}^2(\omega\ )}. \qquad \text{II.23}$$

There are two different kinds of phase matching conditions in birefringent crystals. In Type I crystals, the electric fields oscillating with smaller frequencies have the same polarization. These are perpendicular to the polarization of the electric field with higher frequency. The energy and momentum conservation in a Type I crystal is shown for the SF process (eq. II.24) and DF process (eq. II.25 and see Figure II.4b). Phase matching in Type II crystals is accomplished by a perpendicular polarization of the two lower energetic electric fields. (Type II phase matching is not considered in this work);

[1] $k = n(\omega)\omega/c$

$$\omega_1 + \omega_2 = \omega_3, \qquad \text{II.24}$$

$$n_o(\omega_1) \cdot \omega_1 + n_o(\omega_2) \cdot \omega_2 = n_{eo}(\omega_3, \theta) \cdot \omega_3, \qquad \text{SF process}$$

$$\omega_1 - \omega_2 = \omega_3, \qquad \text{II.25}$$

$$n_{eo}(\omega_1, \theta) \cdot \omega_1 - n_o(\omega_2) \cdot \omega_2 = n_o(\omega_3) \cdot \omega_3. \qquad \text{DF process}$$

2 ii b. Broadband SF and DF generation

The discussion above about SF and DF generation was fully derived by monochromatic electric fields. However, the polarization $P_3(t)$ is usually generated by laser pulses with a broad spectrum Therefore, a mathematical description in the frequency domain is more convenient. This is presented for the SF process in the following. In order to derive an analytical solution, several assumptions are made. Firstly, a thin crystal with the length L and a constant susceptibility d at a given phase matching angle is assumed ($\chi^{(2)}(\omega', \omega) = \text{const.}$). The second assumption considers strong fundamental electric fields which are not depleted by the electric field of the SF light. Therefore, constant electric fields $E_1(\omega)$ and $E_2(\omega)$ as well as a defined dispersion relation at the entrance of the crystal can be assumed. The generated electric field $E_3(\omega)$ is derived under consideration of the slowly varying amplitude approximation. The generated electric field $E_3(\omega)$ depends on the convolution of the fundamental electric field and a term taking the phase matching into account [58-60]:

$$E_3(\omega, \mathrm{L}) \propto d \cdot \int d\omega' E_1(\omega') E_2(\omega - \omega') \times \int_0^L e^{i\Delta k(\omega', \omega) z} dz. \qquad \text{II.26}$$

In order to provide an intuitive access to these equations, the limit of an infinite thin crystal is assumed (i.e. $\int_0^L e^{i\Delta k(\omega,\Omega)z} dz \approx \cdot 1$). In this case, only the convolution of the spectra must be considered:

$$E_3(\omega) \propto \int d\omega' E_1(\omega') E_2(\omega - \omega'). \qquad \text{II.27}$$

The electric field generated in the DF process can be similarly derived (eq. II.28). The SF as well as the DF generated electric field are illustrated in Figure II.5;

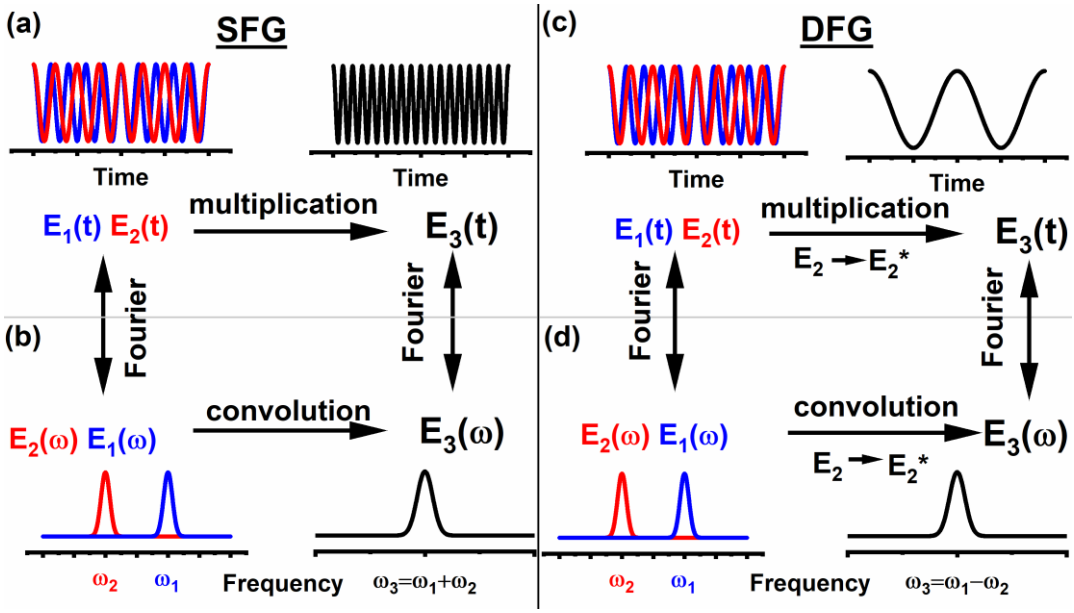

Figure II.5 SF (a&b) and DF generation (c&d) process in time and space. (a) The SF process is described in time by the product of the electric fields E_1 (blue) and (red) with the frequencies ω_1 and ω_2. SF generated light (black) with the electric field E_3 is emitted with an oscillation at the sum of the interacting frequencies $\omega_1 + \omega_2$. (b) This process is depicted in frequency space after a convolution. (c) In the DF process, the interaction of the blue detuned E_1 (blue) and the red-detuned E_2 (red) can also be described by a multiplication when considering the complex conjugation of E_2. (d) The electric field $E_3(\omega)$ (black) is the convolution of the electric fields E_1 (blue) and complex conjugated E_2 (red).

$$E_3(\omega) \propto \int d\omega' E_1(\omega') E_2^*(\omega - \omega') \,. \qquad \text{II.28}$$

It is important to note that the numerical fast Fourier transform is much faster than a direct convolution. This is exploited in all simulations of this work for SF and DF generation by modelling the spectra of the electric fields by a product in time domain via eq. II.29 and eq. II.30, respectively [60]:

$$E_3(\omega) \propto \mathcal{F}\{\mathcal{F}^{-1}(E_1(\omega)) \cdot \mathcal{F}^{-1}(E_2(\omega))\}, \qquad \text{II.29}$$

$$E_3(\omega) \propto \mathcal{F}\{\mathcal{F}^{-1}(E_1(\omega)) \cdot \mathcal{F}^{-1}(E_2{}^*(\omega))\}. \qquad \text{II.30}$$

2 ii c. Applications

In the presented work, two 2nd order nonlinear processes are exploited: the generation of MIR light (i) and SF spectroscopy (ii).

(i) In order to generate MIR light, two electric fields with slightly shifted frequencies are required. The frequencies are usually in the NIR region and their electric fields generate in a DF process MIR light, which is located spectrally at the difference frequency of the incoming NIR frequencies. In accordance with the nomenclature in the CARS process (see later in section 2 iii), the lower-energetic and higher-energetic electric fields are called pump and Stokes, respectively.

The pump and Stokes can be obtained either from one laser pulse having a broad spectrum or from two different laser pulses with narrowband spectra. Their spectral and temporal shapes have a huge impact on the spectrum of the generated MIR pulses as discussed in detail in chapter IV.

(ii) SF spectroscopy is a powerful spectroscopic technique, which gives access to molecular vibrations in non-centrosymmetric systems. This access is provided by direct MIR excitations using a NIR and MIR laser pulse. The MIR pulse directly excites the vibrational modes of a molecule and these modes are non-resonantly probed by the NIR pulse while emitting SF light. The intensity of this SF light I_{SF} is proportional to the absolute square value of the susceptibility 2nd order (eq. II.31) which depicts the vibrational modes with their complex Lorentzian line shapes (Amplitudes B_n, centre frequencies ω_n and decay rates Γ_n). By adjusting the energy of the MIR laser pulse to a vibrational mode, the non-linear process and the generated SF light I_{SF} is enhanced by many orders of magnitude. This gives access to the information of the vibrational modes in the SF spectrum:

$$I_{SF} \propto \left| \chi_{nr} + \sum\nolimits_n \frac{B_n}{(\omega \quad - \omega_n) - \mathrm{i}\Gamma_n} \right|^2 . \qquad \text{II.31}$$

The SF spectrum shows additionally a contribution of a non-resonant background χ_{nr}, which interferes with the resonant contribution. This background appears in almost all non-linear spectroscopy techniques and is discussed in detail in CARS spectroscopy (see. 2 iii).

2 iii. CARS spectroscopy

CARS spectroscopy is another powerful technique to determine molecular vibrations. In contrast to SF, CARS is not restricted to non-centrosymmetric systems, and is also sensitive to isotropic media [36, 61-63]. The CARS process is a four-wave mixing process, which requires the interaction of three different electric fields. Two of them (E_{pump}, E_{Stokes}) have a slightly detuned frequency and are called pump and Stokes (for simplicity both propagate in z-direction). The energetic-lower Stokes and energetic-higher pump generate in a DF process (eq. II.33) a coherence $A(\Omega)$ at the difference frequency Ω of pump and Stokes. This process is described equally to the 2nd order non-linear DF generation (eq. II.28). Instead of emitting MIR light directly, the light with the electric field E_{CARS} is emitted after the interaction with the third electric field E_{probe}, which is called probe (eq. II.32):

$$E_{CARS}(\omega) \propto \int d\Omega\, A(\Omega)\chi^{(3)}(\Omega)E_{probe}(\omega-\Omega), \qquad \text{II.32}$$

$$A(\Omega) = \int d\omega\, E_{pump}(\omega)E^{*}_{Stokes}(\omega-\Omega). \qquad \text{II.33}$$

By tuning the frequency difference Ω between pump and Stokes, the whole CARS spectrum can be acquired. The spectrum shows the vibrational signature of the material by the absolute square of the susceptibility 3rd order $\left|\chi^{(3)}\right|^2$.

This susceptibility has a resonant contribution $\chi^{(3)}_{Res}$ and depicts all Raman active vibrational modes with their Fano line shape in the real part and a Lorentzian line shape in the imaginary part (see eq. II.34 Ω_R, decay rate: Γ_R; Amplitude A_R.). The resonant contribution $\chi^{(3)}_{Res}$ and the corresponding CARS spectrum are illustrated in Figure II.6a&b. The susceptibility 3rdorder $\chi^{(3)}$ consists also of a non-resonant background $\chi^{(3)}_{NR}$, which is generated by an interaction with a different energetic ordering of pump and Stokes (see energy diagram in Figure II.6). This constant and real background interferes with the resonant contribution and distorts the line shapes of the vibrational resonances (Figure II.6c & d):

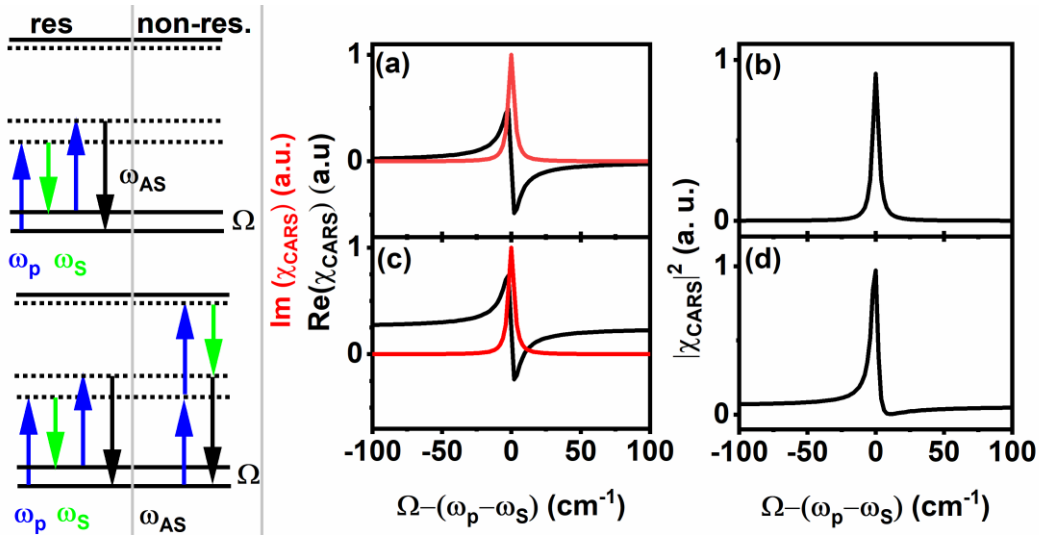

Figure II.6 Comparison of CARS spectra having only a pure resonant contribution (upper row) and a non-resonant contribution in addition (lower row): (a) The complex susceptibility is described by a complex Lorentzian with its dispersion (real part: black) and absorption (imaginary part: red). (b) The detected absolute square of the susceptibility $|\chi_{CARS}|^2$ has the known Lorentzian line shape. (c) The non-resonant background is an offset on the real part. (d) With the interference of the resonant and non-resonant contribution, the line shape of the detected susceptibility $|\chi_{CARS}|^2$ is distorted. On the left side of the image, the energy diagrams of the resonant and non-resonant susceptibility are shown.

$$\chi^{(3)}(\Omega) = \chi_{NR}^{(3)} + \chi_{Res}^{(3)}(\Omega) = \chi_{NR}^{(3)} + \sum_{r} \frac{A_r}{(\Omega - \Omega_r) - i\Gamma_r}. \qquad \text{II.34}$$

It is important to note that the intensity of the non-resonant background scales with the number of additional interactions. This number is large in the interaction of short laser pulses, because many interactions are driven by the temporal overlap of a broad spectrum [64].

In order to extract the information of the vibrational modes, the resonant and non-resonant contributions must be disentangled. This is accomplished either by the time-domain Kramer-Kronig transformation [65] or by the maximum entropy method (MEM) [66]. Latter one decomposes the CARS spectrum into Fourier coefficients and retrieves the amplitude and phase in a fitting procedure. The fitting procedure depicts the constant non-resonant background in a real and constant Fourier coefficient. The time-domain Kramer-Kronig transformation exploits the same fact but in the time domain. It separates a fast decay of the non-resonant background from the slowly decaying vibrational modes.

This non-resonant background can also be experimentally supressed. This is accomplished by using at least two independent laser pulses. The first laser pulse provides pump and Stokes and excites the coherent Raman excitation. The second laser pulse is temporally delayed behind the decay of the non-resonant background. Therefore, this probe pulse generates the CARS signals only in an interaction with the resonant contribution [67, 68].

3. Shaper-based nonlinear spectroscopy

3 i. Towards femtosecond nonlinear spectroscopy

CARS spectroscopy is usually implemented by two NIR laser sources, which provide laser pulses with narrowband spectra (2-10 cm^{-1}) for pump and Stokes. The interaction of pump and Stokes generates a narrowband DF excitation, which can be directly traced back to a specific vibrational mode. The CARS signal is generated by probing this narrowband excitation via an additional interaction with the pump (Figure II.7a & b) [69]. In order to obtain the whole spectrum, the pump spectrum is detuned. In experiments, the temporal and spatial overlap of pump and Stokes must be stable over the whole tuning range. This can be experimentally challenging, especially by a fast wavelength tuning [29].

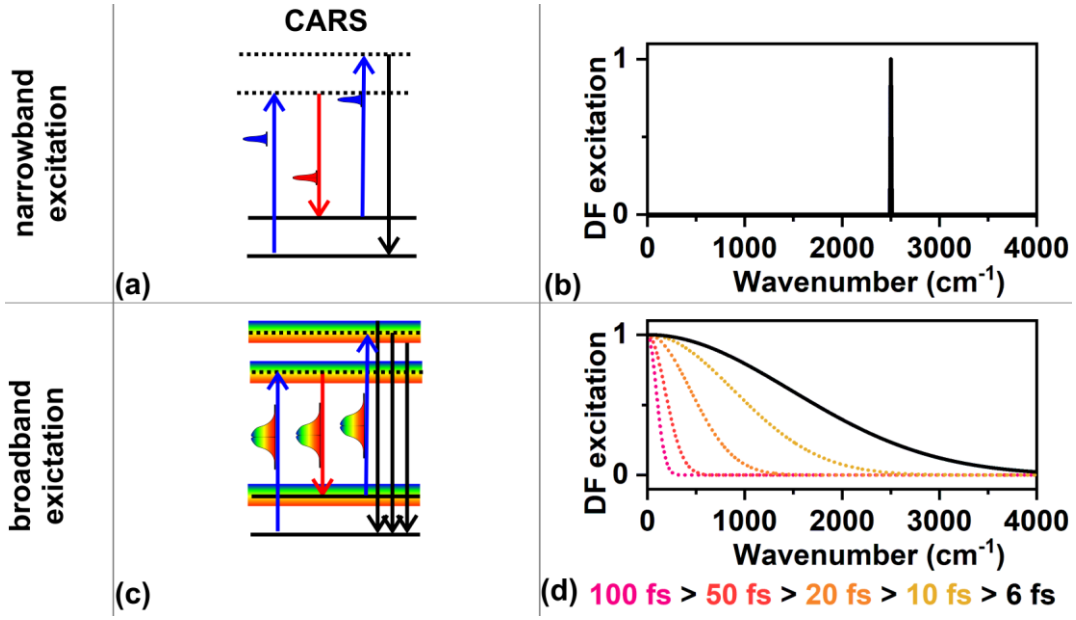

Figure II.7 Comparison of narrowband (1st row) and broadband (2nd row) DF excitations provided by ps and fs pulsed laser sources, respectively: (a) Two laser pulses with narrowband and slightly detuned spectra are used in the CARS process (b) These laser pulses generate a narrowband DF excitation at the frequency difference of the spectra (e.g. at 2500 cm^{-1}). (c) In the use of sub 10 fs laser pulses, the short laser pulses with a broad spectrum are able to generate many DF frequencies simultaneously (rainbow coloured area). (d) Broadband DF excitations with a range up to 3000 cm^{-1} are only possible by sub 10 fs laser pulses (black). 100 fs (purple), 50 fs (red) and 20 fs transform-limited laser pulses (orange) are limited to DF excitations below 250 cm^{-1}, 500 cm^{-1} and 1000 cm^{-1}, respectively. The broadband excitations are simulated by Gaussian shaped laser pulses.

The wavelength tuning can be circumvented by using a broad spectrum, which excites many vibrational modes simultaneously. This can be accomplished by the multiplex and single-beam CARS spectroscopy. In multiplex CARS spectroscopy, a narrowband pump and a broadband Stokes are exploited to excite all vibrational modes. Afterwards, these excitations are probed by the narrowband pump to provide the CARS spectrum with spectral resolution [70, 71]. In contrast, only one laser pulse acting simultaneously as pump, Stokes and probe is required in single-beam CARS spectroscopy (Figure II.7c) [31].

This laser pulse is able to excite all vibrational modes, which have a pair of pump and Stokes within the broad spectrum. In accordance to the profile of the laser spectrum, the DF excitation decreases towards higher frequencies. Therefore, short laser pulses with a broad spectrum are needed to generate a broad DF excitation spectrum. Especially vibrational resonances in the CH stretching region can only be excited, when the pulse length is shorter than 10 fs (see Figure II.7d).

Although this single laser pulse allows for exciting all vibrational modes, the detected CARS signal cannot be linked to a specific vibration and provides up to now no spectral contrast. Pulse shaping is the method of choice to enable spectral resolution using a single ultrabroadband laser pulse. Several shaping concepts have been developed in the last decades to tailor the laser pulse for the purpose of a spectral resolution in CARS [30, 36]. One of the most popular concepts is spectral focusing.

3 ii. Concept of spectral focusing: spectral resolution in difference-frequency processes

Introduced by Veitas *et al* [72], the concept of spectral focusing is a perfect tool to turn a broadband DF excitation into a narrowband and tuneable one [73-75]. In this section, the theory of this concept is summarized (section 3 ii a) [35, 72, 76, 77] and its experimental implementation is discussed (section 3 ii b). Furthermore, the recently discovered extension tailored spectral focusing [35] and its potential for non-resonant background suppression is shown (section 3 ii c).

3 ii a. Concept of spectral focusing

In a single-beam setup, a transform-limited laser pulse excites many frequencies in the DF excitation. Spectral focusing supresses most of these frequencies to generate a narrowband DF excitation $A(\Omega)$ (eq. II.35). This is accomplished by modifying the phase difference $\Delta\varphi$ between pump E_P and Stokes E_S with two parabolic phase functions. These phase functions are defined by the same amount of chirp β and the centre frequencies ω_p and ω_S, respectively (eq. II.36 and Figure II.8a):

$$A(\Omega) \propto \int d\omega \left|E_p(\omega+\Omega)\right| |E_S^*(\omega)| e^{i\Delta\varphi(\omega)}, \qquad \text{II.35}$$

$$\Delta\varphi(\omega) = \frac{\beta}{2}\left(\omega + \Omega - \omega_p\right)^2 - \frac{\beta}{2}(\omega - \omega_S)^2. \qquad \text{II.36}$$

This phase difference $\Delta\varphi$ is reordered mathematically to demonstrate its impact on the DF excitation $A(\Omega)$ (eq. II.37): Whereas for $\Omega \neq \omega_p - \omega_S$ the complex product of pump and Stokes $\tilde{E}_p(\omega + \Omega) \cdot \tilde{\mathrm{E}}_\mathrm{S}^*(\omega)$ interferes destructively over the integral (eq. II.35), the DF excitation $A\left(\Omega \approx \omega_p - \omega_S\right)$ is emphasized by constructive interference. Therefore, the frequency Ω of the narrowband excitation $A(\Omega)$ in eq. II.35 is equally to the difference of the centre frequencies of ω_p and ω_S (see Figure II.8c):

$$\Delta\varphi(\omega) = \beta\left[\Omega - \left(\omega_p - \omega_S\right)\right] \cdot \omega + \mathcal{O}(\omega^0). \qquad \text{II.37}$$

A deeper understanding of the spectral focusing concept is provided in the frequency-time picture by considering the time dependent angular frequency $\omega\ (t) \approx \omega_i + \frac{1}{\beta}t$ for the pump ($\omega_i = \omega_p$) and Stokes ($\omega_i = \omega_S$), respectively. As shown in Figure II.8b, a high amount of chirp stretches the laser pulses up to several picoseconds and reduces the temporal overlap to frequencies with a constant instantaneous frequency difference IFD (eq. II.38 and Figure II.8b). A simple interpretation is depicted in Figure II.8d by the simultaneous increase of the pump and Stokes energy in time, which supresses all other pathways;

$$IFD\ (t) = \omega_p + \frac{1}{\beta}t - (\omega_S + \frac{1}{\beta}t) = \omega_p - \omega_S. \qquad \text{II.38}$$

For pump and Stokes, the centre of the parabolic phase function can be moved around $\frac{\tau}{\beta}$ (eq. II.39). This can be expressed as a linear phase with the slope τ and shows the additional time delay between pump and Stokes. In accordance with eq. II.38, this time delay tunes the IFD to $\omega_p - \omega_S + \frac{\tau}{\beta}$ and accomplishes the tuning of the narrowband DF excitation as depicted in the 2nd column in Figure II.8:

$$\frac{\beta}{2}\left[\omega - \left(\omega_i - \frac{\tau}{\beta}\right)\right]^2 = \frac{\beta}{2}[\omega - \omega_i]^2 + \tau\omega + \mathcal{O}(\omega^0) \qquad \text{II.39}$$

$$\text{with } i \in \{p, S\}.$$

Besides, the spectral width of the DF excitation can be varied by changing the imprinted amount of chirp (Figure II.8 3rd column). In order to understand it, the pulse length $T \approx \beta \cdot \Delta_\omega$ is depicted as the product of the imprinted chirp and the bandwidth of laser spectrum Δ_ω. This relation demonstrates a stretch of the laser pulses by increasing the imprinted

amount of chirp β. The spectral width $\delta\omega = \frac{\pi}{\Delta_\omega \beta}$ of the frequency-time ellipse decreases simultaneously as shown in the 3rd column in Figure II.8.

The spectral focusing concept can also be fully derived in the time domain. This temporal description highlights other aspects of this concept as shown in the appendix (section IX.2).

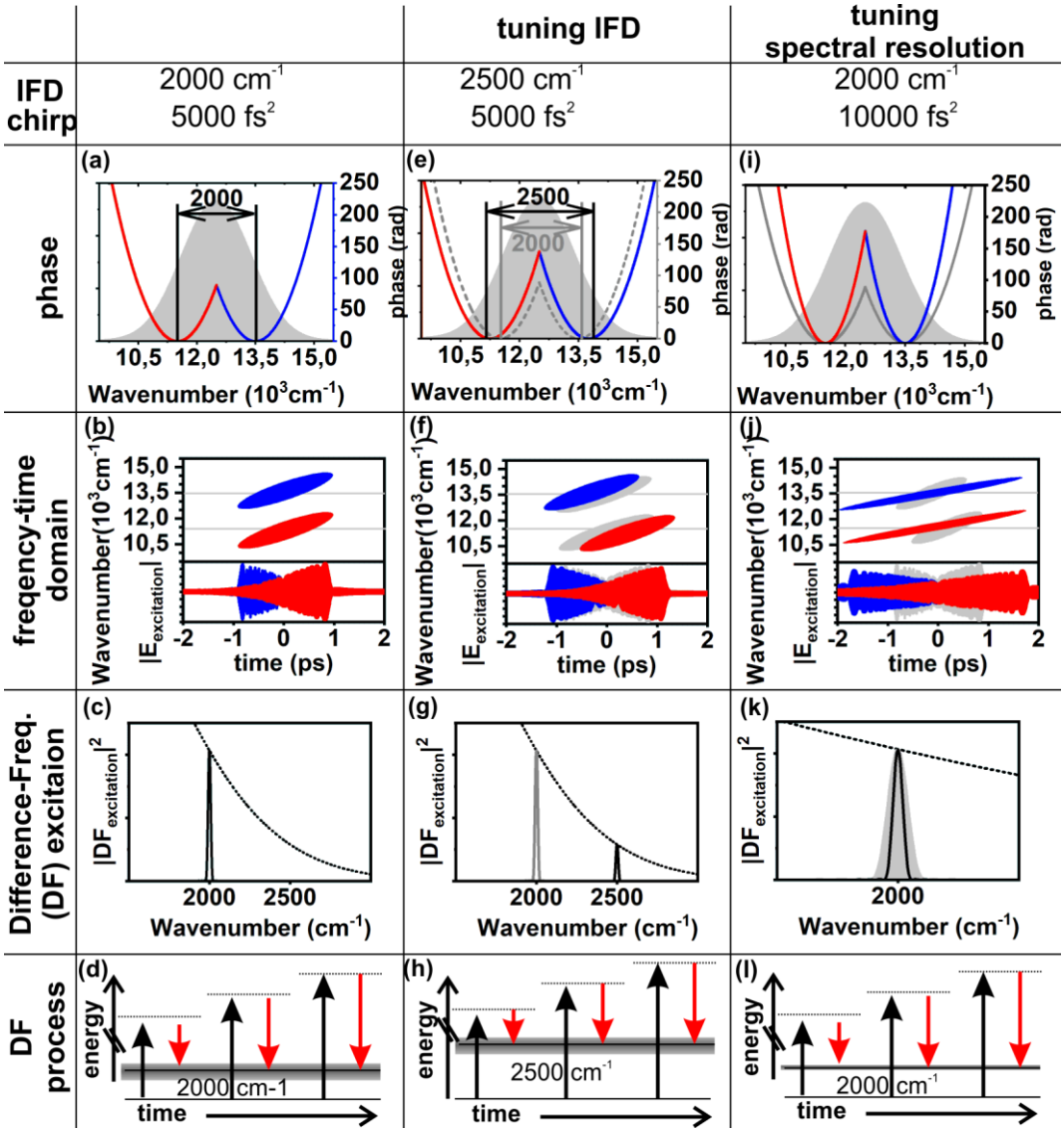

Figure II.8 Concept of spectral focusing: This concept provides in DF processes narrowband excitations (see 1st column), which are tuneable in frequency (2nd column) and spectral width (3rd column). 1st column: (a) In spectral focusing, two parabolic phase functions with the same amount of chirp – e.g. 5000 fs^2- are imprinted. (b) The chirped laser pulses are linearly stretched in time (main panel) and yield a beating in time (lower panel) with a constant frequency at the instantaneous frequency difference (*IFD*), which is defined by the distance of the parabola. (c) In DF generation processes, all off-resonant frequencies are supressed and a narrowband DF excitation at the *IFD*- e.g. 2000 cm^{-1}- is promoted. 2nd column (e&f): The shift of the *IFD*- e.g. from 2000 cm^{-1} (grey) to 2500 cm^{-1} (solid line)- moves the frequency time ellipses in time. (g) In accordance, the narrowband excitation is shifted from 2000 cm^{-1} (grey) to 2500 cm^{-1} (black). 3rd column: (i) The spectral resolution can be tuned by varying the amount of chirp. Increasing the amount of chirp to 10000 fs^2 (red and blue phase) stretches the laser pulses more in time (j main panel). (k) This reduces the bandwidth of the narrowband excitation (solid line). (d&h&l) Spectral focusing concept is illustrated in a time dependent energy diagram.

3 ii b. Experimental implementation of spectral focusing

The spectral focusing concept is usually applied on the individual laser beams of pump and Stokes pulses (Figure II.9a). In these setups, a single laser pulse is split in the pump and Stokes by a dichroic mirror and the chirped phases are imprinted on them either by thick glass rods [78] or grating compressors [73, 79]. Afterwards, pump and Stokes are recombined by a second dichroic mirror and guided to the sample for CARS spectroscopy. In order to acquire the whole spectrum either the pump or Stokes pulse is temporally delayed by a translation stage.

However, both kinds of setups are static: The glass rods are designed for a specific amount of chirp at a given wavelength and must be replaced to change the imprinted amount of chirp. Although the grating compressors are more flexible, the change of the imprinted amount of chirp is quite complex by adjusting the distance of the two gratings inside the compressor. This requires a new alignment of the whole setup and cannot be done in a daily basis.

The use of flexible pulse shaping can overcome these issues by replacing the static optics with a programmable pulse shaper. In spectral focusing, the two parabolic phase function are imprinted on the pulse shaper in a 4f setup. The frequency as well as the spectral width of the narrowband excitation can be simply adjusted by a change of the phase function. Especially, direct control of the spectral resolution via the spectral width is a great advantage of a programmable pulse shaper.

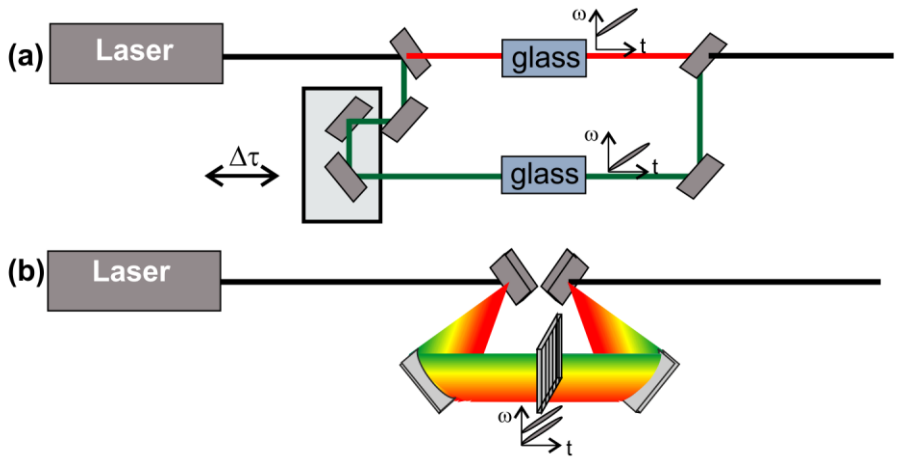

Figure II.9 Experimental implementation of the spectral focusing concept. (a) In many setups, the single laser pulse is split by a dichroic beam splitter. The pump and Stokes pulses are highly chirped by traversing thick glass substrates or a grating compressor. The acquired narrowband excitation can be tuned by a temporal delay of one laser pulse via a translation stage. (b) The concept of spectral focusing can also be realized using a programmable pulse shaper. This is accomplished by passing the laser pulses through the pulse shaper inside a 4f setup. In order tune the DF excitation, the imprinted phases are changed.

3 ii c. Concept of tailored spectral focusing for CARS spectroscopy

Recently, the spectral focusing concept was extended to enable in shaper-based setups a suppression of the non-resonant background observed in CARS spectroscopy. The so-called tailored spectral focusing [35] concept shapes a single laser pulse in order to delay the probe process after the fast decay of the non-resonant background (see section 2 iii). This is accomplished by simply imprinting a new phase function (Figure II.10a). Beside the two parabolic phase functions of pump and Stokes, this phase is linear in independent spectral part. Whereas the parabolic phase functions stretch the pump and Stokes pulses in time to generate the narrowband coherence, the linear phase shifts the probe behind the excitation (Figure II.10b). This delayed probe pulse is able to unveil the undistorted line shape of the vibrational mode as shown in simulations (Figure II.10c). In contrast to the CARS spectrum detected without an independent probe pulse, the spectrum obtained by the delayed probe shows the known Lorentzian line shape.

Furthermore, non-resonant interactions like second-harmonic generation benefits also from this independent probe pulse. In order to understand this, it is important to note that this probe pulse is transform-limited and has usually a temporal width τ below 100 fs [1]. Therefore, generated signals are higher since the generation depends reciprocal on the temporal width τ^{n-1} for the n-th order interaction [80].

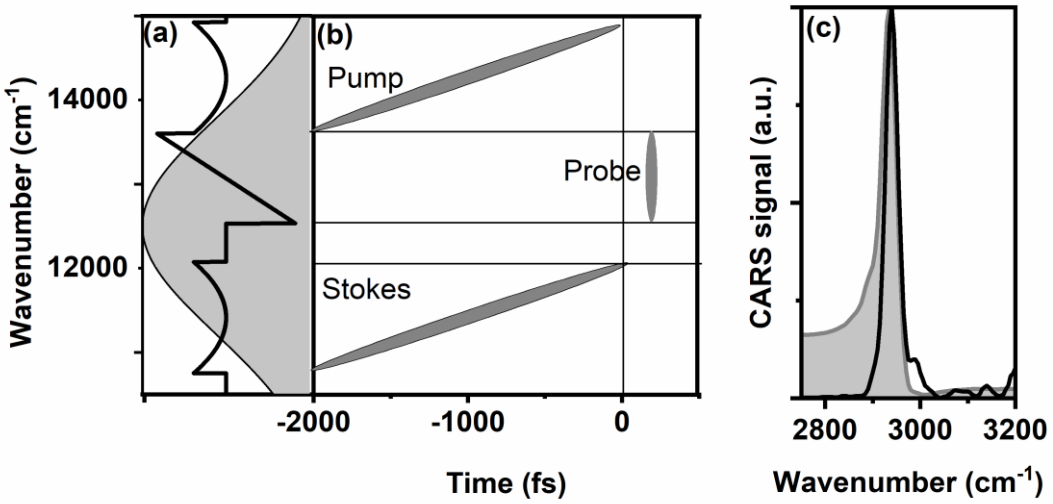

Figure II.10 Demonstration of tailored spectral focusing in a single-beam setup. (a) Beside imprinting two parabolic phase functions on the broad Gaussian shaped laser spectrum (grey background), an additional linear phase is imprinted. (b) In the frequency-time space the probe pulse appears after the pump and Stokes at later time. (c) In CARS spectroscopy, the vibrational resonance is probed by the additional probe laser pulse. Whereas the CARS spectrum probed by the pump is affected by the non-resonant background (grey background), an independent and delayed probe pulse interacts with the resonant contribution after the fast decay of the non-resonant background. The detected vibrational mode shows no distortion.

[1] In assumption of a spectral width above 150 cm^{-1} (assuming a Gaussian shaped pulse)

Moreover, the arbitrary time delay of the probe pulse can be further exploited in time-resolved CARS spectroscopy. By tuning the slope of the linear phase, the time delay of the probe pulse is scanned, and the free induction decay of the vibrational modes is determined.

III. Experimental setup for shaper-based nonlinear microspectroscopy

The potential of multimodal microscopy in a single-beam setup is provided by shaping ultrabroadband laser pulses, whose experimental realization is discussed in this chapter. Initially, the working principle (section 1 i) and the properties (section 1 ii) of the used laser system are described. Afterwards, the experimental implementation of pulse shaping is explained (section 2).

1. Laser system

1 i. Working principle of a Ti:Sa oscillator

Sub 10 fs laser pulses are usually generated in a Ti:Sa oscillator by inserting a Ti^{3+} doped sapphire (Ti:Sa) crystal inside a resonator and by pumping this crystal with a 532 nm centred pump laser. Beside the broad gain bandwidth of the Ti:Sa crystal, its strong susceptibility 3rd order is important for the generation of short laser pulses. Because of this susceptibility, the refractive index of the crystal is varied in dependence on the electric field strength of the laser pulse. Since the spatial intensity profile of the laser pulse yield a higher refractive index inside the crystal than outside, this crystal can be considered as a lens by the so-called Kerr lens effect. Furthermore, the focal length of the crystal is shorter for the transmission of more intense laser pulses. Therefore, only intense laser pulses are focused through a small pinhole, which is present in the resonator. By having the highest electric field strengths, short laser pulses are solely amplified in the so-called mode-locking process due to this pinhole. Nowadays, this pinhole is not needed anymore since the spatial overlap of the laser pulses with the focused pump is used in the mode-locking process [81].

Furthermore, sub 10 fs laser pulses are only generated by implementing chirped mirrors inside the resonator. These mirrors compensate in each round trip the chirp imprinted by the Ti:Sa crystal on the laser pulses. Using additionally chirped mirrors outside the cavity, the generated laser pulses have a temporal width below 10 fs [82].

1 ii. Properties of the used Ti:Sa oscillator

In the following, the main properties of the Ti:Sa oscillator (Femtolasers Fusion Pro 800) used in this work are summarized [82, 83]. This laser source provides laser pulses with an

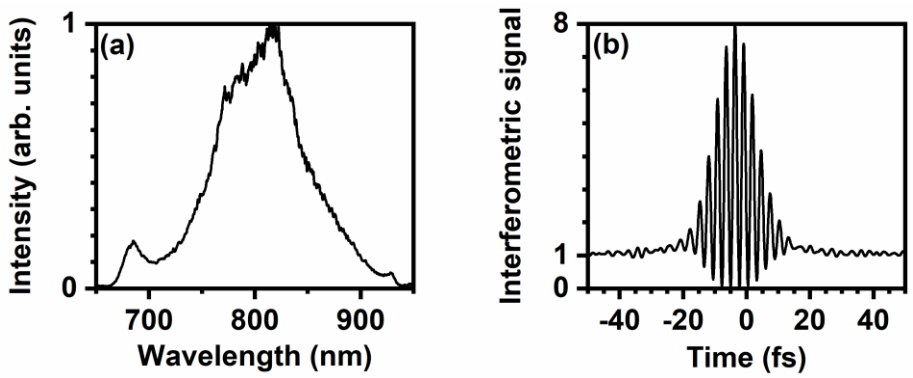

Figure III.1 Spectrum (a) and interferometric autocorrelation (b) of the laser pulses provided by the used Ti:Sa oscillator. (a) The spectrum has a bandwidth, which ranges from 670 nm up to 930 nm. (b) The autocorrelation determines a pulse length with a FWHM of 9 fs.

800 nm centred NIR spectrum, which ranges from 670 nm up to 930 nm (Figure III.1a). Furthermore, the laser pulses have a temporal width between 8,5 fs and 9,3 fs (Figure III.1b), which depends on the alignment of the two-folded resonator. The laser pulses are emitted with a repetition rate of 75 MHz and a pulse energy of 10 nJ, yielding an average output power of 800 mW.

2. Pulse shaping

The temporal and spectral shape of ultrashort laser pulses is adjusted by shaping their phase and polarization. In the presented work, the pulse shaping is accomplished by a spatial light modulator, which imprints the phase functions on a spatially distributed spectrum. Such a spectrum is provided by a 4f setup as shown in section 2 i. Afterwards, the working principle and the properties of the pulse shaper are explained (section 2 ii).

2 i. 4f setup

A 4f setup can be understood as an experimental implementation of two Fourier transforms. The first part of the setup disperses the laser pulse into its spatial distributed spectrum and the second part withdraws the first transformation. Both experimental parts are similar and each of them consists in the simplest application of a grating and a lens (focal length f), separated by f (Figure III.2a). This distance provides the name 4f setup.

In order to understand the 4f setup, only the lenses are considered in a first step (without the gratings). These lenses are aligned with a distance of $2f$ and build a simple imaging system. This system magnifies the spatial distribution of the laser pulses by the first lens in a distance of $1f$ and reduces it back on its original distribution by the second one. In the second step, the gratings are inserted in the setup to image the spectrum. In accordance with

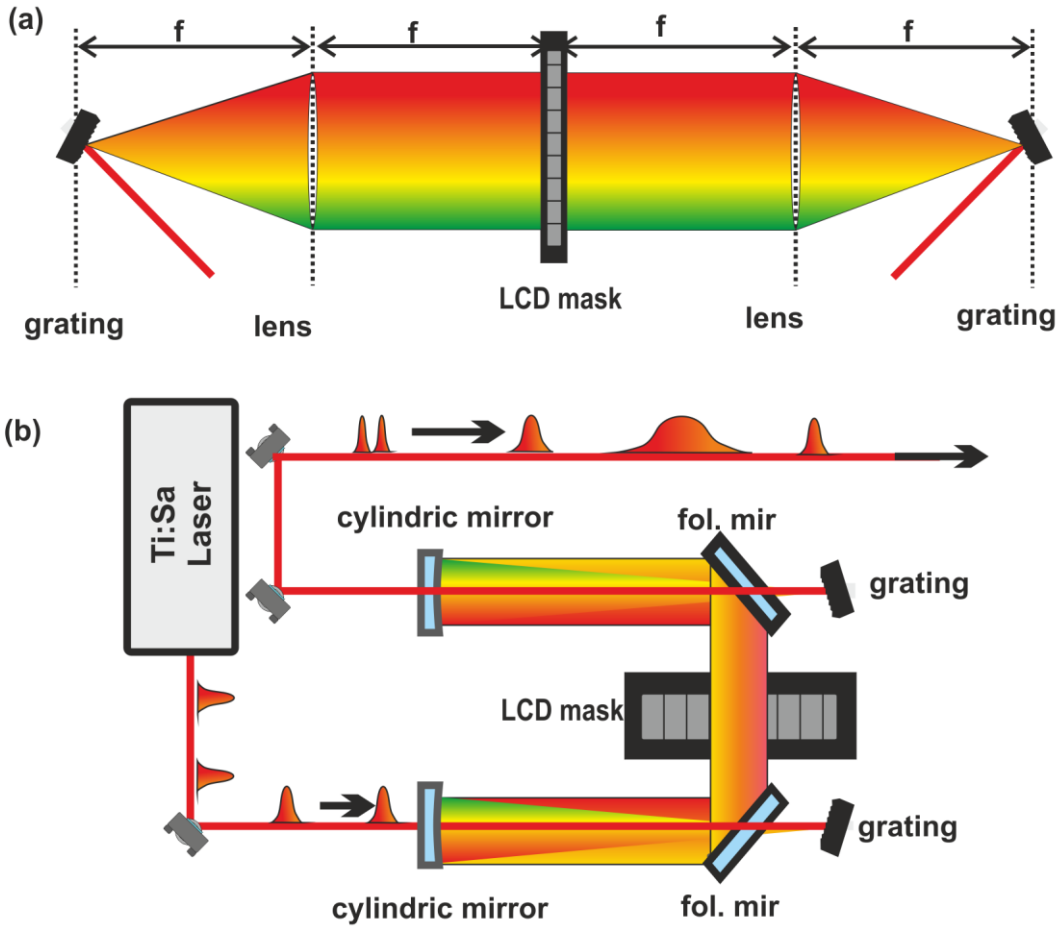

Figure III.2 Principle (a) and experimental implementation (b) of the 4f setup. (a) The 4f setup disperses a laser pulse into its spectrum by a grating and a lens, which are separated by the focal length of the lens. The spectrum is spatially distributed in the Fourier plane having the spatial light modulator (LCD mask) inside. The spectrum is recollimated by an experimental part, which consists of the same lens and grating. All optical elements are separated in one focal length f. (b) The 4f setup is experimentally implemented by aligning a grating and the cylindrical mirror in one axis. The laser pulses are dispersed by the grating and have a beam path slightly downwards to the cylindrical mirror. After being deflected on these mirrors, the pulses are deflected on a folding mirror (fol. mir) into the Fourier plane. Afterwards, the same experimental setup of folding mirror, cylindrical mirror and grating is used to recollimate the laser pulses.

the first grating, the laser spectrum is imaged in the Fourier plane between the two lenses. The second grating transforms the spatially dispersed spectrum to its original distribution.

The used experimental implementation is slightly different (Figure III.2b). Firstly, the lenses are replaced by cylindrical mirrors to prevent the chirp imprinted by the lenses on the laser pulses. Furthermore, the cylindrical mirror (f=35 cm customized by Hellma Optics) and blazed grating (600lines/mm; Thorlabs GR25-0608) are aligned in one axis in order to achieve higher stabilities [84]. This is accomplished by inserting the cylindrical mirrors slightly below the gratings permitting the laser pulses to path these mirrors above. In accordance with this alignment, the beam path of the pulses is slightly tilted downwards on

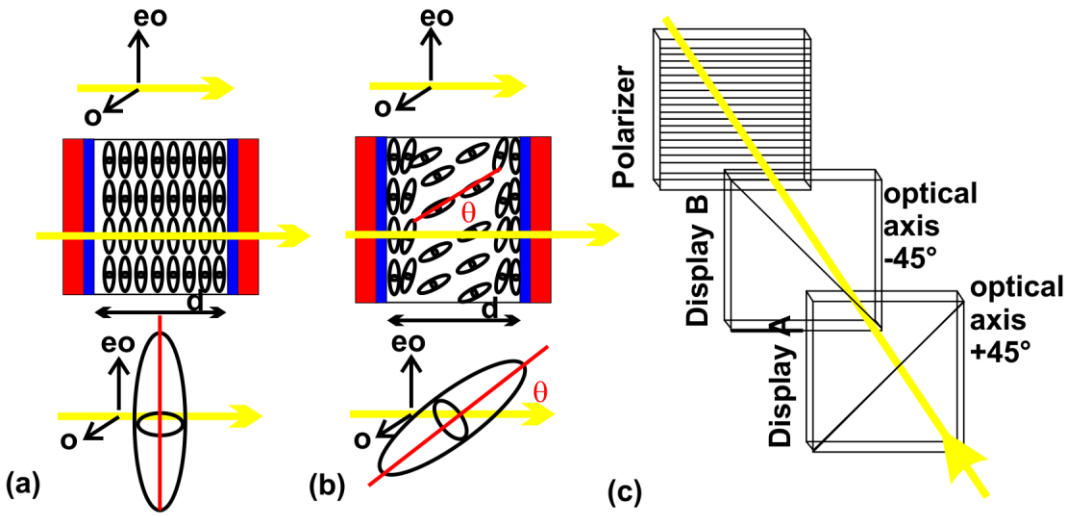

Figure III.3 Principle of a liquid crystal (LC) pulse shaper: (a) Each LC display consists of birefringent crystals wedged between glass substrates with electrodes (red) and an additional layer (blue). The phase shift of light polarized in ordinary (o) and extraordinary (eo) direction is affected by different phase shifts (b). If a voltage is applied on the electrodes, the birefringent crystals are rotated to the angle θ and the refractive index in extraordinary direction is varied. (c) For simultaneous polarization and phase shaping two LC masks with optical axis being perpendicular to each other are needed. For amplitude and phase shaping, an additional polarizer is placed behind the masks.

the grating and the pulses are reflected on the top part of the cylindrical mirrors. Furthermore, a folding mirror is inserted in the beam path behind the cylindrical mirrors to deflect the laser pulses by 90° into the Fourier plane (customized by Hellma optics). Afterwards, the dispersed laser pulses are confined by the same setup consisting of grating, folding and cylindrical mirror. For more information on the detailed setup see [55, 76].

2 ii. Pulse shaper

In the presented setup, pulse shaping is accomplished by a liquid crystal pulse shaper (SLM 640d Jenoptik), which uses a mask consisting of 640 pixels (individual width: 97 µm; separation: 3 µm). Each pixel consists of liquid crystals which are embedded between two glasses, coated each with an indium-tin oxide electrode layer and an additional layer.

These crystals are birefringent and disperse the transmitting light by an individual and arbitral phase shifts with respect to the refractive index n_o and n_{eo} in ordinary and extraordinary polarization, respectively (eq. III.2). The ordinary polarization is perpendicular to the plane spanned by optical axis of the crystals and the wave vector (Figure III.3 a & b). The polarization in extraordinary direction is inside this plane as already discussed in section II.2 ii a. Whereas light polarized in ordinary direction is affected by the constant phase $\varphi_0 = \frac{2\pi d}{\lambda} n_o$, light polarized parallel to this plane is imprinted by a variable phase shift $\varphi = \frac{2\pi d}{\lambda} n_{eo}(\theta)$[1], which depends on the angle θ (see eq. II.23 in section II.2 ii

[1] d: thickness of mask

a). This angle and the relative phase shift $\Delta\varphi(\theta)$ can be modified by applying different voltages on the electrodes (eq. III.1):

$$\Delta\varphi(\lambda, U) = \frac{2\pi d}{\lambda}\Big(n_{eo}\big(\lambda, \theta(U)\big) - n_o(\lambda)\Big), \tag{III.1}$$

$$\frac{1}{n(\lambda,\theta)^2} = \frac{\cos(\theta(U))^2}{n_o(\lambda)^2} + \frac{\sin(\theta(U))^2}{n_{eo}(\lambda)^2}. \tag{III.2}$$

This phase shift is maximized without any applied voltage by orienting the optical axis of the crystals along the polarization of the light (Figure III.3a). While increasing the voltage on the electrodes, the relative phase shift is reduced by rotating the crystals (Figure III.3b). In order to imprint no additional phase on the electromagnetic field, the crystals are rotated 90° by applying the highest voltage.

A single liquid crystal mask allows only for adjusting the phase of the transmitted light. Simultaneous polarization and phase shaping is accomplished by two masks, whose optical axes are aligned 90° to each other and 45° to the incoming light (Figure III.3c). These masks provide the polarization and phase shaping $\Phi(\Delta\varphi_1, \Delta\varphi_2)$ by the difference and sum of the individual phase shifts $\Delta\varphi_1$ and $\Delta\varphi_2$, respectively. In addition, polarization shaping can be switched to amplitude shaping $A(\Delta\varphi_1, \Delta\varphi_2)$ by inserting a polarizer behind the two masks (Figure III.3c):

$$A(\Delta\varphi_1, \Delta\varphi_2) = \cos\left(\frac{\Delta\varphi_1 - \Delta\varphi_2}{2}\right), \tag{III.3}$$

$$\Phi(\Delta\varphi_1, \Delta\varphi_2) = \frac{\Delta\varphi_1 + \Delta\varphi_2}{2}. \tag{III.4}$$

IV. Shaper-based narrowband and tuneable mid-infrared light source

1. Introduction

MIR spectroscopy has provided a tremendous impact in material and life sciences in the last decades [85, 86]. In life sciences, for example, MIR spectroscopy has been used to discriminate between tumorous and healthy tissue by detecting structural changes of proteins [87]. Furthermore, it is a potential candidate for diabetes healthcare via the implementation of a continuous glucose monitoring system [88-90]. The impact of MIR spectroscopy is also shown on its key role in the fight against marine pollution due to its potential to identify microplastics in sea water.[91, 92]

Globars are probably the most used MIR light source in the last decades due to their broad spectral range. In addition, a high spectral resolution is gained by using them in Fourier-transform infrared (FTIR) spectrometers [93, 94]. However, the emission of globars in the 4π-sphere reduces the signal intensities dramatically and hinders quick detection. Quantum cascade lasers [95] and difference-frequency-based laser sources [96] overcome this problem by offering higher signal intensities. In particular, the difference-frequency method is a powerful way to obtain MIR spectra with a wide range of implementations.

These implementations range from non-collinear optical parametric amplification (NOPA) systems generating ultrashort laser pulses [97, 98] to optical parametric oscillators (OPO), which provide narrowband, tuneable MIR spectra [99, 100]. Another interesting and modern method is the generation of MIR pulses using an intrapulse DF process in a single-beam setup [59, 101, 102].

These MIR pulses are usually implemented with either a broad or narrow MIR spectrum (Figure IV.1 a & b). Using thin crystals, the generated MIR spectra span a broad spectral range but with potentially weak spectral intensity. This can be addressed by using thick crystals to generate intense and narrowband MIR spectra, which require a tuning to probe different transitions. Both experimental schemes are static, and a switching of the spectrum from broad to narrowband requires a replacement of the crystal.

A pulse shaper offers the flexibility of both implementations in one setup by exploiting an intrapulse DF process in a thin crystal. The switching between the broad and narrow MIR spectrum, and even the tuning of the narrowband one, is achieved by simply shaping the involved laser pulses without any additional mechanical adjustment (Figure IV.1c). This enables the implementation of a new MIR light source, which flexibly offers MIR spectra with arbitrary spectral and temporal shapes.

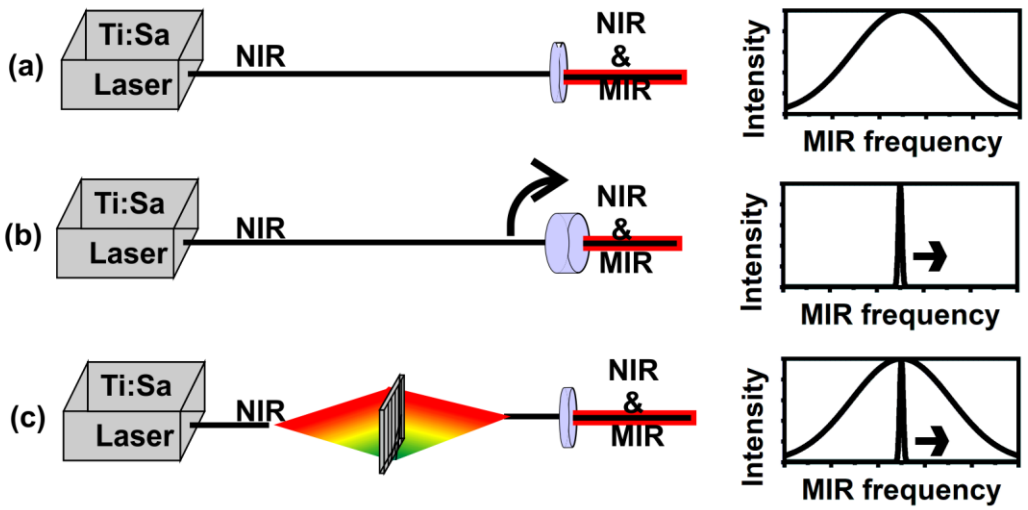

Figure IV.1 Experimental schemes for direct MIR generation. (a & b) The generated MIR spectrum in the critical phase matching regime can be varied by the crystal thickness: either (a) a broad or (b) narrowband MIR spectrum is generated by a thin or thick crystal, respectively. A tuning of the narrowband spectra is accomplished by tilting the DF crystal. (c) The flexible pulse shaping of the driving laser pulses can generate both spectra. They are switched by simply adjusting the imprinted phase without any mechanical changes on the setup.

The narrowband and tuneable MIR spectra in particular have a huge potential for MIR transmission spectroscopy since expensive MIR spectrometers are not needed. When using a single-channel detector, a MIR transmission spectrum can be recorded by tuning the narrowband MIR spectra.

In this chapter, the implementation of a narrowband and tuneable MIR light source is demonstrated via the following sections: Section 2 presents the method of using the shaper-based concept to tune broad MIR spectra to narrowband and tuneable ones. Afterwards, section 3 presents the crystal, generating these MIR spectra, and highlights its important properties to accomplish a broad MIR tuning range. Section 4 describes the experimental details of the setup in order to show how the implementation of the new MIR light source is accomplished. The potential of the new MIR light source is determined in section 5 with respect to their spectral tuneability (5 i) and spectral resolution (5 ii). Finally, FTIR spectroscopy is implemented in the shaper-based setup, which provides all necessary steps simply with flexible pulse shaping (section 6). Parts of the results were already published in Brückner *et al.* [3] and Müller *et al.* [1].

2. A tuneable narrowband MIR light source for MIR transmission spectroscopy

The implementation of a narrowband MIR light source is accomplished via spectral focusing [72], whose potential was already discussed for single-beam CARS spectroscopy (see section II.3 ii). This concept can be also applied to control the MIR generation in the intrapulse DF process by shaping the driving pulse (for more information about the DF generation, see section II.2 ii). In accordance with spectral focusing, this driving laser pulse is stretched in time and is split in pump and Stokes by imprinting parabolic phases via the pulse shaper. Having the same amount of chirp, a constant instantaneous frequency difference between pump and Stokes is provided (blue in Figure IV.2a) and a narrowband MIR spectrum centred at the applied instantaneous frequency difference is generated inside the crystal (blue in Figure IV.2c). In the scan of this frequency difference, the narrowband MIR spectrum is tuneable within the broad range of the transform-limited generated MIR spectrum (red in Figure IV.2c). Therefore, a complete MIR transmission spectrum can be acquired in the scan by detecting the MIR intensity after sampling with a single-channel detector.

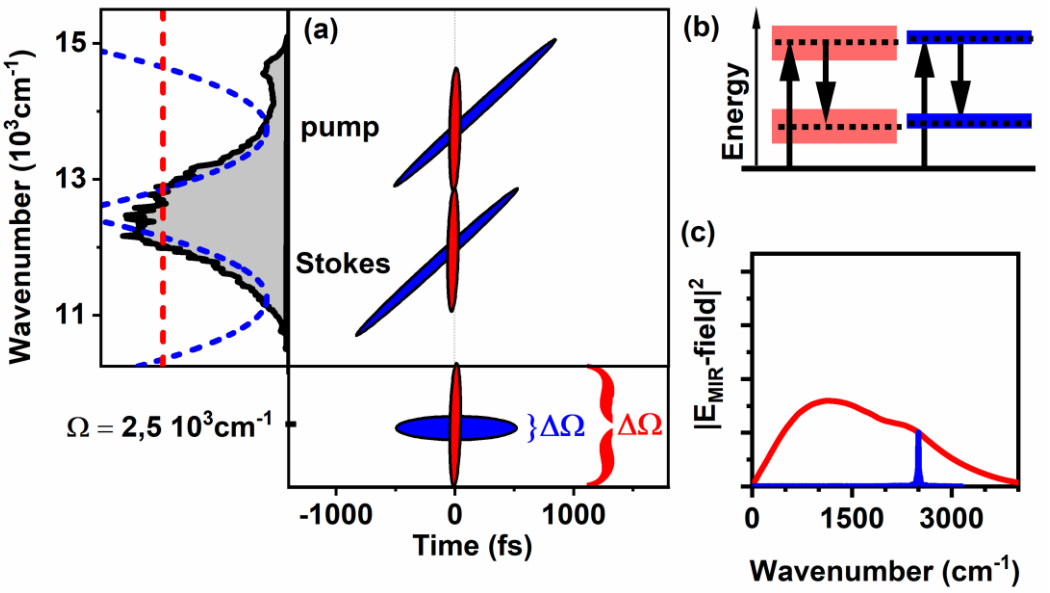

Figure IV.2 (a) For broadband MIR generation, a constant phase (red line on the left) is applied on the NIR spectrum (grey background on the left). The laser pulse (red in the main panel) is short and generates a broad MIR spectrum (red in the lower panel). In spectral focusing, the parabolic phase function (blue on the left) stretches the pulses linearly (blue in the main panel) and a narrowband DF excitation is generated (blue in the lower panel). (b) The schematic mechanism of broadband (left) and narrowband (right) MIR generation is presented. (c) The short laser pulses generate a broad MIR spectrum (red). By applying the phase of the spectral focusing concept with an instantaneous frequency difference (IFD) of 2500 cm^{-1}, a narrowband MIR spectrum is generated at the IFD (blue). The MIR spectrum is tuneable in the boundaries of the MIR spectrum generated by a constant phase of the NIR pulse.

3. Difference-frequency crystals

The generation of MIR pulses is carried out experimentally in the existing non-linear microscopy setup, which is based on a Ti:Sa oscillator. In order to use the MIR pulses in combination with the other spectroscopic techniques in this setup, the DF process must be driven by the same 800 nm centred laser pulses. However, the wavelength of these laser pulses greatly restricts the number of available crystals. Many crystals are limited in UV transparency and cannot be used because of the crystal damage caused by the two-photon absorption of the driving pulses [103, 104]. The best choice is a negative uniaxial $LiIO_3$ crystal, whose potential to generate MIR pulses with a broad spectrum and high intensity is shown in this section.

Firstly, this crystal is investigated with respect to phase matching (see section II.2 ii a). The $LiIO_3$ crystal requires Type I phase matching in order to efficiently generate MIR pulses (Figure IV.3). In this configuration, the pump and Stokes are polarised along the extraordinary and ordinary axis, respectively. In addition, the phase matching angle must be optimized to provide a small wave vector mismatch $\Delta k \sim 0$ (see eq. II.22) [105]. The phase matching angle is around 20° and varies smoothly in dependence on the MIR frequency if a pump wavelength at 800 nm is used (see Figure IV.4a) [106, 107]. This small variation (3°) provides a broad phase matching in the wavelength range between 2 µm and 9 µm.

The phase matching condition can be understood more quantitatively by the coherence length $L_C \equiv \frac{2}{\Delta k}$ defining the largest crystal length, which preserves just a phase matching by $\mathrm{sinc}(\frac{\Delta k L}{2}) \approx 1$ (eq. II.20) [102]. This coherence length is calculated for a Stokes wavelength of 850 nm and two different phase matching angles. In these results (Figure IV.4b), a coherence length above 100 µm over the whole MIR region and above 500 µm in a spectral range over 500 cm^{-1} is shown for both angles.

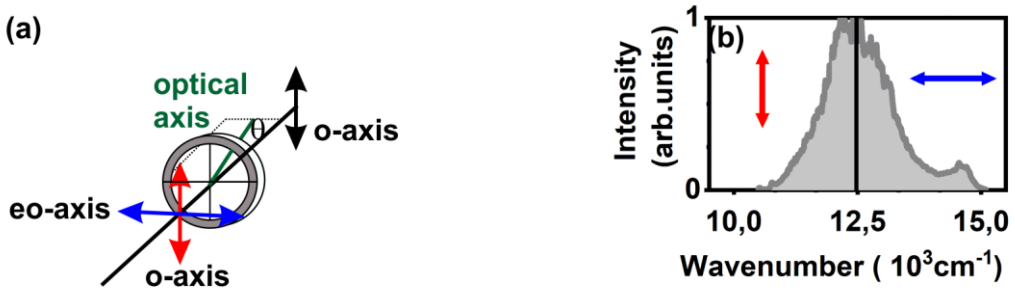

Figure IV.3 (a) Phase matching in the $LiIO_3$ crystal is acquired by the phase matching angle θ, which is in the plane of the beam wave vector and the optical axis. The pump is polarized in extraordinary (eo) axis inside this plane. The Stokes is polarized in ordinary (o) direction perpendicular to this plane. (b) In intrapulse DF generation, a single laser pulse provides the pump and Stokes, which are the blue and red parts of the spectrum, respectively.

In addition, the phase matching of a broadband pump and Stokes is determined for a coherence length of 1 mm (see Figure IV.4c & d). The graphs show a broad spectral range fulfilling the phase matching. Thus, a broad MIR spectrum is also generated in a 1 mm thick crystal, especially when the slight difference of the phase matching angles (19,7° and 20,0°) is within the angular distribution of the incoming laser beam and merges the MIR generation at different angles. This is usually provided by the aperture angle of the focusing lens.

Beside the phase matching condition, the temporal overlap between the pump and Stokes in the $LiIO_3$ crystal is also an important condition for optimal MIR generation. So-called pulse splitting is prevented if the group velocities of pump v_P and Stokes v_S do not differ strongly in the crystal. This condition is expressed quantitatively by the group velocity

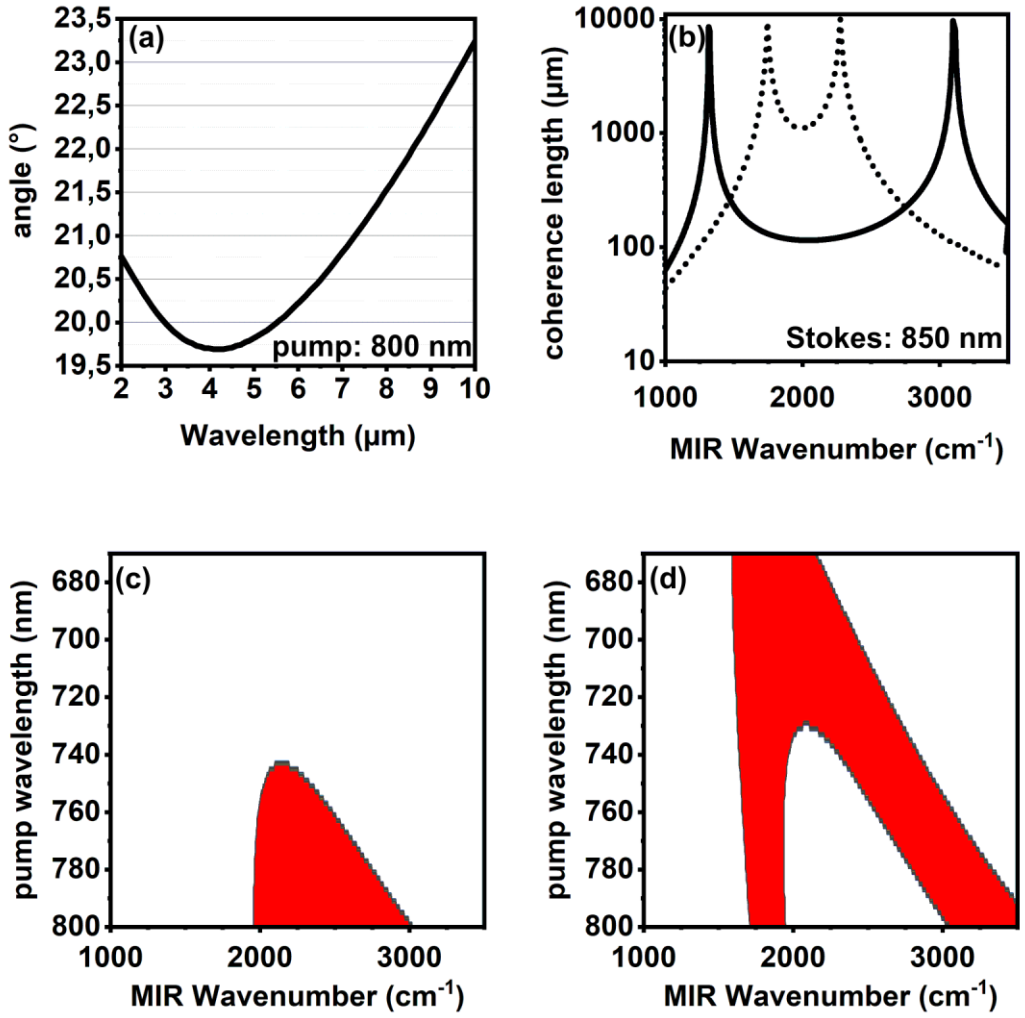

Figure IV.4 Optical properties of $LiIO_3$ crystals in relation to DF generation: (a) The collinear phase matching angle (pump 800 nm) varies in dependence on the MIR wavelength only between 19,7° and 23° over a range of 8 µm (4000 cm^{-1}). (b) The coherence length (Stokes 850 nm) is above 100 µm (500 µm) over 2000 cm^{-1} (500 cm^{-1}) for a phase matching angle of 20° (dotted line) and 21° (solid line). (c & d) In accordance with the coherence length, the fulfilled phase matching condition (red area) in a 1000 µm thick $LiIO_3$ crystal is demonstrated at a phase matching angle at 19,7° (c) and 20,0°(d).

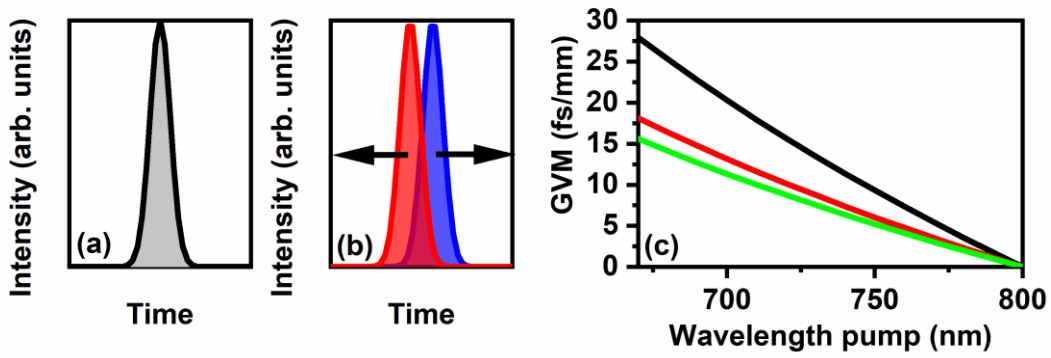

Figure IV.5 Group velocity mismatch (GVM) of $LiIO_3$ crystals. (a & b) Pump and Stokes are delayed to each other in the birefringent material since their polarization is different in relation to the Type I phase matching. (c) Generating MIR pulses with a centre frequency at 1750 cm^{-1} (green), 2000 cm^{-1} (red), and 3000 cm^{-1} (black), the group velocity mismatch is even for a 1 mm crystal below 15 fs, 20 fs, and 27 fs, respectively.

mismatch δ_{P-S} (eq. IV.1; pump: υ_P and Stokes υ_S), which can be interpreted as the time delay of the pulses per unit length [51, 58]:

$$\left|\frac{1}{\delta_{P-S}}\right| = \left|\frac{1}{\upsilon_P} - \frac{1}{\upsilon_S}\right|. \qquad \text{IV.1}$$

For $LiIO_3$ crystals, the group velocity mismatch is below 30 fs/mm for the whole frequency range and is even less than 20 fs/mm for a generated MIR frequency below 2000 cm^{-1} (Figure IV.5). This small mismatch demonstrates an efficient MIR generation in $LiIO_3$ crystals with a thickness up to 1 mm since all obtained values of the time delay between pump and Stokes are in the order of the temporal width of the laser pulses (FWHM=10 fs).

The following question may arise: why should the pulse splitting be considered in the generation of narrowband MIR spectra? In order to generate narrowband MIR pulses, the pulses are stretched up to several picoseconds, and the shift of the Stokes and pump by the dispersion is small compared to the pulse length. However, this temporal shift induces an additional tuning of the MIR spectrum by changing the instantaneous frequency difference. This change leads to an unwanted broadening of the narrowband MIR spectrum.

Furthermore, the generation of MIR pulses also depends on the focusing condition into the non-linear crystal. These technical details are explained in the appendix (see section IX.3).

4. Experimental setup for MIR generation

The MIR generation is driven by ultrabroadband NIR pulses (Figure IV.6). These 800 nm centred, sub 10 fs NIR laser pulses are provided by a Ti:Sa oscillator and guided

into a 4f setup. A two-mask liquid crystal pulse shaper is located in its Fourier plane, which shapes the laser pulses in phase as well as polarisation (for more details, see chapter III).

Afterwards, the shaped laser pulses are guided into the MIR generation part and are focused with a parabolic mirror (f=10 cm) into a $LiIO_3$ crystal. In accordance with the Type I phase matching condition, the pump and Stokes part of the NIR pulses are polarised perpendicular to each other.

The MIR pulses are generated in 100 µm, 500 µm, and 1000 µm thick $LiIO_3$ crystals that have a power of 5 µW, 16 µW, and 22 µW, respectively. They are measured by an MCT detector (InfraRed Associates 13-2.0), which was calibrated by detecting the power of a MIR-NOPA [108] with the MCT detector behind a ND2 filter and a calibrated power metre (Coherent PS 10) as reference. The results obtained reflect those of Zentgraf *et. al.* [102], which further corroborates the measured powers.

After the MIR generation, the NIR and MIR laser pulses are collimated by a parabolic mirror (f =5 cm) and are guided to the detection part. Detection is made by focusing the MIR pulses with a spherical mirror (f =15 cm) on the single-pixel MCT detector, which was calibrated beforehand. In order to detect the MIR pulses without any interference, the fundamental laser pulses are blocked by a thick MIR-anti-reflection-coated germanium substrate (Edmunds Optics #62-645) in front of the detector. The signal on the MCT detector is electronically amplified by a preamplifier, which requires chopping the MIR pulses. Although the signal is chopped while spatially separated from the detector, small amounts of noise are also modulated and observed on the detector. To avoid this noise, the NIR pulses are chopped before the MIR generation and a MIR-absorbing glass substrate is placed behind the chopper to absorb the MIR noise. The dispersion imprinted by the glass on the NIR pulses is pre-compensated by the pulse shaper.

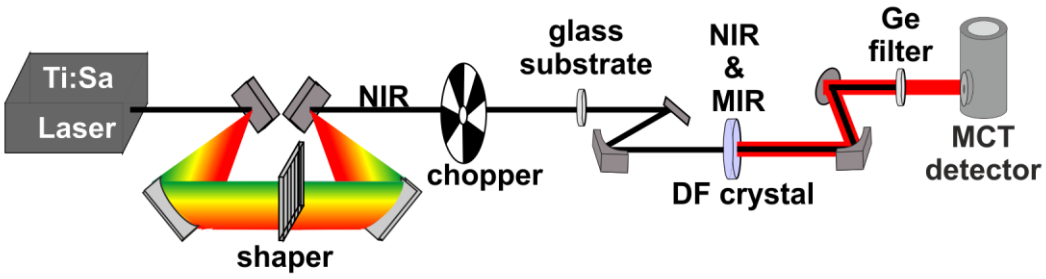

Figure IV.6 The experimental scheme for MIR generation consists of a Ti:Sa laser, a pulse-shaper setup, and a MIR generation stage. The sub 10 fs laser pulses are shaped in polarization and phase by a liquid crystal pulse shaper inside a 4f setup. These laser pulses generate MIR light in the DF crystal ($LiIO_3$). The MIR light is detected by an MCT detector after suppressing the fundamental NIR pulses with a germanium filter. In correspondence with the MCT, the MIR pulses are chopped. The chopper reflects MIR light that originates from the environment on the detector. This is blocked by a glass substrate before the MIR generation. The phase of the glass substrate is compensated by the pulse shaper.

5. Characterization of the narrowband and tuneable MIR light source

The narrowband and tuneable MIR light source is characterised by measuring the MIR transmission of a polystyrene reference film. As an example, the transmission taken with a high amount of chirp (15000 fs^2) is depicted (black in Figure IV.7). It shows the specific polystyrene absorptions corresponding well with reference measurements obtained by a FTIR spectrometer (the grey background). By identifying the polystyrene absorption, a tuning of the MIR light source from 1250 cm^{-1} up to 3500 cm^{-1} is demonstrated (section 5 i). Furthermore, a small difference between the MIR transmission with respect to the reference is shown. This can be explained by the spectral resolution, which is discussed in detail in section 5ii.

5 i. Spectral tuneability

The tuning of the narrowband MIR spectrum is observed by scanning the frequency of this spectrum and detecting the MIR light without any sample. The obtained broad spectrum determines the tuning range and is called the envelope spectrum. Due to the dependence of this tuning range on the crystal thickness, the envelope spectrum is investigated for the MIR generation by a 100 µm (a) and 500 µm (c & d) thick $LiIO_3$ crystal (Figure IV.8).

The bandwidth of the envelope spectrum generated in the 100 µm thick $LiIO_3$ crystal ranges over 2000 cm^{-1}, from 1250 cm^{-1} to above 3250 cm^{-1} and does not significantly vary by slightly changing the phase matching angle. This contrasts with the tuning bandwidth of the envelope spectrum generated in the 500 µm thick crystal. The thick crystal limits the phase matching and shifts the envelope spectrum with respect to the phase matching angle, as shown for two envelope spectra acquired at different phase matching angles (Figure IV.8c & d). Whereas the first angle maximises the MIR intensity generated by a transform-limited NIR pulse and has a tuning range between 1750 cm^{-1} and 3250 cm^{-1} (c), the second one maximises the MIR power at 3000 cm^{-1} (d). The envelope spectrum in the latter case

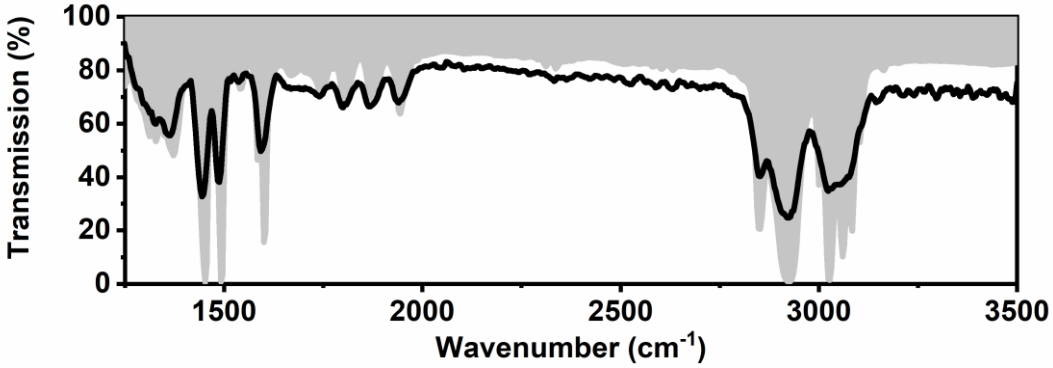

Figure IV.7 The Polystyrene transmission spectrum obtained by the new MIR light source shows a broad tuneability from more than 2000 cm^{-1} and a high spectral resolution (solid line). The MIR transmission spectrum is acquired using the concept of spectral focusing with an imprinted amount of chirp of 15000 fs^2. For comparison, the MIR transmission is also taken by a FTIR spectrometer with a resolution of 1 cm^{-1} (grey background).

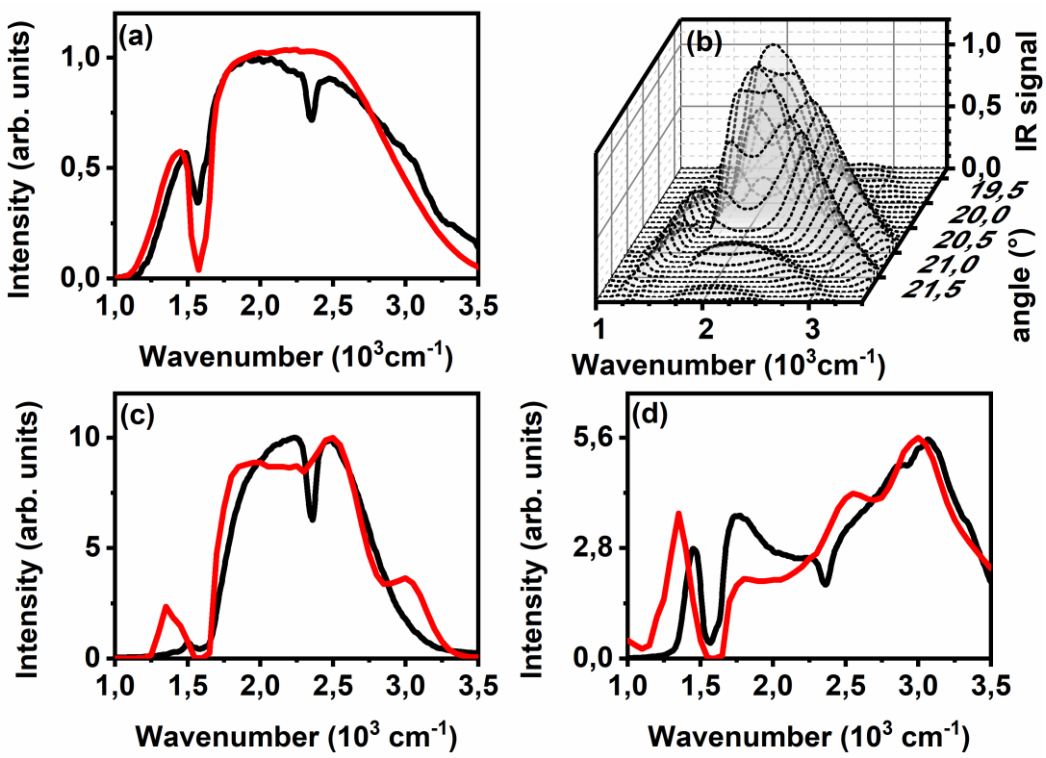

Figure IV.8 Tuning range of the narrowband MIR spectra generated in a 100 µm (a) and 500 µm (b-d) thick $LiIO_3$ crystal. (a) The tuning range of the MIR spectra generated in a 100 µm thick $LiIO_3$ crystal (black) ranges from 1250 cm^{-1} up to 3250 cm^{-1} and corresponds well with simulations done at a phase matching angle of 19,8° (red). (b) The simulated MIR spectra generated in a 500 µm thick $LiIO_3$ crystal are depicted in their dependence on the phase matching angle and show a shift towards larger MIR frequencies by increasing the phase matching angle. (c) The measured (black) and simulated (red) tuning bandwidth of the MIR spectra generated in the 500 µm thick crystal is more narrowband than the 100 µm thick crystal. (d) By shifting the phase matching angle, this bandwidth is increased. (a-d) Simulation and measurement use phases with an amount of chirp of 5000 fs^2 in the spectral focusing concept. The measurements are corrected by the spectral response of the MCT detector and the transmission of the germanium filter. The simulation takes the measured NIR spectrum and phase matching, as well as thickness and transmission of the crystal into account. Contrary to the simulation, the known CO_2 absorption at 2350 cm^{-1} is observable in the measurement. (c & d) The measured and simulated MIR spectra of the 500 µm thick $LiIO_3$ are scaled relatively to the MIR intensity of the 100 µm thick crystal. For (a): Adapted with permission from [3]. For (b): Reproduced from [1], with the permission of AIP Publishing.

has a broader bandwidth, ranging from 1500 cm^{-1} up to 3500 cm^{-1}, and the highest MIR intensity is shifted towards higher and lower frequencies. Therefore, this envelope spectrum has the same tuning range as the envelope spectrum generated in a 100 µm thick crystal with a five times higher MIR intensity in the CH stretching region.

In order to corroborate the measurements, they are also modelled by simulations. In the model, the complex electric fields of the NIR pulses consists of the measured NIR spectrum and of the imprinted phase with respect to the spectral focusing concept. This phase takes the pixelation of the pulse shaper into account and splits the simulated NIR laser pulse into pump (E_{pump}) and Stokes (E_{Stokes}). In the DF process, they generate a narrowband MIR

spectrum with the electric field E_{MIR} (eq. IV.2) in consideration of the phase matching condition $Z(\omega, \Omega, L)$ with the crystal thickness L and wave vector mismatch Δk (eq. IV.3) [58, 59]. After tuning the MIR spectrum, the acquired envelope spectrum is modified by the $LiIO_3$ transmission $T_{LiIO3}(\Omega, L)$:

$$E_{MIR}(\Omega, \mathrm{L}) \propto T_{LiIO3}(\Omega, L) \times \int d\omega\, E_{pump}(\omega) \cdot E^*_{Stokes}(\omega - \Omega) \cdot Z(\omega, \Omega, L), \qquad \text{IV.2}$$

$$Z(\omega, \Omega, L) = \int_0^L e^{i\Delta k(\omega,\Omega)z} dz = \frac{1}{\mathrm{i} \cdot \Delta k(\omega, \Omega)} (e^{i\Delta k(\omega,\Omega)L} - 1). \qquad \text{IV.3}$$

The envelope spectrum modelled with a phase matching angle of 19,8° corresponds well with the measurement obtained by the 100 µm thick $LiIO_3$ crystal (Figure IV.8a). However, modelled envelope spectra with a specific phase matching angle cannot describe the two measured spectra generated in the 500 µm thick crystal (not shown). In order to understand this, their dependence on the phase matching angle must be considered. In contrast to the MIR generation in the 100 µm thick crystal, the shape of the envelope spectra generated in the 500 µm thick crystal varies much stronger in dependence on the phase matching (Figure IV.8b). Therefore, the aperture angle of the parabolic mirror, which focuses the driving pulses in the crystal and offers a distribution of phase matching angles, is no longer negligible. Taking this angular distribution into account, each of the two measured MIR spectra can be modelled by a summation of MIR spectra at different phase matching angles. In a fit, the MIR spectra (angle: 20,0°–20,6°) are obtained, whose summation corresponds well with the measurement in Figure IV.8c. The best fit in accordance with the measured MIR spectrum in Figure IV.8d accounts for the MIR spectra with an angle from 20,5° to 21,5°.

5 ii. Spectral resolution

Spectral focusing has the potential to flexibly adapt the bandwidth of the narrowband MIR spectra. This is shown on the transmission spectra of the polystyrene film by imprinting different amounts of chirp (Figure IV.9a). With a small amount of chirp (black), the obtained MIR transmission is unable to resolve the vibrational modes of polystyrene, which can be clearly seen by FTIR reference measurements (dotted line). Increasing the imprinted amount of chirp to 3000 fs^2 indicates broad absorption peaks at 1450 cm^{-1} and 1600 cm^{-1}, as well as absorption at 2900 cm^{-1} and 3050 cm^{-1}. The spectral resolution is further increased by tuning the imprinted amounts of chirp even to 10000 fs^2 (green) and 12500 fs^2 (blue).

For a more quantitative analysis, the MIR transmission spectrum T_{meas} (Ω) is expressed as convolution of a molecular response (MRF) and a Gaussian-shaped instrument response (IRF) function (eq. IV.4-IV.6). Although the MRF is not known, the FTIR reference measurement (PerkinElmer spectra 400) taken with high spectral resolution (1 cm^{-1})

provides a sufficient approximation. The spectral width of the IRF can be obtained by fitting the convolution to the measurement:

$$T_{meas}(\Omega) = Conv\big(MRF(\Omega), IRF(\Omega)\big), \tag{IV.4}$$

$$T_{meas}(\Omega) = \int MRF(\Omega - \omega) \cdot IRF(\omega) d\omega, \tag{IV.5}$$

$$IRF(\omega) \propto \frac{4\ ln(2)}{\mathrm{FWHM}^2} \cdot exp\left(-4\ ln(2) \cdot \left(\frac{\omega}{\mathrm{FWHM}}\right)^2\right). \tag{IV.6}$$

After obtaining the FWHMs of the IRF in a low-frequency range (1400–1900 cm^{-1}) and a high frequency range (2800 cm^{-1}–3200 cm^{-1}), they indicate a decrease from above 100 cm^{-1} for both spectral regions down to 20 cm^{-1} and 30 cm^{-1} for the low and high frequency region, respectively (Figure IV.9c).

In order to understand the decrease of the best spectral resolution for higher MIR frequencies, it is important to know that the MIR spectra around 3000 cm^{-1} are generated at the wings of the NIR spectrum. Furthermore, the pixel density in the blue wing of the spectrum must be considered since it is smaller than the density in other parts of the spectrum due to the nearly linear wavelength distribution over the pulse shaper. Therefore, high amounts of chirp cannot be efficiently imprinted by the Nyquist theorem in the blue wing of the spectrum.

In summary, the tuneable and narrowband MIR light source is able to generate MIR spectra that have a spectral width down to 20 cm^{-1} and are tuneable over more than 2000 cm^{-1}. This entails new potential applications like combined MIR and CARS microspectroscopy (chapter V) and SF spectroscopy (chapter VI).

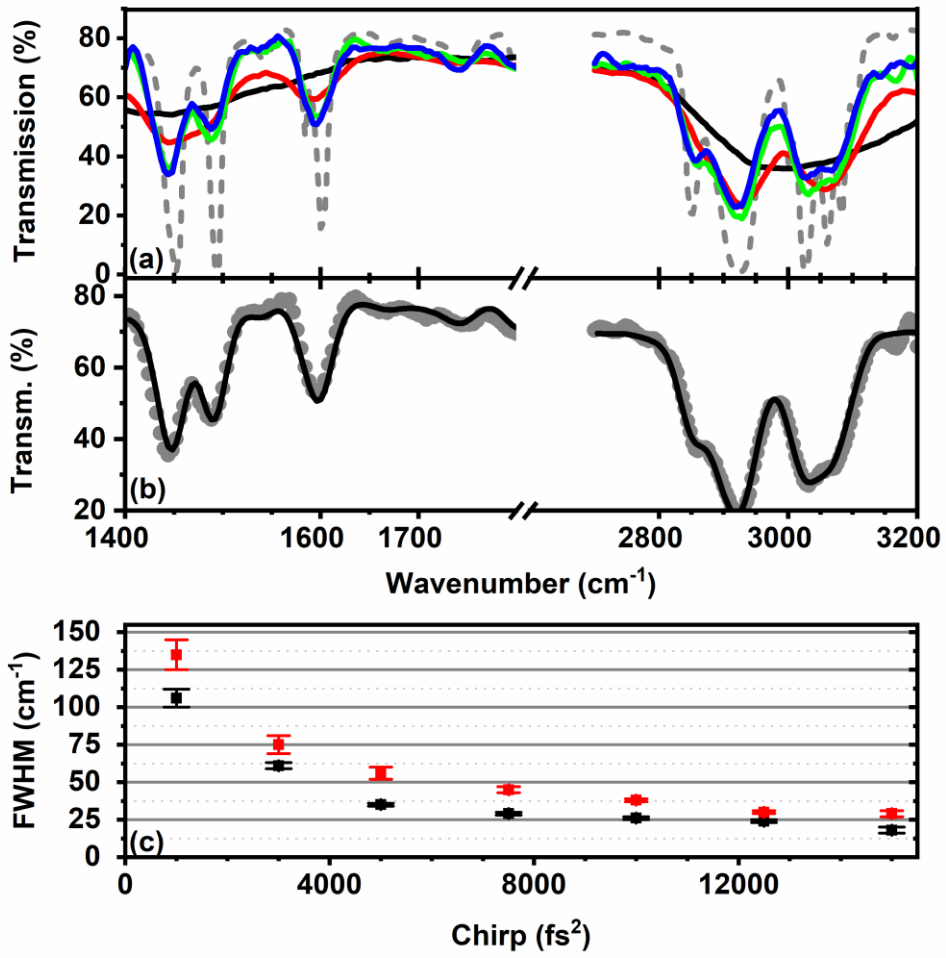

Figure IV.9 The spectral resolution of the narrowband MIR light source can be determined on polystyrene vibrational modes. (a) In the low-frequency range (1400 cm^{-1}–1900 cm^{-1}) and in the high frequency range (2800 cm^{-1}–3200 cm^{-1}), transmission spectra of a polystyrene reference film show an increase in spectral resolution by an increasing amount of chirp from 1000 fs^2 (black), over 3000 fs^2 (red), 10000 fs^2 (green) up to 12500 fs^2 (blue). A FTIR transmission measurement obtained with a resolution of 1 cm^{-1} is also shown (grey). (b) For a more quantitative analysis in the two frequency regions, the convolutions (solid line) of the molecular response (FTIR measurement) and instrument response function (Gaussian shape) are fitted to the MIR transmission spectra (dots: measured transmission). It is depicted for an imprinted amount of chirp of 10000 fs^2. (c) The FWHM of the instrument response function decreases for the low-frequency region (black dots) and the high frequency region (red dots) from above 100 cm^{-1} to below 20 cm^{-1} and 30 cm^{-1}, respectively. Adapted with permission from [3].

6. Additional approach: Difference-frequency based FTIR spectroscopy

FTIR spectroscopy is a powerful tool for analysing samples by their MIR transmission [109, 110]. This is accomplished in a Michelson interferometer by splitting the laser light and scanning the time delay. The spectral resolution in FTIR spectrometers is directly defined by the scan length in this Michelson interferometer.

In the shaper-based MIR setup introduced above (Figure IV.6a), FTIR spectroscopy can also be implemented by generating MIR double pulses via shaped NIR laser pulses. With the transfer function $M(\omega)$, the programmable pulse shaper splits the NIR pulses into two pulses. $M(\omega)$ on its turn consists of the amplitude $A(\omega)$ and phase $\varphi(\omega)$ (eq. IV.7 taken from eq. II.12):

$$M(\omega) = A(\omega)e^{i\varphi(\omega)} = \left|\cos(\omega\frac{\tau}{2})\right| e^{ia(\omega)} \qquad \text{IV.7}$$

$$\text{with } a(\omega) = \begin{cases} 0 & \text{if } \cos\left(\omega\frac{\tau}{2}\right) \geq 0 \\ \pi & \text{if } \cos\left(\omega\frac{\tau}{2}\right) < 0 \end{cases}.$$

After inserting a polariser behind the pulse shaper, amplitude shaping is implemented. Therefore, the polarisation cannot be adjusted by the pulse shaper for the conservation of phase matching. In order to still preserve phase matching, the $LiIO_3$ crystal (of a thickness of 100 µm) is rotated around 45° to provide half of the NIR intensity along the ordinary and

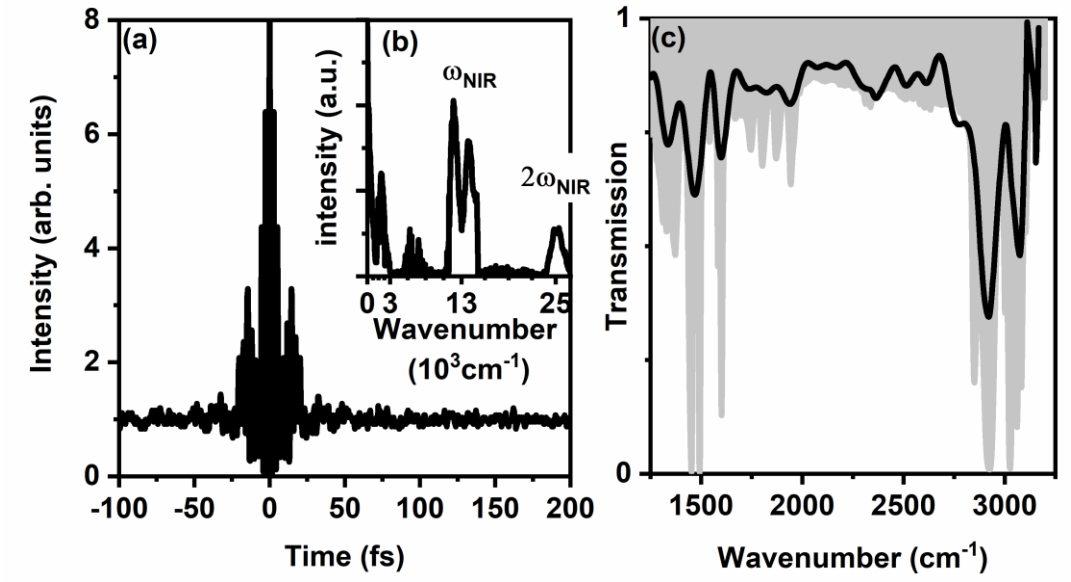

Figure IV.10 (a) In DF-based FTIR spectroscopy, MIR double pulses are generated via the pulse shaper, and an interference pattern is recorded by scanning the time delay. (b) The interferometric signal consists of three spectrally-separated components: the interferometric part at low frequencies known from conventional FTIR and the two spectral parts at the centre frequency ω_{NIR} and at the doubled centre frequency $2\omega_{NIR}$ of the NIR laser pulse. The MIR spectrum can be retrieved after isolating the low-frequency signal. (c) The DF-based FTIR corresponds well with the commercial one ($\Delta\upsilon$ = 1 cm^{-1}) in accordance with the reduced spectral resolution.

extraordinary axis. This results in only one fourth of the MIR intensity, which is generated without rotating the crystal.

The acquired time scan of the pulses displays an interferometric autocorrelation by the amplitude ratio of 8:1 and includes different contributions (Figure IV.10a). The major one is the MIR interferogram at low frequencies. Since the high-frequency contributions are spectrally separated, the FTIR spectrum can be extracted [111, 112].

The potential of the shaper-based FTIR method is demonstrated on a polystyrene sample (Figure IV.10c). Although the acquired transmission of the polystyrene film follows the reference measurement, the spectral resolution is low. With its definition through the temporal overlap, the spectral resolution is around 150 cm^{-1} since the temporal overlap is only over 200 fs observable. Due to these limitations, the tuneable, narrowband MIR light source provided by the spectral focusing concept is exploited in the following for several applications (chapter V and VI).

V. Single-beam Coherent Raman and mid-IR microspectroscopy

1. Introduction

CARS and MIR microspectroscopy are label-free methods for the detection of molecular vibrations. These methods have several complementary advantages and disadvantages. CARS microspectroscopy is a powerful method which combines vibrational sensitivity with high spectral resolution [21, 113-116]. However, the nonlinear process in CARS requires intense laser pulses that are not suitable for the investigation of samples with a low damage threshold [117]. In contrast, MIR microspectroscopy, with its linear process, has a much higher sensitivity over the whole spectral range although using lower intensities. Drawbacks compared with CARS are the worse spatial resolution in MIR microspectroscopy and its more challenging access to aqueous samples due to the strong water absorption.

The combination of CARS and MIR spectra merges the advantages and overcomes the disadvantages of the individual methods as has already been shown in material and life sciences [118-121]. However, it is important to note that in these applications the spectra are obtained using different setups. The implementation of both methods in one setup is a further advantage for microspectroscopy since both spectra and the respective images can be acquired at the same position.

The combination of both methods for microspectroscopy in one single-beam setup is demonstrated in this chapter. This is based on the new MIR light source, whose implementation was discussed in the preceding chapter (chapter IV). This light source provides MIR pulses with narrowband and tuneable spectra, which can be exploited inside the microscope. The MIR pulses are generated by shaped NIR pulses using the concept of spectral focusing. Additionally, these shaped NIR pulses can be used in the microscope directly to investigate the same sample by CARS microspectroscopy (see section II.2 iii).

In order to describe the potential and applications of combined MIR and CARS microspectroscopy, this chapter is divided into the following parts. First, the details of the experimental setup are discussed (section 2). Afterwards, spectroscopy (section 3) and microscopy (section 4) are demonstrated especially on polymers and human dermis. A part of the results presented were previously published in [1].

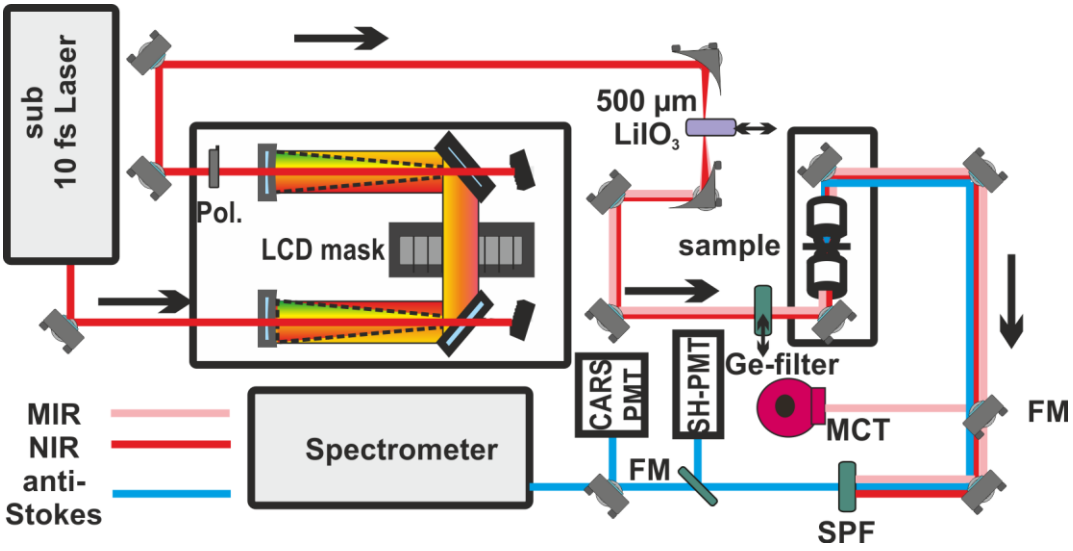

Figure V.1 Setup for combined MIR and CARS microscopy. Sub 10 fs NIR laser pulses are created by a Ti:Sa oscillator and guided into a 4 f setup for flexible pulse shaping by a liquid crystal pulse shaper. The shaped laser pulses generate MIR laser pulses in a 500 µm thick $LiIO_3$ crystal. Both laser pulses are focused by a Schwarzschild objective (BOS, 74x, NA 0.65) in the sample located on a piezo-driven stage. The NIR, MIR, and generated CARS signal is collimated by a 40x reflective objective and guided into the detection scheme. The MIR light is detected by an MCT detector and the CARS signal is detected after a 650 nm short-pass filter either by an intensity CCD camera or by a photomultiplier. To switch the setup from MIR to CARS spectroscopy, the $LiIO_3$ crystal and germanium filter (GE) are replaced by a polariser (Pol.) behind the shaper. In addition, a mirror (FM) in the detection path is flipped.

2. Experimental details for combined microspectroscopy

The setup for combined microspectroscopy consists of three parts (Figure V.1): a laser pulse generation part, a microscope, and a detection part. In the first part, the NIR and MIR pulses are generated by the already used shaper-based setup, which in this case has a 500 µm thick $LiIO_3$ crystal for MIR generation (see section IV.4.).

After their generation, the collinear NIR and MIR pulses are guided in the microscope and focused by a Schwarzschild objective (74x, numerical aperture [NA] 0.65, Beck Optronic systems), which transmits 85% of the incoming power into the sample. The laser pulses are recollimated afterwards by another Schwarzschild objective (40x, NA 0.4, Thorlabs). The sample is moved inside the microscope by a piezo-driven table (PI nano XYZ).

The detection of the signals is different for the two spectroscopic methods. An MCT detector is used for detection in the MIR transmission spectroscopy and the generated CARS signal is detected behind a 650 nm short-pass filter either by an intensity charged-coupled device (CCD) camera (Andor DH 501) or by a single-channel photomultiplier (Hamamatsu H9300 series). Whereas the camera offers higher sensitivities and is used for spectroscopy,

data acquisition in microscopy is done faster with a photomultiplier, which is equipped with a bandpass filter (640 ± 10 nm).

As already discussed, second-harmonic light is generated simultaneously with the CARS signal. A 2nd photomultiplier is inserted behind a bandpass filter at 400 nm (width: 10 nm) to detect this light.

It is important to note that, the MIR and CARS spectra are not acquired simultaneously for two reasons. One, the NIR and MIR pulses overlap temporally and also generate SF light in the sample, which coincides with the CARS signal spectrally and thus, cannot be distinguished. Two, the small damage threshold of many samples requires a reduction of the NIR power, which should be accomplished in the single-beam setup without decreasing the MIR intensities. This reduction cannot be provided by any optical substrate, so far as the author is aware.

Therefore, switching between the two spectroscopic methods is necessary. The setup is adapted for CARS spectroscopy by removing the $LiIO_3$ crystal and by inserting a polariser behind the pulse shaper. This polariser lowers in combination with polarisation shaping the power of the NIR pulses down to 50 mW. In MIR spectroscopy, a MIR-anti-reflection-coated germanium substrate is inserted in front of the microscope to block the NIR pulses. This substrate is tilted to a certain angle to compensate the small spatial shift between the NIR and MIR pulses caused by the spatial walk-off in the $LiIO_3$ crystal (see section IX.3).

The CARS and MIR spectra obtained in the single-beam setup are compared with reference measurements taken with an FTIR spectrometer (Perkin Elmer spectra 400) and a Raman microscope (Horiba XploRA Plus). These Raman spectra are acquired with an excitation wavelength at 532 nm.

3. Demonstration of combined MIR and CARS spectroscopy

The combined MIR and CARS spectroscopy is demonstrated by investigating a polystyrene film (section 3 i) and alkyne molecules (section 3 ii).

Before the MIR and CARS spectra are acquired, a constant phase of the NIR pulses must be preadjusted via the pulse shaper to imprint the right phases without any artefacts. In both spectroscopy methods, this constant phase is determined by shortening the NIR pulses in the optimization with an evolutionary algorithm. The MIR and CARS signals are through their nonlinear dependence on the NIR intensity the feedback signals, which increase with shorter NIR pulses.

3 i. Polystyrene

The MIR and CARS spectrum of the polystyrene film are recorded with an imprinted amount of chirp of 12500 cm^{-1} and 7000 fs^2, respectively (Figure V.2a). The MIR spectrum (blue) shows absorptions at 2920 cm^{-1} and 3050 cm^{-1}, which are linked to CH_2 and aromatic ring stretching, respectively [8]. The corresponding CARS spectrum indicates a strong non-resonant background, which is generated by the interaction of pump and Stokes without an

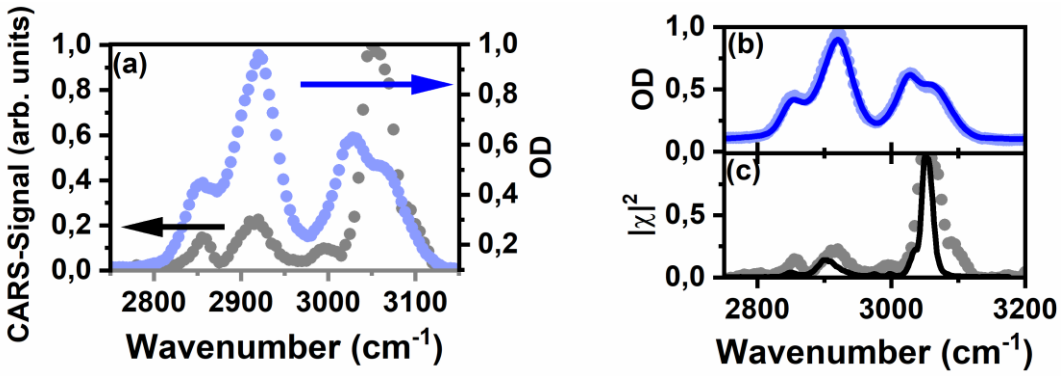

Figure V.2 Demonstration of combined MIR and CARS spectroscopy on a polystyrene film. (a) The CARS spectrum (grey dots) and MIR absorption spectrum (OD, blue dots) is detected by a narrowband DF excitation with a chirp of 7000 fs^2 (CARS) and 12500 fs^2 (MIR), respectively. The CARS spectrum is acquired with tailored spectral focusing extension via a probe delay at 200 fs after the end of the excitation. (b) The MIR absorption spectrum (blue dots) corresponds well with the FTIR reference (blue line), after accounting for the instrument response function of the MIR light source. (c) The CARS spectrum (grey dots) shows the same vibrational modes as the squared Raman spectrum (black line) acquired with a commercial microscope.

independent probe pulse (not shown). This background is supressed by delaying the probe pulse 200 fs after the end of excitation via tailored spectral focusing (for more details see section II.3 ii c). The background-free CARS spectrum also shows the two vibrational resonances located at 2920 cm^{-1} and 3050 cm^{-1} (grey in Figure V.2a). Furthermore, a vibrational mode at 2850 cm^{-1} is observed, which is only shown by a sideband in the MIR spectrum.

Spectra are taken with the FTIR spectrometer and Raman microscope to verify the recorded spectra. As already shown in section IV.5 ii, the instrument response function of the new MIR light source has a spectral width around 30 cm^{-1} and, thus, is worse than the resolution of the FTIR spectra ($\Delta\upsilon = 1\ cm^{-1}$). In order to provide a direct comparison between the two MIR spectra, the MIR spectrum obtained by the FTIR is adjusted by a convolution with the instrument response function of the new MIR light source. Afterwards, it is observed that the FTIR spectrum corresponds well with the measured MIR spectrum (Figure V.2b). The CARS spectrum also matches the square of the Raman spectrum (Figure V.2c). The pre-process of taking the square value accounts for the linear and quadratic dependence on the number of molecules for the Raman and CARS processes, respectively. It is important to note that this simple pre-process is only possible after supressing the non-resonant background. If this pre-process is not done, the resonant and non-resonant background must be disentangled using more sophisticated methods such as MEM retrieval (see section II.2 iii).

3 ii. Alkyne

The combined CARS and MIR spectroscopy are also demonstrated by detecting the C-C triple bond in 1- and 4-octyne. These molecules are prepared inside a CaF_2 cuvette with

a 50 µm-thick volume, and the dispersion of the top glass (1 mm thickness) is compensated by the pulse shaper for the CARS spectroscopy. The spectra of the molecules are detected by imprinting a chirp of 9000 fs^2 (MIR) and 7000 fs^2 (CARS) in the spectral focusing concept.

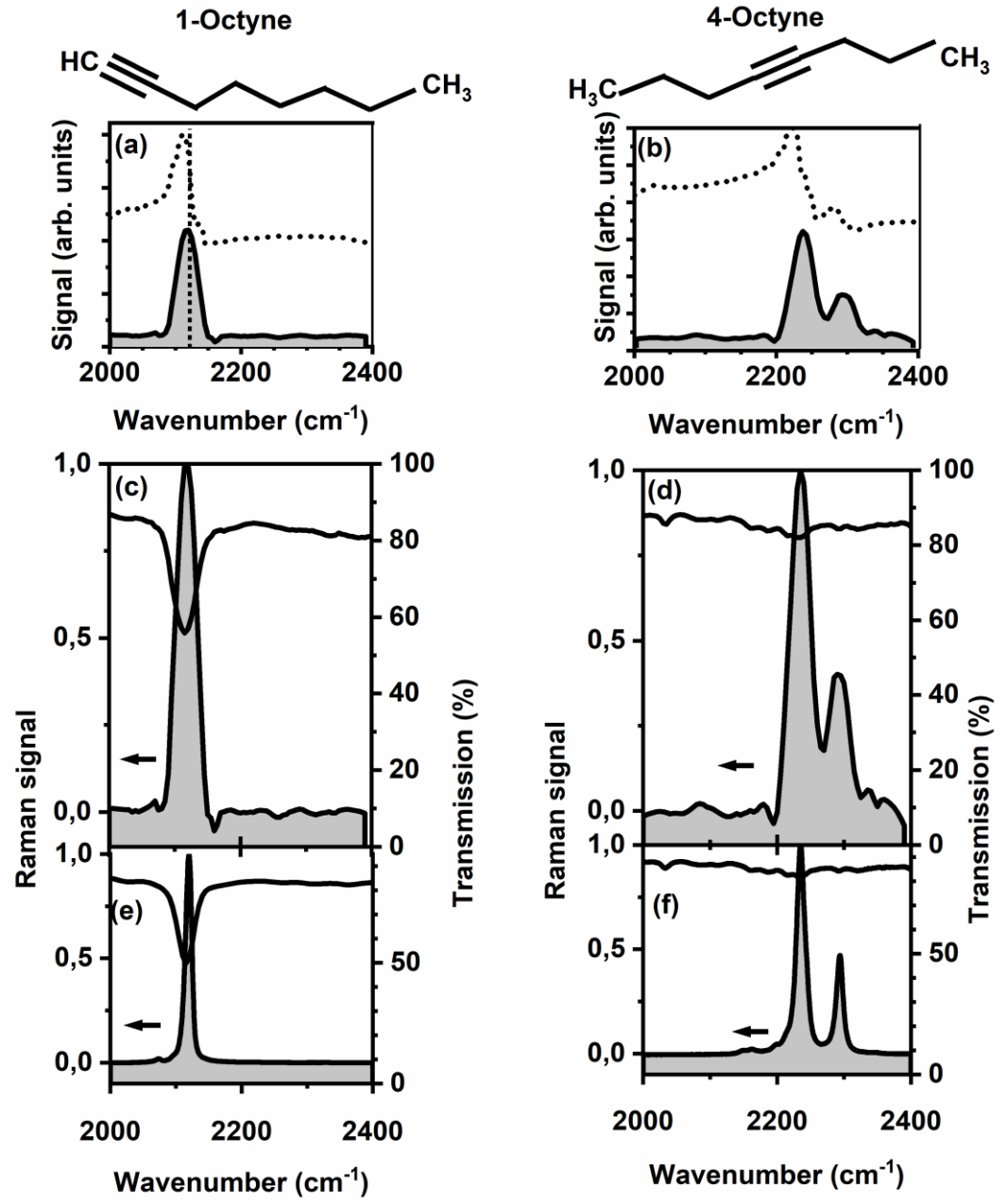

Figure V.3 Demonstration of the combined MIR and CARS spectroscopy on the C-C triple bond of 1-octyne (the left column) and 4-octyne (the right column) in solution. The CARS spectra of (a) 1-octyne and (b) 4-octyne (dotted line) are transformed into the linear Raman signal (black line) by MEM retrieval. (c & d) MIR spectra (solid black lines) and the MEM-retrieved Raman spectra (with grey backgrounds) for (c) 1-octyne and (d) 4-octyne. (e & f) Reference measurements are taken in a commercial Raman microscope and FTIR spectrometer for (e) 1-octyne and (f) 4-octyne. (a-d) A chirp of 9000 fs^2 and 7000 fs^2 is imprinted on the shaper in the single-beam setup for the MIR and CARS spectroscopy, respectively. Reproduced from [1], with the permission of AIP Publishing.

In CARS spectroscopy, vibrational modes are observed at 2120 cm^{-1} (a) and 2240 cm^{-1} (b) for 1-octyne and 4-octyne, respectively (Figure V.3). These modes are affected by a strong non-resonant background. Therefore, a MEM retrieval with error-phase fitting was performed to extract the Raman-like spectra [66, 122].

The linear Raman-like spectra are compared to the MIR spectra for 1-octyne (c) and 4-octyne (d), as shown in Figure V.3. Whereas the C-C triple bond is observed at the same frequency in both spectra for 1-octyne, the vibration mode of 4-octyne is only shown in the Raman-like spectrum. This mode is not observable in the MIR spectrum due to its MIR inactivity, which is caused by the inversion symmetry of the C-C triple bond in 4-octyne.

In order to verify these results, independent measurements are performed with a FTIR spectrometer (e) and a Raman microscope (f in Figure V.3). These measurements overlay well with the results of the combined MIR and CARS spectroscopy when the spectral resolution of the FTIR spectra is adjusted by the instrument response function of the new MIR light (see section IV.5 ii and section before).

4. Demonstration of combined CARS and MIR microscopy

4 i. CARS and MIR microscopy on polymers

The potential of combined CARS and MIR microscopy with a polyethylene (PE) film is shown in Figure V.4.

In order to identify the vibrational modes, spectra are recorded with both methods first. The CARS spectrum is taken with an imprinted amount of chirp of 7000 fs^2 and a probe delay of 100 fs after the end of the excitation (Figure V.4d). This spectrum shows the vibrational resonances without any background at 2850 cm^{-1} and 2920 cm^{-1}, originating from the symmetric and anti-symmetric CH_2 stretching modes, respectively [123]. The same vibrational modes are also observed in the MIR transmission spectrum, which is acquired with the same imprinted amount of chirp (Figure V.4d).

To investigate the sample microscopically using both methods, the frequency is tuned to the symmetric CH_2 stretching (2850 cm^{-1}) and the sample is spatially scanned (Figure V.4a&b). The CARS image (a) indicates the high intensity of the CARS signal inside the sample, and this also allows one to observe the structure of the PE film. As expected, the MIR image shows a low transmission inside the sample due to the high MIR absorption (Figure V.4b). In contrast to the CARS image, the obtained contrast in this image is much smaller due to the limitation in the spectral resolution, which is discussed in more detail below (see section 4 iii). It is important to note that the images are acquired by an amount of chirp (CARS: 5000 fs^2; MIR: 3000 fs^2), whose corresponding width matches the width of the vibrational resonance. Therefore, high signal levels in both methods are obtained.

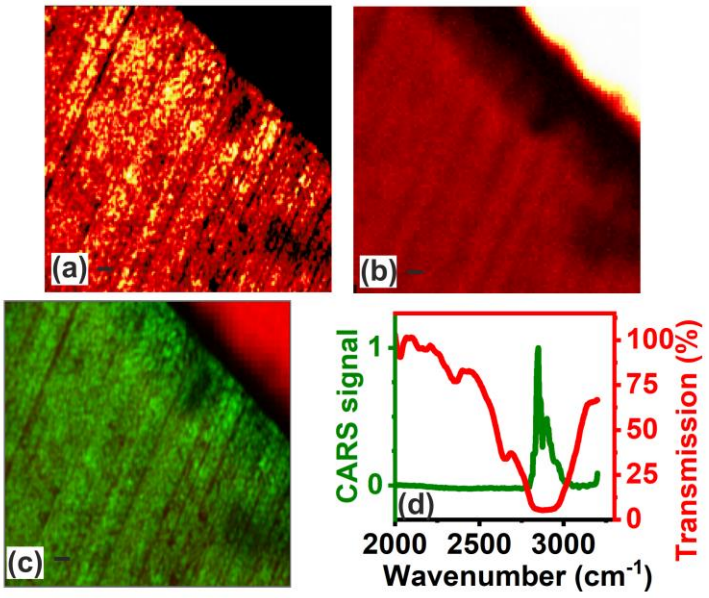

Figure V.4 First demonstration of the vibrational resonant CARS and MIR imaging. (a & b) The MIR transmission image (b, chirp: 3000 fs^2) and the CARS image (a, chirp: 5000 fs^2; probe delay: 100 fs after the end of excitation) are both resonant to the vibrational mode at 2850 cm^{-1}. They demonstrate reverse behaviours: high MIR transmission (bright) outside the polyethylene film and high intensity of anti-Stokes light inside the PE film. (c) In the combined image, the CARS intensity (green) and MIR transmission (red) are depicted. The black bar indicates 10 µm in all images. (d) The strong methylene band (CH_2-stretching) of the polyethylene (PE) is recorded in the MIR (red) and CARS (green) spectrum with an imprinted amount of chirp of 7000 fs^2. The probe pulse in CARS is delayed at 100 fs after the end of excitation. Reproduced from [1], with the permission of AIP Publishing.

The imaging potential is further investigated on 7 µm thick polystyrene beads (Figure V.5). This example demonstrates the good spatial accordance between the two images without a spatial shift.

Figure V.5 Image of 7 µm polystyrene beads detected at the vibrational resonance at 3060 cm^{-1} with an imprinted amount of chirp of 3000 fs^2 in MIR (b) and CARS (a) imaging. (c) The combined image with the CARS signal (green) and the MIR transmission (red) shows good agreement between the CARS and MIR images. The bar in the lower left represents 10 µm.

4 ii. Application of combined microscopy in life sciences

The combined MIR and CARS microscopy is also demonstrated on human skin tissue (in order to demonstrate how it would primarily be applied in life sciences). This sample is extracted from the dermis and fixed on CaF_2 substrates [1]. Its microspectroscopic investigation is done by acquiring the MIR transmission spectra as well as obtaining resonant MIR, resonant CARS, and second-harmonic images.

The MIR transmission spectrum is detected with an imprinted amount of chirp of 7000 fs^2 (Figure V.6a). The transmission has in the low-frequency range an absorption at 1655 cm^{-1} as well as two overlapping modes at 1540 cm^{-1} and 1450 cm^{-1}. Furthermore, absorption bands at 2920 cm^{-1} and around 3300 cm^{-1} are observable in the high-frequency range. In accordance with the literature [8, 124, 125], the spectrum is assigned to the protein collagen, which has a high abundance in the dermis in the formation of fibre bundles. The absorption bands are assigned to the Amide I band (1655 cm^{-1}), Amide II band (~1550 cm^{-1}), and the C-H bend vibration (1450 cm^{-1}) in the low-frequency range and to the CH_2 (2920 cm^{-1}) and N-H_2 (~3300 cm^{-1}) in the high-frequency range.

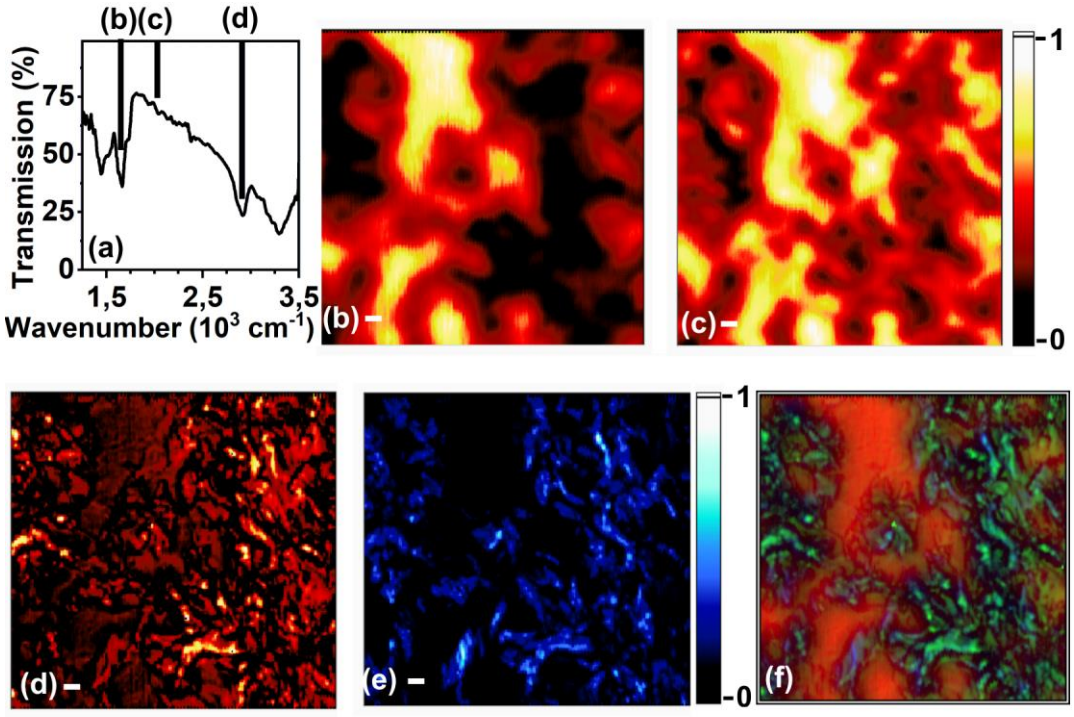

Figure V.6 Demonstration of combined MIR and CARS imaging on human skin tissue (190 µm x190 µm; 10 µm bar). (a) a MIR spectrum at a specific point of a human skin tissue sample is recorded. (b & c) The vibrational resonant MIR image at 1655 cm^{-1} (b) shows the collagen structure with more contrast than the non-resonant MIR transmission imaging at 2000 cm^{-1} (c). In MIR spectroscopy and imaging, an amount of chirp of 7000 fs^2 is imprinted. (d & e) CARS (d) and SHG (e) images are taken simultaneously at the resonance at 2920 cm^{-1} with an imprinted amount of chirp of 3000 fs^2. They show the collagen structure. (f) The combined image of vibrational resonant MIR (red), CARS (green), and SHG (blue) shows the correspondence of the different structures.

[1] prepared by the "Hautklinik des Universitätsklinikums Heidelberg"

To demonstrate vibrational resonant imaging, an image at 1655 cm^{-1} is taken (b) and compared with a non-resonant image, which is acquired at 2000 cm^{-1} (c in Figure V.6). The image taken at 2000 cm^{-1} has a contrast which is obtained without any vibrational signature by the scattering of the sample. In addition, the resonant image at 1655 cm^{-1} has a contrast from the absorption of Amide I and is directly sensitive to the collagen bundles.

Beside the MIR microspectroscopy, a CARS image with a narrowband excitation at 2920 cm^{-1} is taken simultaneously with a second-harmonic image at the same spot of the sample (Figure V.6 d & e). Both images indicate a fibrous structure, which can be directly assigned to collagen bundles. This structure is also shown in the superposition of the non-linear images and the resonant MIR image (Figure V.6f).

4 iii. Spatial resolution in MIR microscopy

In microscopy, the spatial resolution is limited by the wave characteristics of light and can be expressed by several criteria. One of them is the Rayleigh criterion, which considers the imaged Airy discs of two-point light sources on a screen. In order to resolve the two light sources in the image, the maximum of the first disc should be located at least at the minimum of the second one. The FWHM of a disc is used to express the criterion quantitatively and to indicate a linear dependence on the wavelength λ and the inverse numerical aperture NA [126]:

$$\mathrm{FWHM} = 0{,}51\,\frac{\lambda}{\mathrm{NA}}. \qquad \text{V.1}$$

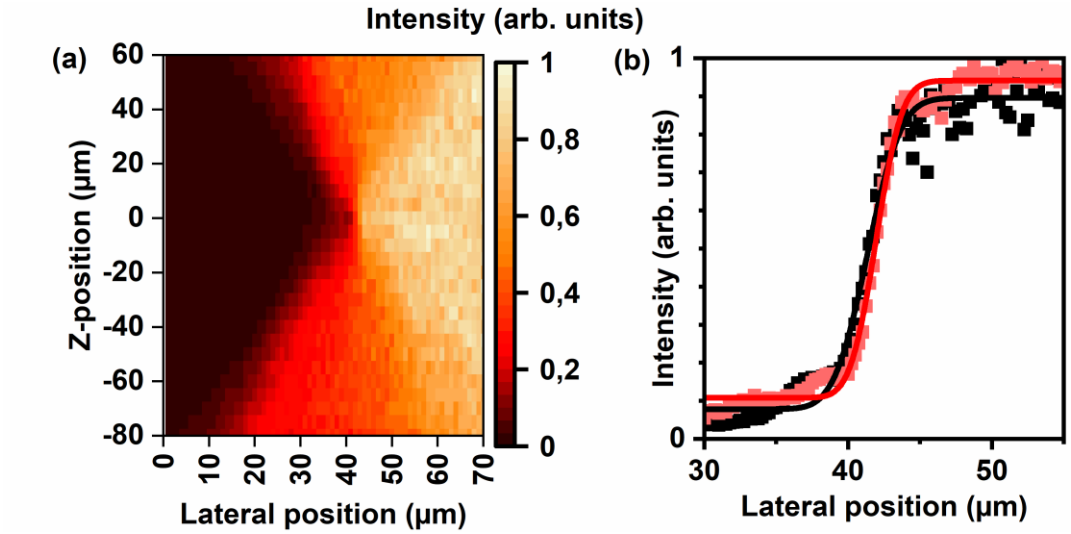

Figure V.7 Determination of the spatial resolution in MIR microscopy by scanning a razor edge. (a) The image of a razor edge in the X-Z plane is displayed (X: lateral direction, Z in beam direction and across the focus). It shows the focal plane (Z-position 0) by the sharpest profile of the edge. (b) For a broadband (black) and a narrowband (red; centre: 2850 cm^{-1} chirp: 7000 fs^2) MIR spectrum, the spatial width of the focused laser beam is retrieved by fitting an error-function (line) to the corresponding data (dots). The spectral widths with (4,3+/-0,3) µm (broadband) and (3,3+/-0,15) µm (narrowband) corresponds well with the theoretical resolution of 3,8 µm (broadband) and 2,7µm (narrowband).

Besides the theoretical consideration, the spatial resolution can be obtained experimentally by imaging a razor edge. The rectangular profile of this razor edge is flattened in the image by the finite instrument response function. In order to determine the response function, the image can be fitted by the convolution of the rectangular profile and the instrument response function, IRF, which is assumed to be Gaussian shaped (eq. V.2). The fit provides the information of the spot size (FWHM) in the focus;

$$IRF(x) \propto e^{-\sqrt{2\ln(2)}\left(\frac{x}{\mathrm{FWHM}}\right)^2}. \qquad \text{V.2}$$

In order to determine the spatial resolution of the new MIR light source, the profile of the razor edge is measured at different positions z along the beam propagation through the focus (Figure V.7a). A FWHM of $4{,}3 \pm 0{,}3\ \mu m$ and $3{,}3 \pm 0{,}2\ \mu m$ is obtained in the focus (z=0) for a MIR beam with a broadband and narrowband (2850 cm^{-1}) MIR spectrum, respectively.

These results can be compared to the theoretical limit of the spatial resolution by taking the objective (NA 0.65) into account (eq. V.2). An FWHM of 3,9 µm is obtained for the beam with the broadband spectrum centred at 5 µm and the beam with the narrowband spectrum at 3,5 µm has a theoretical resolution of 2,7 µm. The comparison of the experimental results with the theoretical limit indicates a small decrease of the spatial resolution, which is probably due to small misalignments in the setup.

The main limitation of MIR microscopy is the MIR wavelength itself, however, and its spatial resolution never reaches the limit that is possible in CARS microscopy. Defined by the wavelength at 800 nm, this theoretical limit is roughly five times smaller. Moreover, an additional factor $\frac{1}{\sqrt{N}}$ further increases the spatial resolution of the N^{th} order non-linear process (for more details see [127, 128]).

VI. Sum-frequency microspectroscopy based on flexible pulse shaping

1. Introduction

In nonlinear microscopy, the information about molecular vibrations is often obtained via coherent Raman spectroscopy using one or several laser pulses having a spectrum in the NIR or visible region (see chapter V) [63, 78, 114, 129, 130]. This information is also accessible by direct MIR excitations in SF spectroscopy. In contrast to CARS spectroscopy, SF spectroscopy is only sensitive to non-centrosymmetric systems and allows for the great possibility to investigate surfaces, interfaces, and crystalline structures [40, 41, 131, 132]. It provides high contrast of these structures by being blind to the dense bulk surrounding [133].

In addition, the SF process can also be applied to microscopy. This provides huge potential by combining the vibrational information with improved spatial resolution [42-45, 134-136]. In SF microscopy, the resolution is defined by the overlap of the NIR and MIR spot sizes. Since the spot sizes are proportional to the wavelengths due to Abbe's law, the NIR spot is smaller and defines the spatial resolution. This is a great advantage of SF microscopy over the already presented MIR microscopy (chapter V), whose spectral resolution is limited to several micrometres (see section V.4 iii).

The SF spectroscopy and microscopy are typically implemented either via a MIR-scanning or a multiplex method (Figure VI.1) [38, 137-141]. The MIR-scanning method

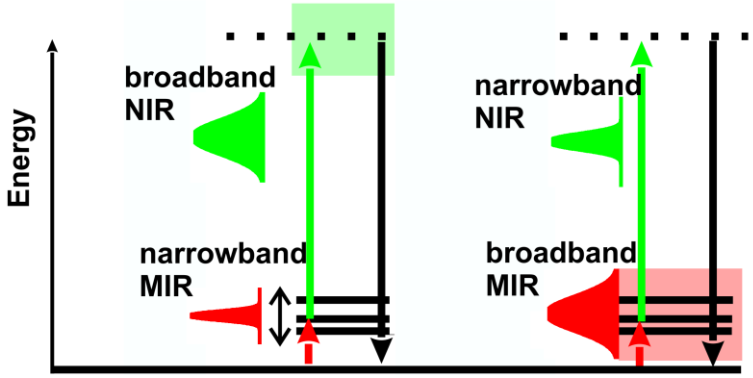

Figure VI.1 Scheme for MIR-scanning (left) and multiplex (right) SF spectroscopy. For the MIR-scanning method, a narrowband MIR spectrum (red) is scanned across the resonances and generates an excitation. This is probed by a broadband NIR spectrum (green). In the multiplex method, a broad MIR laser spectrum (red) excites all resonances at once, and the excitations are probed by a narrowband NIR spectrum (green).

acquires the SF light by exciting a single vibrational mode with a narrowband MIR pulse and probing the excitation non-resonantly with a NIR pulse. In order to acquire the whole SF spectrum, the spectrum of the MIR pulse must be tuned, as accomplished in optical-parametric-oscillators (OPO). By contrast, all vibrational resonances are excited in the multiplex method using one MIR pulse with a broad spectrum. The spectral resolution is obtained afterwards by generating the SF spectrum in the probe process via a NIR laser pulse, which has a narrowband spectrum. In order to assign the resonances to their MIR frequencies, the generated SF spectrum in the visible must be shifted by the NIR frequency into the MIR region.

Both experimental methods have specific advantages, which are complementary to each other. The MIR-scanning method uses either high MIR intensities or strong and spectrally broad NIR pulses to generate strong SF signals, which are detectable with short integration times and even allow microscopic imaging. These signal levels are usually not reached in the multiplex method. In contrast to the MIR-scanning method, the multiplex method has the potential to take the complete spectrum in one shot. Consequently, the implementation of both methods in one setup provides great advantages and is accomplished in a compact way through flexible pulse shaping. With nothing more than a switch of the imprinted phase, the application of both methods in a series is provided.

Furthermore, the shaping methods used have an additional difference. Whereas the MIR-scanning method is homodyne due to the detection without any background, the multiplex method is heterodyne since the signal is enhanced by the interference with a strong reference, which is called a local oscillator (LO). By implementing both methods, the potential phase sensitivity in the heterodyne multiplex method and the capability for detecting the undistorted SF signal in the homodyne MIR-scanning method is merged in one setup.

In this chapter, the shaper-based implementation of the homodyne MIR-scanning (chapter 2 i) and the heterodyne multiplex method (chapter 2 ii) is demonstrated. In the MIR-scanning method, the NIR laser pulses are shaped by spectral focusing [72] to generate narrowband MIR light. In order to achieve multiplex spectroscopy, the double-quadratic-spectral-interferometry [142] and the phase cycling [143] method are combined in the heterodyne multiplex method. After describing the experimental details (chapter 3), the two methods are demonstrated by detecting the vibrational modes of cholesterol and of crystalline cysteine (chapter 4). The results were already published in [2].

2. Pulse shaping approach for sum-frequency spectroscopy

The shaper-based implementation of SF spectroscopy consists of four main components: the NIR laser source, the DF generation stage, the pulse shaper, and the microscopic setup (Figure VI.2, 1st column):

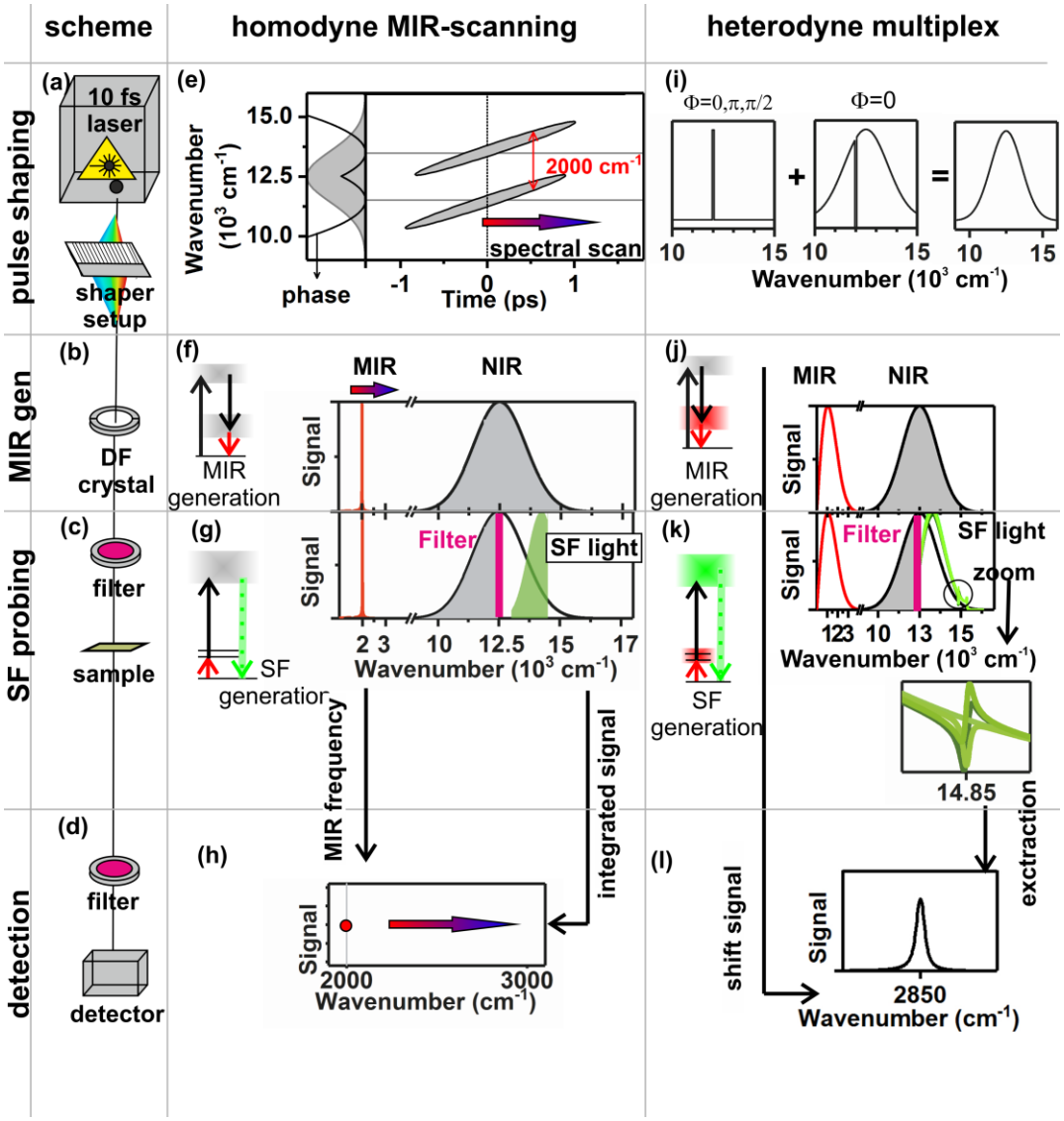

Figure VI.2 Scheme to demonstrate the homodyne MIR-scanning (the 2nd column) and the heterodyne multiplex method (the 3rd column) on the specific experimental parts (the 1st column). The setup consists of a laser and pulse shaper (a), DF stage (b), sample (c), and detection channel (d). The experimental parts are assigned row-wise to the two methods. (e) In the homodyne MIR-scanning method, spectral focusing shaped phases (solid line in left panel) with an instantaneous frequency difference (IFD) of 2000 cm^{-1} are imprinted on the laser pulses. These laser pulses are stretched in time (main panel). (f) The shaped NIR pulses (NIR spectrum grey area in the main panel) with an IFD at 2000 cm^{-1} generate MIR pulses that have a narrowband spectrum (red) in a DF process (the left sketch). (g) After passing through a long-pass filter, the spectrally cut NIR laser pulses and the MIR pulses generate SF light (green) in the sample. (h) This SF light is integrated on the detector and linked to the specific IFD and MIR frequency at 2000 cm^{-1}. To acquire the whole SF spectrum, the imprinted IFD and the MIR frequency are scanned (arrows in e, f, h). In the heterodyne multiplex method (the 3rd column), (i) the whole NIR spectrum (right) consists of a small gate with a variable phase of 0, π, -π/2 (left) and a broad part of the spectrum with an unchanged phase (middle). (j) The whole NIR spectrum (grey background) generates the broad MIR spectrum (red) in a DF process (left sketch). (k) Both NIR spectra generate SF light in the interaction with the MIR spectra, and the light varies in dependence on the imprinted phase on the gate (see zoom). (h) The SF spectrum is retrieved in accordance with eq. VI.3. Reprinted with permission from [2].

The sub10 fs NIR laser pulses are shaped by a programmable pulse shaper and used in a nonlinear crystal to generate MIR pulses. Afterwards, the NIR and MIR pulses are guided into the microscope to generate SF light inside the sample. The spectral resolution is solely accomplished by the pulse shaping via the two different methods, which are described below.

2 i. Homodyne MIR-scanning method

In the homodyne MIR-scanning method (Figure VI.2, 2nd column), MIR pulses with narrowband spectra are generated via the same two steps as in the MIR transmission spectroscopy (chapter IV). In the first step, NIR pulses are shaped with respect to spectral focusing (see Figure VI.2e) [72]. In accordance with spectral focusing, these pulses are stretched by two parabolic phase functions to provide elliptically-shaped pump and Stokes pulses in the frequency-time space. In the second step, pump and Stokes generate inside the DF crystal MIR pulses with a narrowband spectrum (see Figure VI.2f).

Afterwards, the generated MIR and shaped NIR pulses overlap perfectly in time and generate SF light inside the sample (see Figure VI.2g). After supressing these laser pulses with a short-pass filter, the SF light is detected. Although detection is made with a spectrometer, the signal is integrated and can be directly assigned to a specific vibrational mode due to the narrowband spectrum of the MIR pulses. To acquire the whole SF spectrum, this narrowband spectrum is tuned via an adjustment of the phase imprinted on the pulse shaper (for more details see chapter II.3 ii)

It should be noted that the SF light must be detected without any spectral overlap with the fundamental laser pulses. This is not provided a priori since SF light generated by MIR

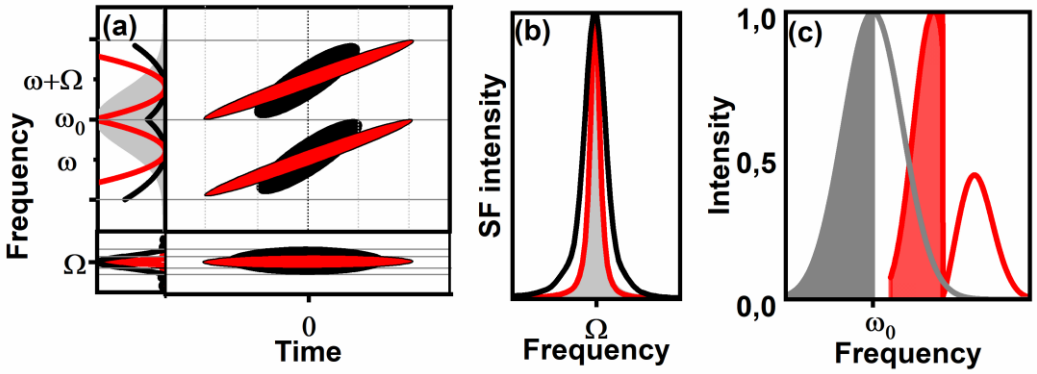

Figure VI.3 The figure has two independent parts considering different aspects in the homodyne MIR-scanning method. Figures (a & b) explain the spectral resolution and figure (c) demonstrates the spectral filtering of the NIR pulse. (a) Imprinting a high amount of chirp (red in the left upper panel) stretches the pulses strongly in time (red frequency-time ellipse in the main panel). These laser pulses generate MIR pulses with a narrowband spectrum (red line in the lower panel). (b) The narrowband MIR pulses resolve the vibrational resonance (grey background), whereas MIR pulses with broader spectra are not capable of resolving it (black). (c) MIR excitations in the SF process can be probed either by the Stokes (grey background) or pump (grey line without background). Simulations show that the SF intensity generated by the Stokes (red background) is larger than the SF intensity generated by the pump (red without background). Therefore, an 800 nm long-pass filter provides the Stokes for the SF process. (a & b) Adapted with permission from [2].

light at the low-frequency range (~1750 cm^{-1}) overlaps with the broad spectrum of the NIR pulses. Therefore, the spectral range of the pulses must be restricted either to the pump or Stokes. This choice is determined by the dynamic of the vibrational excitations, which show a slow decay after the MIR excitation. The Stokes, via its temporal increasing intensity, accounts for this dynamic and probes the MIR excitation at later times with high intensities. In contrast, the pump has its high intensity before the MIR excitation is completely built up and generate less SF signals. Consequently, the Stokes is chosen as the NIR probe pulse in the SF generation. This choice is corroborated by simulations which indicate an SF signal roughly two times higher after probing the MIR excitation by the Stokes than by the pump (Figure VI.3 c).

As already described in chapter II.3 ii, the flexible pulse shaping is also used for adjusting the spectral width of the MIR laser pulses by changing the amount of chirp imprinted via the pulse shaper (Figure VI.3a). The control of the shaper over the spectral resolution is shown in Figure VI.3b. The narrowband MIR pulses with a high amount of chirp can resolve the vibrational mode in the SF spectrum, whereas the one with a low amount of chirp cannot.

2 ii. Heterodyne multiplex method

In multiplex SF spectroscopy, the whole SF spectrum is acquired in general by probing broadband excited vibrational resonances with NIR pulses having a narrowband spectrum. Therefore, the width of these spectra directly determines the spectral resolution and should be narrower than 1 nm to resolve vibrational resonances with a typical width below 30 cm^{-1}. However, this bandwidth cannot be provided by typical pulsed laser sources, and additional spectral filtering is required. Usually this is done using Fabry-Perot filters or spatial filters in a 4 f setup [144, 145], although both have several drawbacks. Whereas a Fabry-Perot filter stretches the NIR pulses in a highly asymmetric manner over time, the spatial filtering in a 4f setup is complex as well as static [146].

The heterodyne multiplex method overcomes these problems by shaping NIR pulses via the phase of the double-quadrature-spectral-interferometry method [142] (Figure VI.2, 3rd column). This phase divides the whole spectrum of the NIR pulses into a broadband part with a constant phase and a narrowband part of the spectrum with a variable phase ϑ, which is called gate (see Figure VI.2i) [37, 143].

These shaped pulses are focused in the DF crystal and generate broadband MIR pulses (Figure VI.2j). Due to the small bandwidth of the gate, the MIR pulses are generated mainly by the broadband part of the NIR pulses and are not distorted by the changes of the gate-phase ϑ.

Afterwards, the combined NIR and MIR pulses generate SF light inside the sample, which is detected spectrally resolved. As depicted in the zoom in Figure VI.2k, the acquired SF spectra show a variation in dependence on the gate phase ϑ due to the interference between the SF light I_{LO} and I_{sig}, which are generated by the broadband part of the NIR spectrum and the gate, respectively. This variation can be exploited to retrieve the spectral shape of $I_{sig}(\omega)$, which depicts the vibrational mode of the sample with spectral resolution.

In order to derive the formalism unveiling $I_{sig}(\omega)$, the varied SF spectra S are divided into a constant part I_{homo} and a phase-sensitive term I_{het}. I_{homo} depends only on the amplitude of the SF light I_{LO} and I_{sig}. The phase-sensitive term I_{het} is assigned to the interference of the generated SF lights. Therefore, in addition to the amplitudes of the SF light, it also depends on the relative phase of the SF light's electric fields. This phase consists of the phase ϑ imprinted by the shaper and an unknown phase φ, which originates from the sample itself (eq. VI.1):

$$\begin{aligned} S &= I_{homo} + I_{het} \\ &= \left(I_{LO} + I_{sig}\right) + 2\sqrt{I_{LO} I_{sig}}\cos(\varphi + \vartheta). \end{aligned} \tag{VI.1}$$

In order to reconstruct $I_{sig}(\omega)$, three measurements, $S(\vartheta = 0)$, $S(\vartheta = \pi)$, and $S(\vartheta = -\pi/2)$, with different gate phases are considered. The interferences I_{het} are varied for the three measurements: $I_{het}(\vartheta = 0) \propto \cos(\varphi)$, $I_{het}(\vartheta = \pi) \propto -\cos(\varphi)$, and $I_{het}(\vartheta = -\pi/2) \propto sin(\varphi)$. The unknown parameters $I_{LO}(\omega)$, $I_{sig}(\omega)$, and $\varphi(\omega)$ are determined by the equation system of the three measurements $S(\vartheta = 0)$, $S(\vartheta = \pi)$, and $S(\vartheta = -\pi/2)$:

$$\tan(\varphi) = \frac{1}{I_{het}}\left\{S\left(\vartheta = -\frac{\pi}{2}\right) - I_{homo}\right\}, \tag{VI.2}$$

$$I_{sig} = \frac{I_{homo}}{2} - \frac{1}{2}\sqrt{I_{homo}^2 - \left(\frac{I_{het}}{\cos(\varphi)}\right)^2}, \tag{VI.3}$$

with the auxiliary equations

$$I_{homo} = \left(I_{LO} + I_{sig}\right) = \frac{1}{2}\{S(\vartheta = 0) + S(\vartheta = \pi)\}, \tag{VI.4}$$

$$I_{het} = 2\sqrt{I_{LO} I_{sig}}\cos(\varphi) = \frac{1}{2}\{S(\vartheta = 0) - S(\vartheta = \pi)\}. \tag{VI.5}$$

The final step shifts the retrieved spectrum of $I_{sig}(\omega)$ from the visible into the MIR region and assigns it to the vibrational modes by subtracting the frequency of the gate from the frequency of $I_{sig}(\omega)$.

In contrast to $I_{sig}(\omega)$, $I_{LO}(\omega)$ is generated by the broadband part of the NIR spectrum and consists mainly of the generated non-resonant background (see section II.2 ii). Since this background is much stronger than $I_{sig}(\omega)$, it acts as an LO and enhances the low signals $I_{sig}(\omega)$ above the noise threshold [147]. Furthermore, it provides the phase sensitivity in the heterodyne detection, which is important for the reconstruction of $I_{sig}(\omega)$.

This heterodyne detection on the bases of the double-quadratic-spectral-interferometry method has three main advantages [142]. Firstly, the SF spectrum $I_{sig}(\omega)$ is reconstructed

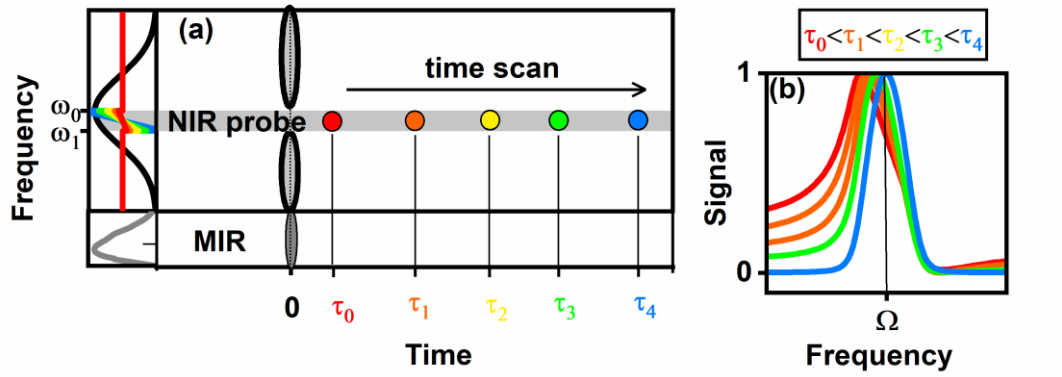

Figure VI.4 Concept and simulation of the extension tailored-probing in the heterodyne multiplex method: (a) Using linear phases imprinted on the gate, the NIR probe pulses are delayed to do not overlap with the MIR pulses. (b) The strong interference between the non-resonant background and the vibrational resonances decreases by increasing the probe delay (from red to blue). Due to better illustration, the width of the gate in (a) is five- times greater. Adapted with permission from [2].

by its intensity, which hinders the increasing of the noise by taking the square-root in an analysis of its electric field. Secondly, the two-value problem of the trigonometric functions is overcome by accounting for the same periodicity of π in the phase ($\tan(\varphi)$) and the intensity retrieval ($\cos(\varphi)$). Lastly, the SF pulses of the signal and the LO overlap in time for all gate widths. Therefore, the highest spectral resolution can be acquired simultaneously with the highest signal-to-noise ratio. This is in contrast to the popular SF detection scheme 'spectral interferometry', which provides spectral resolution by the interference of the signal with a time-delayed second laser pulse [148]. In this case, high spectral resolution is only possible with large time delays, which simultaneously reduces the temporal overlap of the two pulses and the signal-to-noise ratio.

It is important to note that instead of using the specific SF spectra $S(\vartheta = 0), S(\vartheta = \pi), S(\vartheta = -\pi/2)$ every configuration of measurements with three different phases can be used for the spectral retrieval. However, phase imprinted variations of the SF spectra are maximized by combinations out of $\vartheta = 0, \pi, +\pi/2, -\pi/2$. Especially the configuration $0, \pi, +\pi/2$ can be simply used by adding a sign change in the argument of equation VI.2.

The imprinted phases in the heterodyne multiplex method vary only in a small range. Therefore, the interacting laser pulses are much shorter and generate a large non-resonant background, which distorts the line shape of the detected vibrational modes (see section II.2 ii). A reduction can be accomplished utilising the fast decay of the non-resonant background and the long lifetimes of the resonant contributions. Therefore, this background can be supressed by delaying the probe pulse behind the end of the MIR excitation. This is solely accomplished by an additional phase on the gate in the extension tailored-probing. Beside the variable phase ($\vartheta = 0, \pi, -\pi/2$), a linear phase is imprinted whose slope determines the time delay (Figure VI.4).

However, the gate with its width between 10 and 30 cm^{-1} cannot be delayed by its temporal width in the ps-range. A temporal confinement of the gate is only possible by broadening its spectrum, which on its downside decreases the spectral resolution. In order to solve this contradiction, the narrow gate with its variable phase ($\vartheta = 0, \pi, -\pi/2$) is

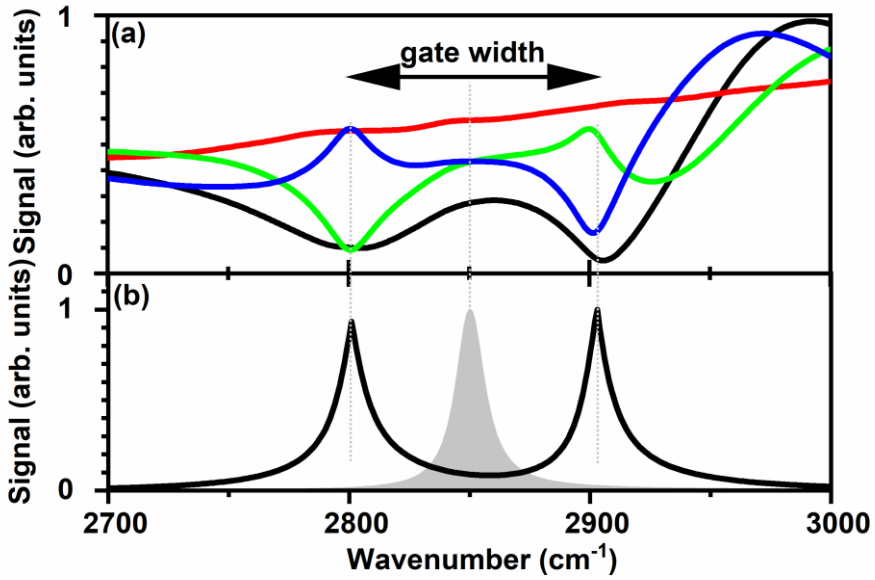

Figure VI.5 Simulated failure of the heterodyne multiplex method. A suppression of the non-resonant background in combination with a broad gate width makes this method unusable. (a) In this case, the phase jump at the edge of the gate dominates the SF spectra (phase 0 [red], π [black], π/2 [green] and -π/2 [blue]). (b) The retrieved SF spectrum (black) also fails to show the expected vibrational mode (grey background).

enclosed in a broader gate, which contributes with the linear phase. While the narrowband gate still provides a high spectral resolution, the broader gate is short in time and accomplishes the time delay.

It is important to note that tailoring the probe pulse only reduces the non-resonant background rather than supress it completely. This is important since this background is the main contribution of the LO. As demonstrated in simulations (Figure VI.5), detection in the heterodyne multiplex method without any LO allows no retrieval of the SF spectrum.

In order to preserve the LO, it must be generated either by a small phase gate in a larger time gate or by a smaller time delay. The latter option yields an interference of the signal $I_{sig}(\omega)$ and the non-resonant background $I_{LO}(\omega)$, which is generated by the broadband NIR pulse at time zero and is not completely decayed. With the first option, the phase gate is small, and the LO can also be generated by the resonant contribution.

3. Experimental details

Both methods are demonstrated by a setup (Figure VI.6) which is based on the already used shaper-based setup (chapter IV). A Ti:Sa oscillator provides sub 10 fs laser pulses, which are shaped by a liquid crystal pulse shaper and generate MIR pulses in a 1 mm thick $LiIO_3$ crystal with a spectrum ranging from 1750 up to 3500 cm^{-1}.

The NIR and MIR pulses cannot be used for SF spectroscopy in a single-beam setup since the NIR pulses cannot be modified by any substrate without the MIR pulses

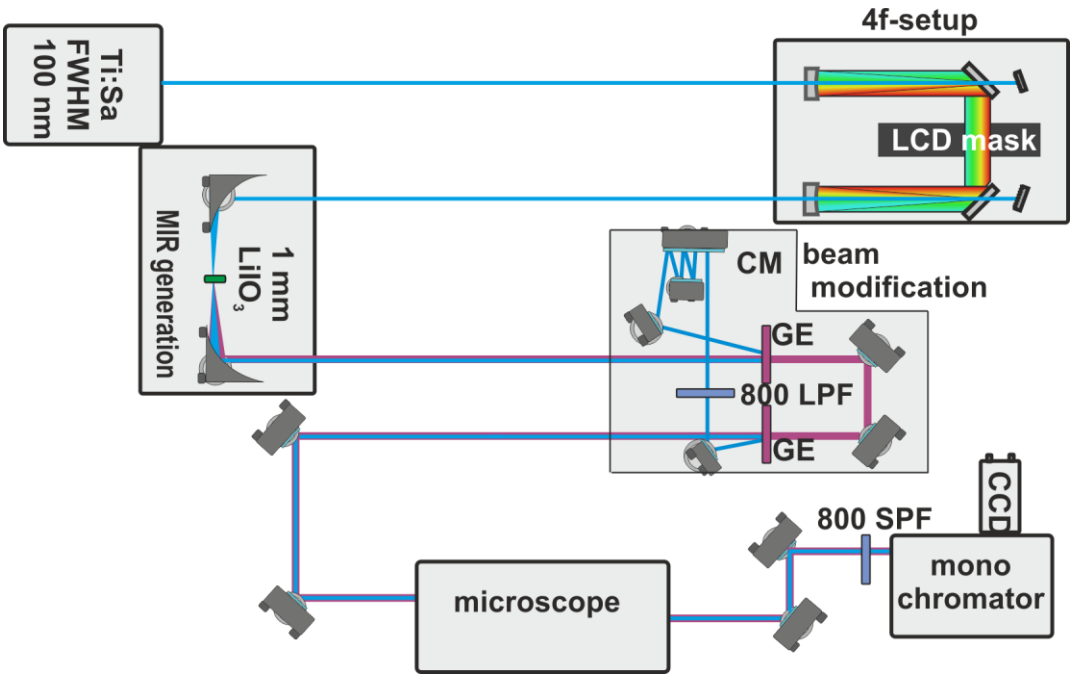

Figure VI.6 Experimental details of SF spectroscopy. The sub 10 fs laser pulses made by the Ti:Sa oscillator are guided into the 4 f setup for arbitrary pulse shaping. Afterwards, these shaped laser pulses are guided to the MIR generation setup consisting of parabolic mirrors that focuses the pulses (f = 10 cm) inside the 1 mm thick $LiIO_3$ crystal and collimates (f= 5 cm) them. The MIR and NIR laser pulses are separated by a germanium (GE) beam splitter. The reflected NIR pulses are guided to the 800 nm long-pass filter (LPF) and to chirped mirrors (CM). The MIR pulses are transmitted and recollimated with the NIR laser pulses by a second GE beam splitter. The collimated MIR and NIR pulses generate SF light in the sample inside the microscopy. After passing through a 785 nm short-pass filter to suppress the fundamental laser pulses, the SF light is dispersed in a Frank-Czerny spectrometer and detected on an electron-multiplying CCD camera. Adapted with permission from [2].

deteriorating (see for more details section V.2). Therefore, these NIR and MIR pulses are separated on a germanium beam splitter. The MIR pulses transmit the beam splitter and pass through two CaF_2 lenses, which provide temporal and spatial confinement. The NIR pulses are reflected on this beam splitter and their spectrum is cut afterwards by an 800 nm sharp-edge long-pass filter. However, this filter stretches these pulses in time. They can be compressed by a specific number of reflections on chirped mirrors (1000 fs^2) to the pulse length, which they have before the beam splitter. In order to determine the number of reflections, different amounts of chirp are imprinted on the pulse shaper, and the interferometric autocorrelation is measured before the chirped mirrors.

The NIR and MIR pulses are combined on a second germanium beam splitter and focused into the sample using a 74X Schwarzschild objective (BOS 5007, NA 0.65). After the SF generation, all laser pulses are collimated using a 40X reflective objective (Thorlabs LMM-40x-P01), and they are guided to the detection channel. The SF light is detected spectrally resolved (Acton SP300i) by an electron-multiplying CCD camera (Andor Newton DU 970) after passing a short-pass filter (785 nm) that supresses the fundamental laser pulses.

The potential of both methods is shown on cholesterol and cysteine. Cholesterol is prepared as a crystalline sample on an objective. This is accomplished by dissolving cholesterol in chloroform that evaporates in the crystallisation process [43]. The cysteine dissolved in water crystallises on an objective slide after the water has been evaporated.

4. Experimental application

4 i. Homodyne MIR-scanning method for sum-frequency microscopy

The potential of the homodyne MIR-scanning method for SF microspectroscopy is demonstrated by investigating the strong methylene band of crystalline cholesterol. These spectra are taken with different spectral resolution by varying the imprinted amount of chirp (Figure VI.7a). The obtained spectra show a broad or narrow methylene band by imprinting a small or high amount of chirp, respectively.

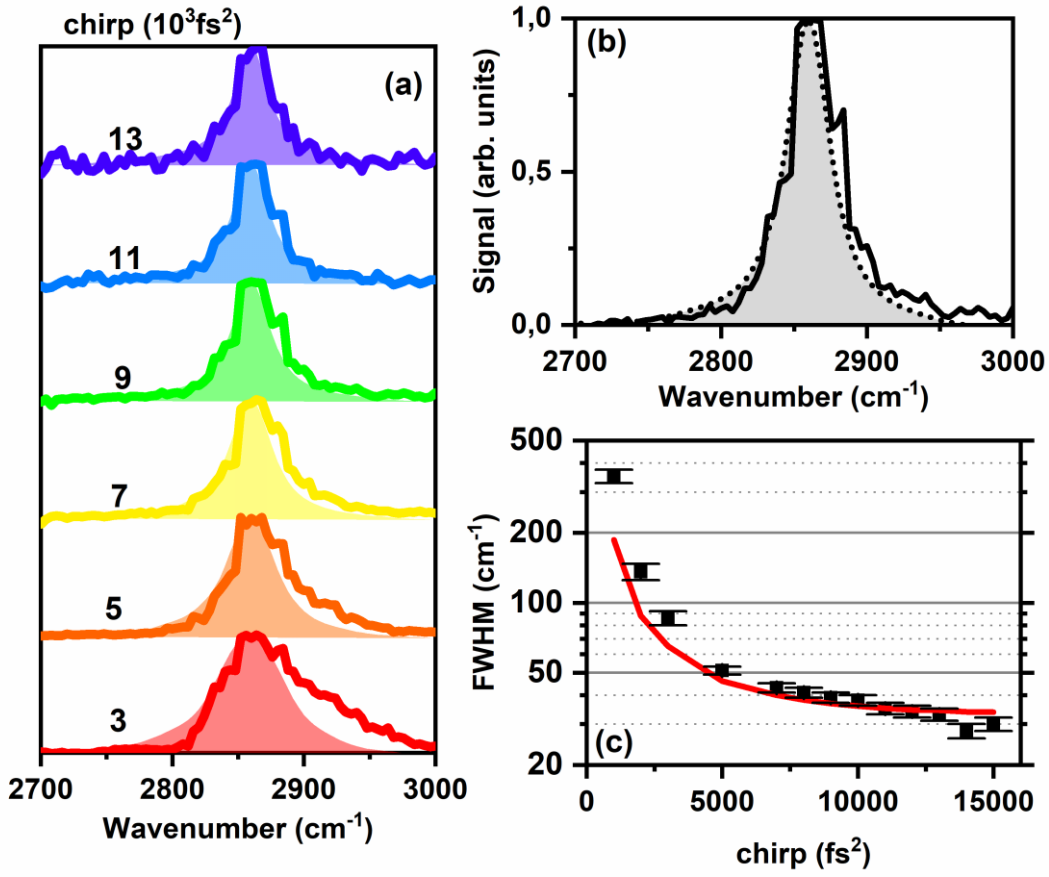

Figure VI.7 Demonstration of the homodyne MIR-scanning method by detecting the methylene group of cholesterol. (a) The measured (solid line) and simulated (background) SF spectra show an increase in spectral resolution with an increasing amount of chirp. All simulations agree with their measurement. (b) This is shown in particular for an imprinted chirp of 9000 fs^2. (c) The spectral width of the methylene band decreases by an increasing chirp (measurement: dots, simulation red line). Adapted with permission from [2].

The spectral resolution is analysed quantitatively by investigating the spectral width of this band in dependence on the imprinted amount of chirp (Figure VI.7c). The obtained widths (FWHM) show a decrease from above 100 cm^{-1} by chirps to below 3000 fs^2 down to 30 cm^{-1} at chirps above 13000 fs^2.

The homodyne MIR-scanning method is further corroborated by modelling the experimental results with simulations. The simulations consider the experimental NIR spectrum, the pulse shaping in a 4f setup by the pixelated pulse shaper, as well as the MIR and SF generation. Using an evolutionary algorithm, a FWHM of 18 cm^{-1} is obtained for the molecular response function of the methylene band by fitting these results in combination with the results of the heterodyne multiplex method. The fittings (the backgrounds in Figure VI.7a) correspond well with all measurements (the solid lines in Figure VI.7a).

It is important to note that the fitted linewidth of the molecular response function (18 cm^{-1}) is larger than the typical linewidths of vibrational modes in the susceptibility 2nd order (~8-12 cm^{-1}) [149, 150]. This is caused by several line-broadening effects, which cannot be resolved in SF microspectroscopy. Firstly, the sample has an unordered crystalline structure, which provides a distribution of different phase matching angles in SF microscopy. With the large aperture angle of the microscopic objective, SF light with respect to all phase matching angles is generated. Consequently, a vibrational mode detected in the SF spectroscopy is the summation of individual vibrational line shapes. Secondly, the used SF microscopy is not polarisation sensitive. Therefore, the different spectral shapes of a vibrational mode observable in polarisation-sensitive SF spectroscopy cannot be resolved. The impact of the different line-broadening effects can be further analysed either in polarisation-sensitive or in time-resolved SF spectroscopy. In the latter, the free induction decay of the MIR excitation is detected by driving an excitation at time 0 with the MIR pulse and scanning the decay of this excitation with the NIR probe pulse in time. The obtained decay rates of the vibrational modes are the temporal representation of the vibrational line shapes and indicate the hidden structure of the detected SF spectrum [151, 152].

The potential of the homodyne MIR-scanning method for resonant imaging is demonstrated on crystalline cysteine. Cysteine is an amino acid, which is, for example, part of proteins inside the muscle tissue. This amino acid can be identified by its thiol group (-SH sulphur hydrogen) around 2550 cm^{-1}, as shown in the detected SF spectrum (Figure VI.8d; chirp 3000 fs^2). In addition, the SF spectrum shows a distortion of the vibrational line shape and a small signal outside the resonance due to the presence of a non-resonant background. However, this background is much smaller than the resonant contribution generated using highly stretched laser pulses. Therefore, vibrational resonant imaging has a higher contrast compared to images obtained off-resonantly.

A resonant image with an integration time of 100 ms is taken by tuning the MIR spectrum to the vibrational resonance (chirp 3000 fs^2). It shows a crystalline structure of the cysteine (Figure VI.8a) and agrees well with an image taken by second-harmonic light (Figure VI.8b) due to the quadratic dependence on the 2nd order susceptibility of both processes.

The agreement between both images is only obtained after a correction of the second-harmonic image. This correction is needed due to the slight tilt of the sample in the

microscope. In this case, the sample moves out of focus and the beam spot size changes slightly across the sample. This change must be considered due to the different scaling of both processes on the NIR intensity and on the beam spot size. While the SF image linearly depends on the inverse NIR-beam spot size, the second-harmonic image quadratically depends on it. This different scaling is consequently corrected.

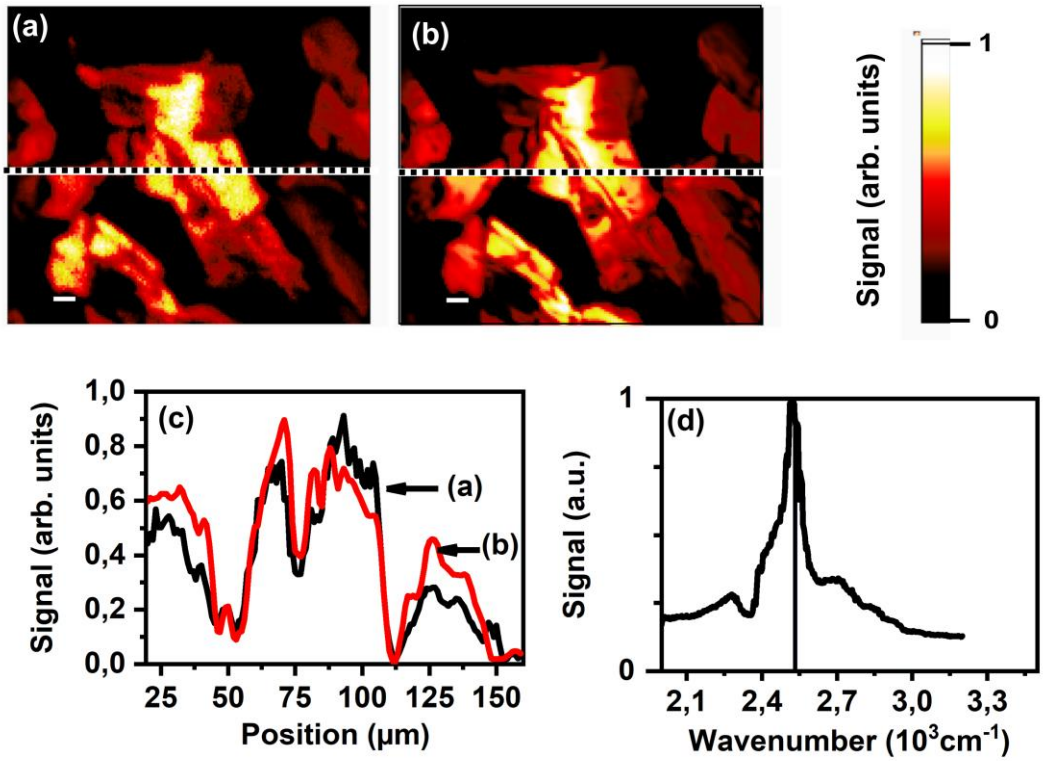

Figure VI.8 Demonstration of the SF imaging on cysteine microcrystals. (a) A resonant SF image is recorded on the vibrational mode of the thiol group (the white bar represents 10 µm). (b) The image obtained by second-harmonic light shows the same crystalline structure. (c) The lineouts also show the agreement of SF (black) and second harmonic (red) signals (position marked in [a] and [b]). (d) SF spectrum of cysteine depicts the well-known thiol band. (a-c) Adapted with permission from [2].

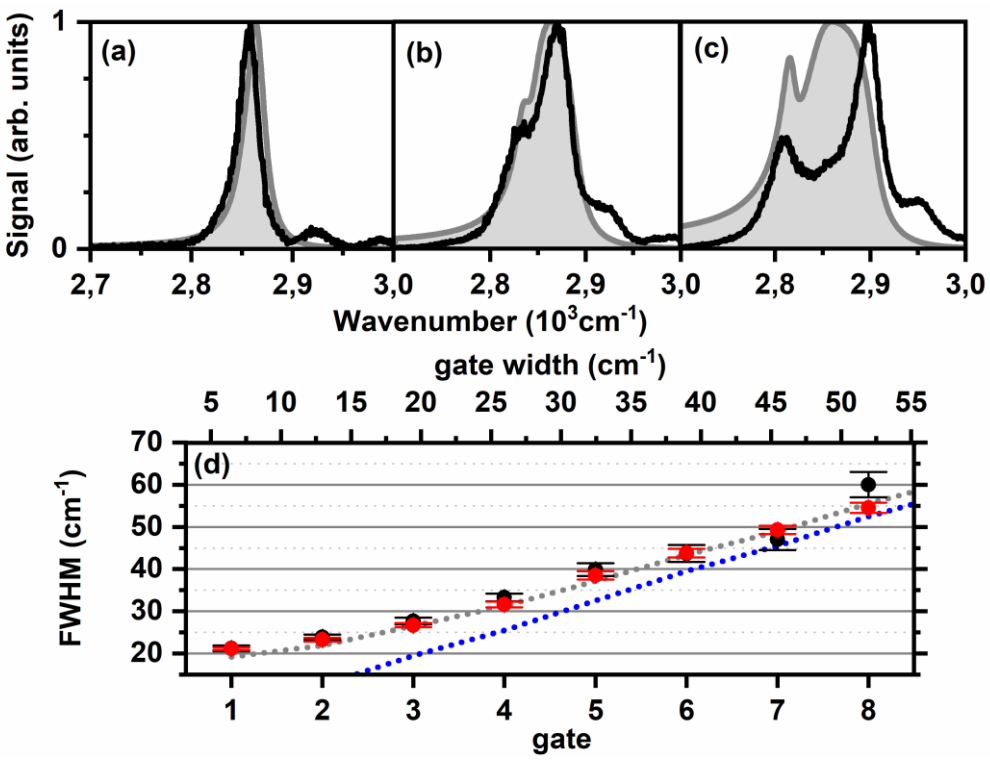

Figure VI.9 Demonstration of the heterodyne multiplex method on the cholesterol methylene band. (a & b) The measured (black line) and simulated (grey background) SF spectrum are detected by a gate width of 2 (a) and 8 pixels (b). (c) The heterodyne multiplex method breaks down when using gate widths that are too large, as shown on the SF spectrum acquired with a gate width of 13 pixels. (d) The spectral widths (FWHM) of the measured (black) and simulated (red) methylene band increase by increasing the gate width. They correspond well with the squared sum (grey dotted line) of the molecular response function and the instrument response function. Latter one is determined by the spectral width of the gate on the pulse shaper (blue dotted line). Adapted with permission from [2].

---

4 ii. Heterodyne multiplex method for sum-frequency spectroscopy

The heterodyne multiplex method is demonstrated on cholesterol microcrystals (Figure VI.9). The SF spectra (a & b) show the known methylene band at 2855 cm^{-1} and, in addition, vibrational resonances at higher wavenumbers, which have been observed earlier by Hanninen *et al.* [43].

However, these resonances are not present in the spectra acquired in the homodyne MIR-scanning method. In order to understand the deviation between the SF spectra, the temporal differences in the excitation and probing of the two methods must be considered. In contrast to the excitation by long laser pulses in the homodyne MIR-scanning method, the excitation and probe process are much shorter in the heterodyne multiplex method. These time scales affect the SF generation on different vibrational modes since the dynamic of these vibrational modes must be accounted for. Therefore, the vibrational modes with higher

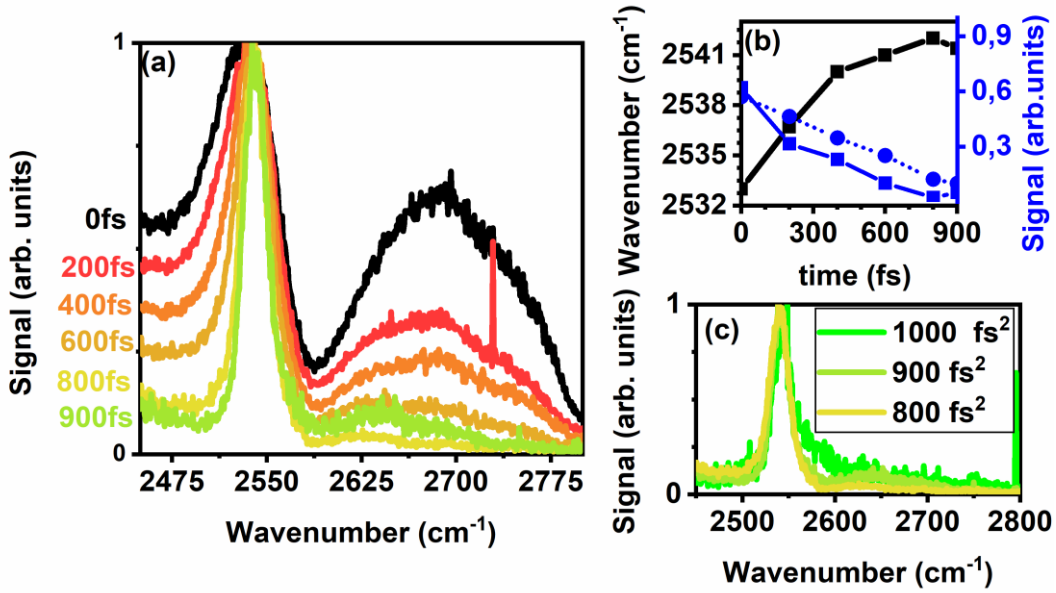

Figure VI.10 Experimental demonstration of the extension tailored-probing in the heterodyne multiplex method on crystalline cysteine. (a) The detected SF spectra show a decrease of the non-resonant background from above 0,6 down to 0,1 when the time delay is increased (time gate: 50 cm^{-1}, phase gate: 32 cm^{-1}). In addition, the distortion of the vibrational mode is also reduced. (b) The shift of the centre of the detected mode is depicted in black in accordance with the left y-axis. The signal intensity outside the resonance is shown on the right y-axis for 2475 cm^{-1} (blue dotted line) and 2650 cm^{-1} (solid line). (c) A revival of the non-resonant background at probe delays of 900 fs^2 and 1000 fs^2 appears due to the sinc-shape of the gate in frequency space. (a) Adapted with permission from [2].

decay rates are detected with higher intensities in the heterodyne multiplex method than in the homodyne MIR-scanning method.

The observation of the strong methylene band, which corresponds well with the homodyne MIR-scanning method, is also used to determine the spectral resolution. As shown in Figure VI.9d, the spectral width of this band (FWHM) increases depending on the gate width from below 25 cm^{-1} (1 pixel) up to 60 cm^{-1} (8 pixels). This is further corroborated by simulations, which are simultaneously performed with the ones for the homodyne MIR-scanning method (see more details in section 4 i).

The spectral resolution can be further analysed by taking the measured vibrational mode as a convolution of the instrument and molecular response function. The widths of the instrument and molecular response function are modelled by the width of the gate (blue line in Figure VI.9d) and the spectral width of the methylene band, respectively. The latter width (18 cm^{-1}) is taken from the simultaneous fit of both SF methods (see section 4 i). Assuming Gaussian-shaped response functions, the spectral width of the SF-detected vibrational mode is calculated by the squared sum of the individual FWHMs. The result of this calculation corresponds well with the measurement, as shown in Figure VI.9d.

The deterioration of the heterodyne multiplex method is also demonstrated on the methylene band of cholesterol as shown on the SF spectrum acquired by a large gate width (13 pixels). This spectrum indicates the edge of the gate rather than resolving the methylene

band (see Figure VI.9c). This is in accordance with the previous theoretical considerations (see section 2 ii).

The potential for supressing the non-resonant background by a delayed probe pulse is experimentally demonstrated on crystalline cysteine. This molecule is a perfect example due to the appearance of a strong non-resonant background in SF spectra that is detected without a probe delay (black in Figure VI.10). By delaying the probe (800 fs), this background is reduced by more than a factor of 20. Furthermore, the distortion of the detected vibrational mode disappears, and the centre of the resonance is shifted from 2533 cm^{-1} (0 fs) up to 2541 cm^{-1} (800fs) (see also Figure VI.10b).

The SF spectra acquired at a large time delay (900 fs and 1000 fs) show a small revival of this distortion and of the off-resonant amplitude (Figure VI.10c). This distortion can be traced back to the rectangular shape of the probe spectrum, which shows a sinc-function with known sidelobes as temporal distribution. For large probe delays, one of these sidelobes matches the MIR excitation at time 0 and generates a non-resonant background. In contrast to the non-resonant background generated by the LO (broadband part of the NIR spectrum), this one varies by the phase of the gate and therefore contributes to the retrieved SF spectrum. This explanation is corroborated by the good agreement between the time delay yielding experimentally the smallest non-resonant background (800 fs) and the position of the minimum (820 fs) calculated for this gate (width: 50 cm^{-1}).

4 iii. Homodyne MIR-scanning method for MIR spectroscopy

MIR transmission spectroscopy is a powerful method for obtaining information about molecular vibrations by detecting their spectra directly in the MIR. However, the used spectrometers have much lower sensitivities than detectors in the visible, which can even detect single photons [153]. The up-conversion spectroscopy method exploits these detectors for the acquisition of MIR transmission spectra by shifting MIR spectra via an SF process in the visible [154-156].

The SF spectroscopy setup presented here permits up-conversion spectroscopy by focusing the NIR and MIR pulses into a 100 µm thin $LiIO_3$ crystal outside the microscope and detecting the generated SF light with a visible spectrometer (detailed setup in Figure VI.11a). The broad and constant conversion efficiency of this thin crystal provides SF light, which solely depends on the MIR intensity. In order to obtain the whole SF spectrum with spectral resolution, the homodyne MIR-scanning method is applied to scan the MIR spectra and link the detected SF light to a specific MIR frequency.

In a first application, an SF spectrum without any sample is obtained (Figure VI.11b). This spectrum ranges from 1750 cm^{-1} above 3000 cm^{-1} and allows access to vibrational modes over a broad spectral range in SF spectroscopy.

Furthermore, MIR transmission spectra of a polystyrene film are taken for different amounts of chirp (Figure VI.11c). These spectra agree well with the FTIR reference measurement as concerns the spectral resolution. The spectral resolution is analysed by fitting the convolution of molecular response and the instrument response function to the detected transmission spectra, as was already done for the spectra detected directly in the MIR (see chapter IV). The obtained spectral width of the narrowband MIR spectra

decreases from high spectral widths at low amounts of chirp towards a spectral width around 25 cm^{-1} at high amounts of chirp (Figure VI.11d). These widths are in accordance with the results acquired previously by direct MIR detection (see Figure IV.9)

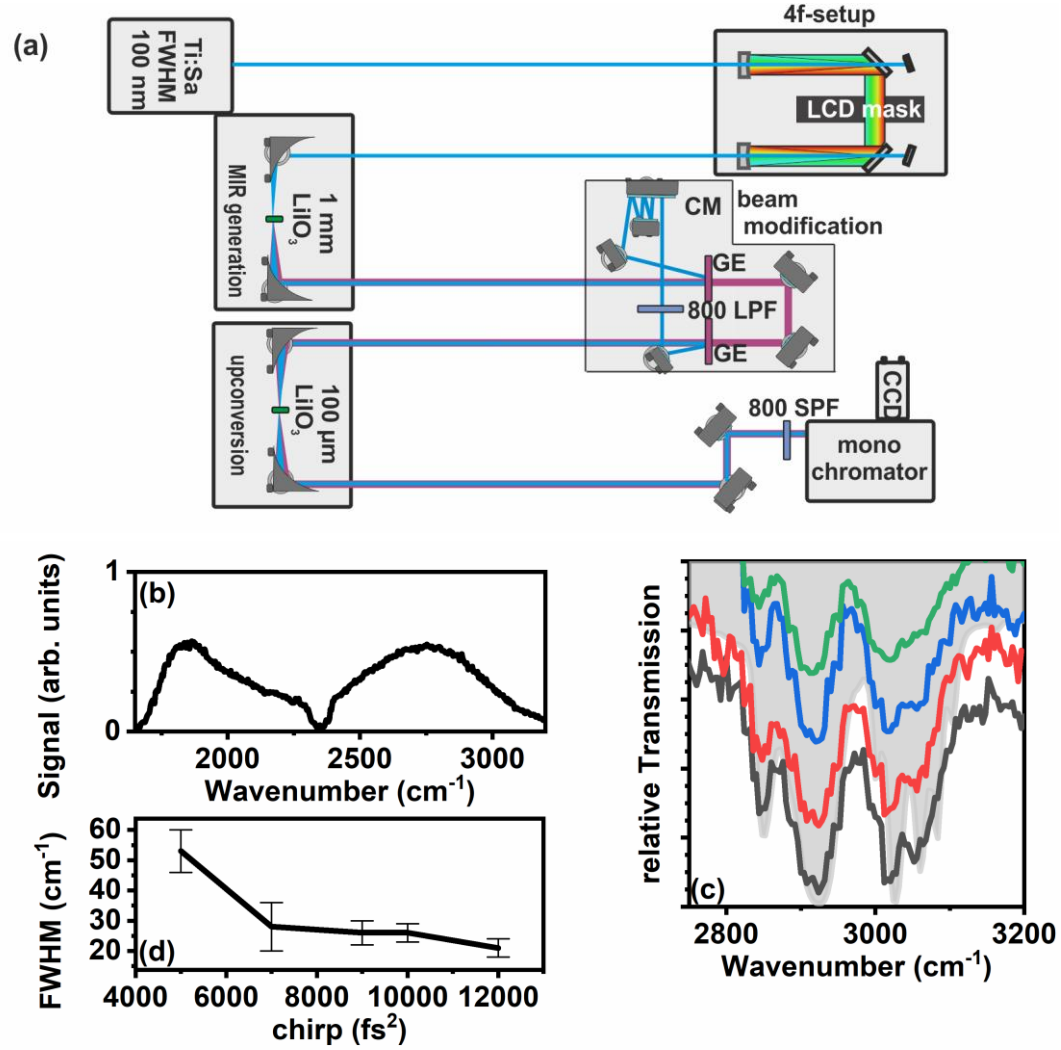

Figure VI.11 Homodyne MIR-scanning method for up-conversion MIR spectroscopy. (a) The setup for up-conversion spectroscopy is slightly different to the setup for SF microscopy (Figure VI.6). It consists of a 100 µm thick $LiIO_3$ crystal between two parabolic mirrors instead of a microscope (focusing: f = 10 cm; collimating: f = 5 cm). (b) The detected SF spectrum (chirp 5000 fs^2) has a broad range from 1750 to above 3000 cm^{-1} (c) The transmission spectra of a polystyrene film are detected by the up-conversion method. They show the known vibrational resonances and an increase in spectral resolution when the amount of chirp is increased from 5000 fs^2 (green) to 7000 fs^2 (blue), 9000 fs^2 (red), and 12000 fs^2 (black). The SF spectra at a high spectral resolution correspond well with the FTIR reference measurement (grey background; resolution 1cm^{-1}). For illustration, an offset is added. (d) Taking the SF spectra as convolution of the molecular response and instrument response function into account, the FWHMs of the narrowband MIR spectra decrease by increasing the amount of chirp. (a & b) Adapted with permission from [2].

VII. Mid-infrared phase retrieval: a dispersion scan approach

Phase shaping provides access to a great variety of information in nonlinear spectroscopy [32, 157]. The shaping of NIR pulses, for example, can be exploited for background-free [35], phase-sensitive, and heterodyne [33, 34, 37] CARS spectroscopy as well as multimodal microscopy [20, 63]. Combined CARS and MIR microspectroscopy (chapter V) as well as SF spectroscopy (chapter VI) are made possible by applying phase-shaped NIR and MIR pulses. A fundamental requirement in all of these spectroscopic techniques is the precise knowledge of the optical phase

Several experimental methods have been developed to obtain the phase of a laser pulse. Aside from the shaper-based multiphoton-intrapulse-interference-phase-scan (MIIPS) method [158], the frequency-resolved-optical-gating (FROG) method [159] is the foundation for many methods, and its potential is demonstrated in applications ranging from the MIR [160, 161], the NIR/visible [162], and the UV [163, 164] regions. Phase information is provided by splitting the laser pulse into two replicas and scanning their time delay. In contrast to the FROG-based methods, the recently developed dispersion scan (d-scan) method [46, 165] does not require any pulse splitting and retrieves the phase in a single-beam setup by scanning the thickness of glass in its beam path. This compact setup makes the method attractive, as has already been shown for the visible and NIR regions [166, 167].

The phase retrieval of MIR pulses is more challenging due to difficulties in the setup alignment as well as the lack of suitable optics and spectrometers. In order to overcome such technical challenges, this chapter explains how NIR pulses can be exploited via an SF process in order to develop two novel d-scan methods.

These two MIR d-scan methods are presented in the following sections: Initially, the general concept of the d-scan method is summarised (section 1) and the two MIR d-scan methods are introduced (section 2). After discussing the experimental details of the nonlinear microscopy setup used in this work (section 3), the two methods' potential for MIR phase retrieval is demonstrated (section 4).

1. Dispersion scan method

The d-scan method [46] analyses laser pulses using a setup which consists of a pair of glass wedges, a nonlinear crystal, and a spectrometer (Figure VII.1a). The phases of the laser pulses are retrieved by scanning the thickness of the glass wedges and detecting

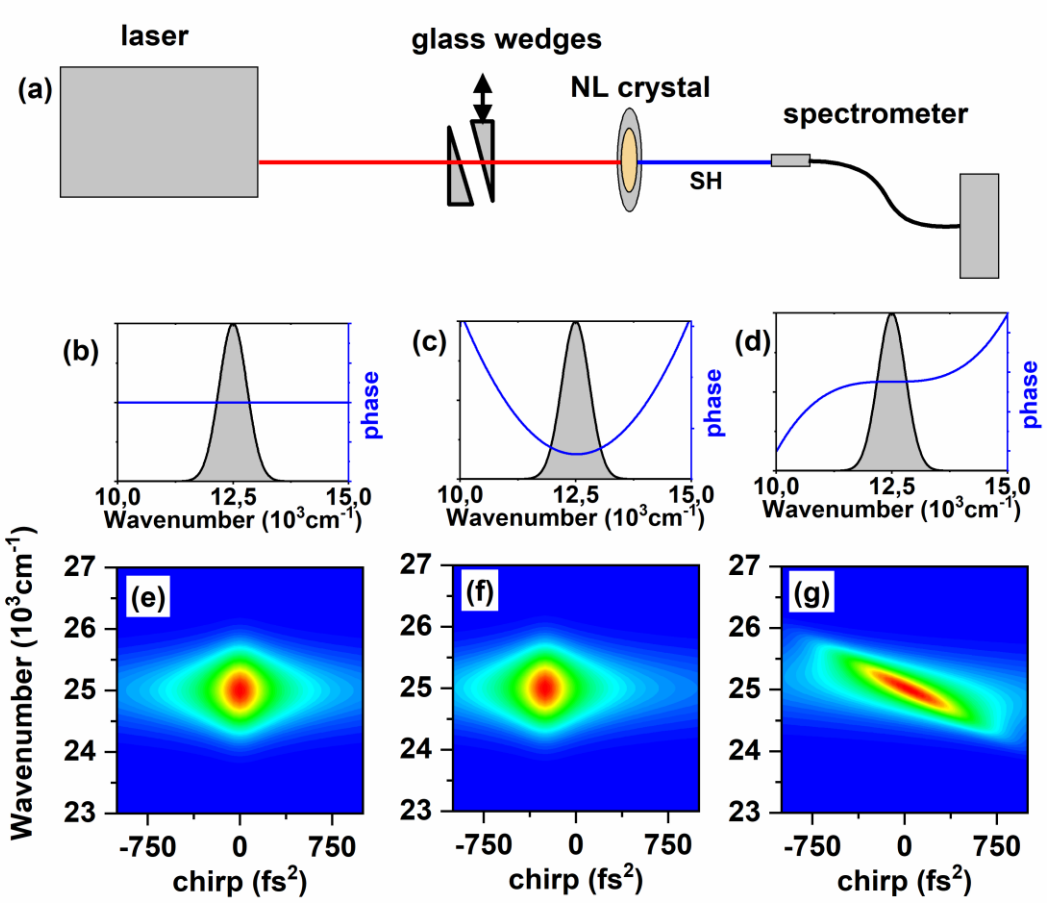

Figure VII.1 (a) The phase retrieval in the d-scan method is accomplished by scanning the thickness of glass wedges which generates second-harmonic light in a nonlinear crystal and detects the second-harmonic light with a spectrometer. (b-g) The impact of different phases on the d-scan traces is shown: (b & e) A constant phase yields a symmetric d-scan around the imprinted chirp 0. (c & f) An imprinted amount of chirp of 250 fs^2 results in a shift to -250 fs^2 of a d-scan trace with the same shape. (d & g) The d-scan trace of a cubic phase is tilted.

spectrally resolved the second-harmonic spectra. These spectra are collected in their dependence on the imprinted chirp in the so-called d-scan trace.

This d-scan trace contains the signature of the unknown phase of the fundamental laser pulses, as shown in Figure VII.1 b-g. Laser pulses with a constant phase, for example, generate a symmetric d-scan trace around chirp 0 (e), and its shape cannot be changed by an additional linear phase affecting only a time delay. A quadratic phase with a certain amount of chirp shifts the d-scan trace without changing its shape to the same chirp with the opposite sign (f). Furthermore, the shape of the d-scan trace is stretched and tilted by an imprinted cubic phase (g).

In order to retrieve these unknown phases $\varphi(\omega)$ quantitatively, two steps are required: In the first step, the d-scan trace S_{fit} is modelled in dependence upon the second-harmonic frequency ω and the amount of chirp β, which is imprinted via the phase $\theta(\omega', \beta)$ on the laser pulse (eq. VII.2). This laser pulse contributes to the d-scan trace by its complex electric field (eq. VII.1) with the amplitude $E_0(\omega')$ and phase $\varphi(\omega')$:

$$E\ \ (\omega') = E_0(\omega') \cdot e^{i\,\varphi(\omega')}, \tag{VII.1}$$

$$S(\omega,\beta) \propto \left|\mathcal{F}\left(\left\{\mathcal{F}^{-1}\left(E(\omega') \cdot e^{i\,\theta(\omega',\beta)}\right)\right\}^2\right)\right|^2. \tag{VII.2}$$

In the second step, this unknown phase $\varphi(\omega)$ is obtained in a fit by minimising the quadratic loss function L (eq. VII.3) between the measured d-scan trace $S_{meas}(\omega,\beta)$ and the modelled one $S_{fit}(\omega,\beta)$. The amplitude of $S_{fit}(\omega,\beta)$ is normalised beforehand via eq. VII.4. The multidimensional nonlinear fit is usually accomplished using the Nelder-Mead method (also called the downhill simplex method) [168]:

$$L = \sqrt{\int d\omega \int d\beta \left\{S_{meas}(\omega,\beta) - \mu \cdot R(\omega) \cdot S_{fit}(\omega,\beta)\right\}^2}, \tag{VII.3}$$

$$\mu = \frac{\int d\omega \int d\beta\, S_{meas}(\omega,\beta) R(\omega) \cdot S_{fit}(\omega,\beta)}{\int d\omega \int d\beta \left(R(\omega) \cdot S_{fit}(\omega,\beta)\right)^2}. \tag{VII.4}$$

(normalization)

Two aspects are important to obtain a good fit. Firstly, the parametrisation of the unknown phase must be well chosen. The phase can be expressed either in a Fourier base to describe simple phases or in a sparse approximation capable of expressing more complex phases. The latter is implemented by iteratively running the fitting algorithm several times. In each step, the phase is varied at a few spline frequencies and the whole phase is obtained by an interpolation. The best result of the former step is used in the next iteration, and the number of spline frequencies is increased [169]. The second aspect regards the need for an additional fit parameter. For this purpose, the so-called spectral response $R(\omega)$ is inserted as an amplitude factor to model effects like the spectral response of the spectrometer and the conversion efficiency of the crystal [46].

2. Mid-infrared phase retrieval

The phase retrieval of MIR pulses is demonstrated for two d-scan methods; the dual d-scan (2nd row) and the Xd-scan method (3rd row in Figure VII.2). Both methods exploit the SF spectra generated by the interaction with NIR pulses. Therefore, the complex electric field of the NIR pulses must be determined first. This is done using the shaper-based NIR d-scan method (1st row in Figure VII.2).

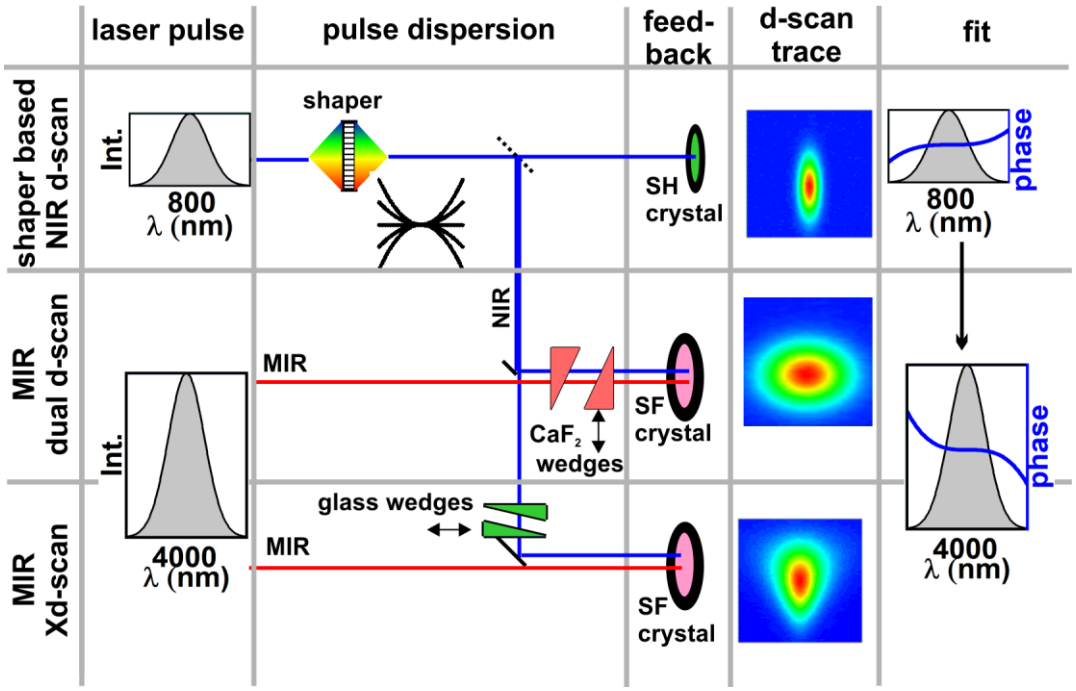

Figure VII.2 The dual d-scan method (2nd row) and the Xd-scan method (3rd row) are able to reconstruct the phase of MIR pulses. The methods are independent of each other and require the retrieved phase of the NIR pulses in the fit. This phase is obtained by the shaper-based NIR d-scan method (1st row). The shaper-based NIR d-scan is done by scanning the imprinted amount of chirp via a programmable pulse shaper and generating second-harmonic light in a nonlinear crystal (SH crystal). (2nd row) With the dual d-scan method, dispersion is imprinted on the NIR as well as on the MIR laser pulses by CaF_2 wedges and, SF light is generated in a nonlinear crystal (SF crystal). (3rd row) With the Xd-scan method, a pair of glass wedges is inserted into the NIR beam path to scan the SF spectra generated in the SF crystal. In both methods, the phase of the MIR pulses is retrieved independently in a fit, which accounts for the amplitude as well as the fitted phase of the NIR pulses.

2 i. Shaper-based NIR d-scan method

The shaper-based NIR d-scan method is implemented using the usual setup (see Figure VII.1a) with one modification. Rather than use glass wedges, the phases are directly applied with a programmable pulse shaper, which has the advantage of imprinting positive as well as negative amounts of chirp arbitrarily (1st row in Figure VII.2).

2 ii. Dual d-scan method

With the dual d-scan method (2nd row in Figure VII.2), the scan of the dispersion is made with optical wedges inserted in the collinear NIR and MIR beam path to disperse both laser pulses. In this setup, CaF_2 wedges are chosen to imprint the chirp (Figure VII.3a). The scan of the CaF_2 thickness indicates three different d-scan traces (see Figure VII.3b). Beside the two traces generated in a second-harmonic process of the individual laser pulses, the interaction of the NIR and MIR pulses provide the d-scan trace of the SF light.

This SF d-scan trace as well as the retrieved NIR phase from the shaper-based NIR d-scan method is used to retrieve the phase of the MIR pulses in a fit, which takes the imprinted phase of the CaF_2 wedges directly by taking the refractive index into account [170].

2 iii. Xd-scan method

In contrast to the dual d-scan method, the Xd-scan method is based on a scan of the temporal overlap between the NIR and MIR pulses, similar to the FROG method [159]. In this d-scan method, the NIR pulse is scanned temporally with respect to the MIR pulse by varying the thickness of glass wedges in the NIR-beam path (Figure VII.3c & d). The scan of the glass thickness in a limited range is enough to obtain the whole trace. Therefore, the additional imprinted chirp on the NIR pulses is negligible. This is shown in the result of a simulation, which depicts the temporal distributions of the laser pulses depending on the glass thickness (see Figure VII.3c). These distributions demonstrate a temporal confinement of the NIR pulses over the whole glass range without any signature of a chirp. If the chirp

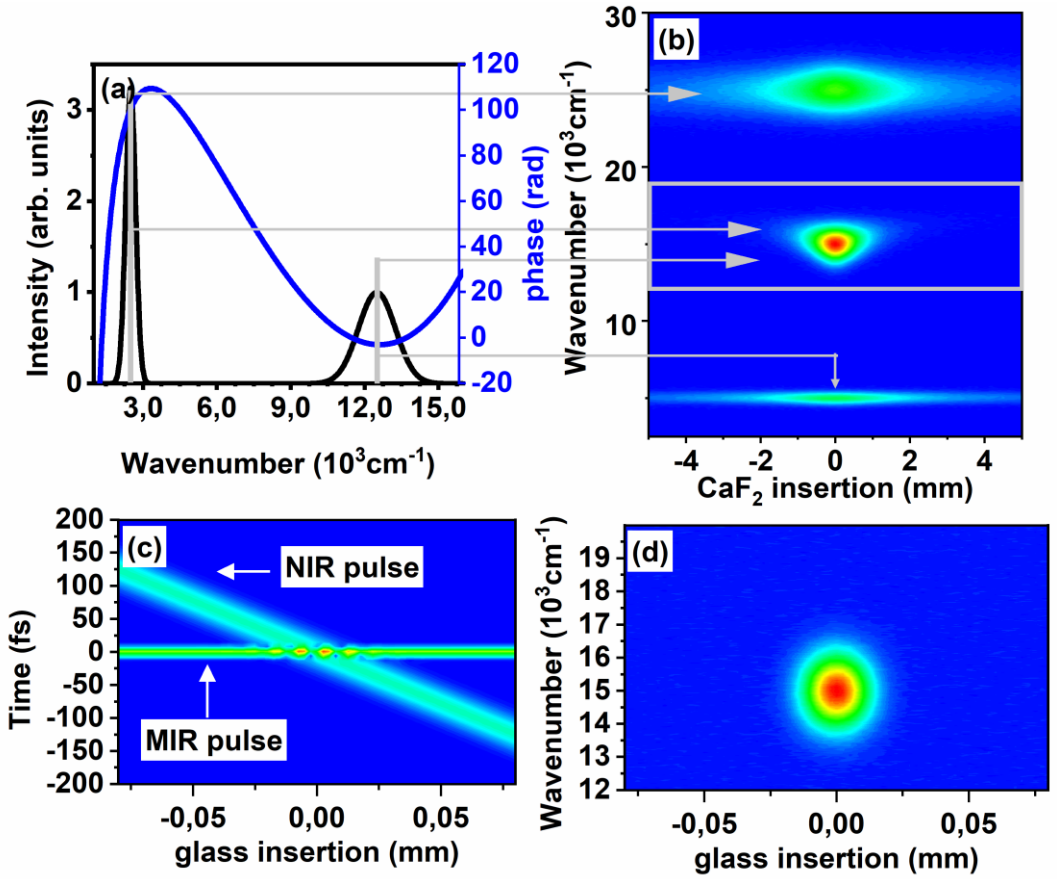

Figure VII.3 Principles of the dual d-scan (upper row) and the Xd-scan method (lower row). (a) In the dual d-scan method, CaF_2 wedges are inserted into the NIR and MIR beam path to imprint the CaF_2 phase (e.g. 5 mm thick substrate blue) on both laser spectra (black). (b) d-scan traces are generated by the MIR pulses (with a trace centred at 5000 cm^{-1}) and NIR pulses (with a trace centred at 25000 cm^{-1}), as well as by the SF process of both (middle). The latter is analysed in the dual d-scan method. (c) With the Xd-scan method, glass wedges are inserted into the NIR-beam path, and the NIR pulses are delayed to MIR pulses. (d) The temporal overlap in the Xd-scan method generates the SF light.

contributes to the imprinted phase, a temporal broadening at greater glass thickness would be observed.

The phase of the MIR pulses can be obtained by a fit that takes the Xd-scan traces and the retrieved NIR phase into account. The fit algorithm also models the insertion of the glass wedges by their refractive index and uses the same principles as in the dual d-scan method. It is important to emphasise that the SF process in this algorithm takes the measured NIR and MIR spectrum into account and is modelled via eq. VII.2.

Beside the individual fits of both methods, the phase can also be acquired by a global fit. To do so, the individual loss functions of both d-scan traces are summed to provide one fitted phase. This approach is shown below.

2 iv. Benchmarking

The potential of MIR phase retrieval is first demonstrated by simulations which use the experimental NIR and MIR spectra from SF spectroscopy (see chapter VI). A phase is imprinted on the MIR spectrum, and the d-scan traces are simulated for both methods (Figure VII.4a & b). This phase is reconstructed in the two individual fits of the methods and the global fit (Figure VII.4c & d). For all three fits, the results show good agreement between the imprinted and fitted phases over a broad spectral range (e). Therefore, the two MIR d-scan methods enable a phase retrieval over more than 1000 cm^{-1} (~3 µm for a centre at 5 µm).

The fitted phases also show small deviations at the edge of the MIR spectrum. These deviations are caused by small contributions in the d-scan traces coming from the edge of the MIR spectrum. The fit of this small contribution is inherently difficult due to the multidimensional fitting character of the d-scan algorithm. This algorithm is prone to get stuck at a local minimum especially while addressing complex phases over a broad spectrum. Consequently, the small contributions of the wings play a minor role in the fit result. This issue has been addressed in several publications in recent years [169, 171-173] and goes beyond the scope of the proof of principle demonstration in this work. An elaborate discussion of this issue and some opportunities for overcoming it are discussed in section 5.

Moreover, the fit performance is tested for both methods in a more quantitative way with a benchmark. In accordance, many synthetic d-scan traces are simulated with respect to the measured NIR and MIR spectrum as well as randomly generated MIR phases. The imprinted phases are a summation of quadratic (+/- 1000 fs^2), cubic (+/- 5000 fs^3), and oscillating contributions. In the benchmark, the shapes of these phases are retrieved by a fit and compared to the shape of the imprinted ones.

In the analysis, the error between the imprinted $\varphi(\omega)$ and fitted phase $\varphi'(\omega)$ is calculated by taking into account the spectral amplitude $E(\omega)$ of the MIR pulse. The error ranges from 0 for perfect fitting to 2 for two complete opposite phases after normalizing the integral of the spectrum to 1:

$$\mathrm{error}(\varphi,\varphi') = \left| \int d\omega \; \left| |E(\omega)| \cdot \left(e^{i\varphi(\omega)} - e^{i\varphi'(\omega)} \right) \right|^2 \right|^{\frac{1}{2}}. \qquad \text{VII.5}$$

The error distribution is depicted for the two individual fits and the global fitting in histograms, which show a small error for all contributions (Figure VII.5). Furthermore, it is also observed that the performance of the Xd-scan is better than the dual d-scan.

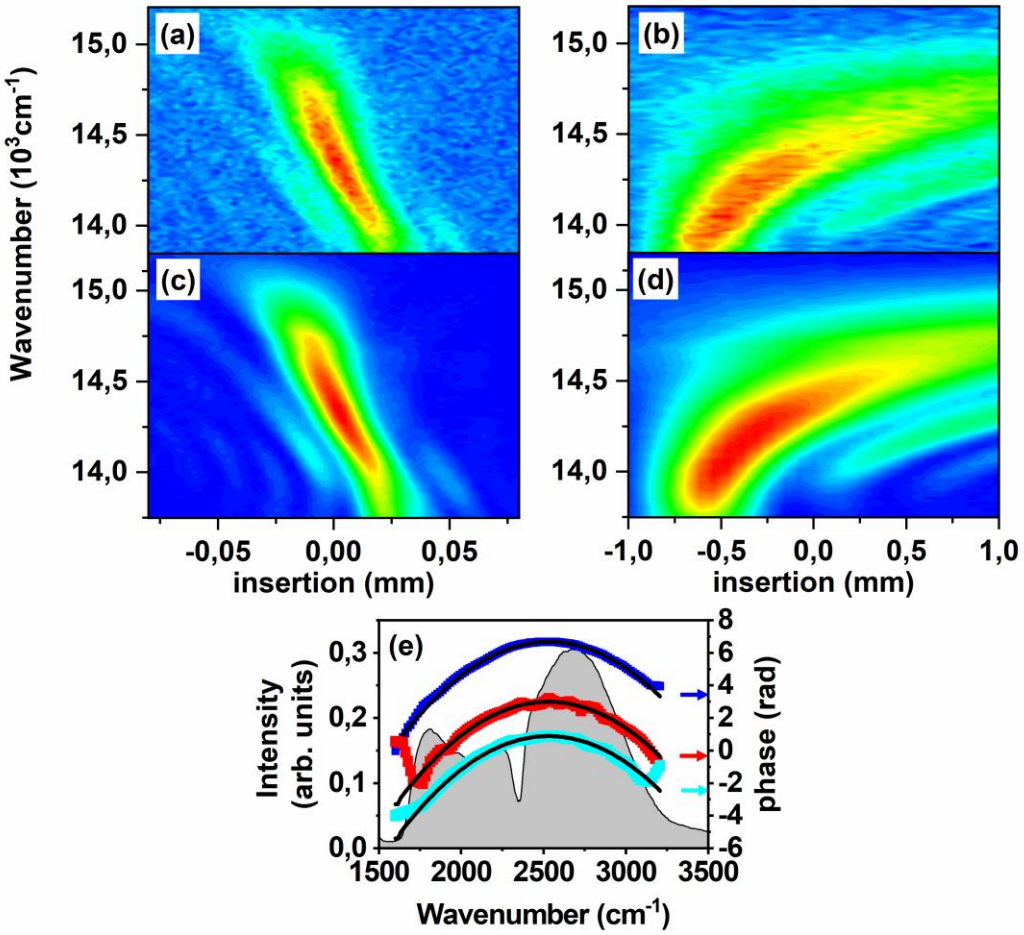

Figure VII.4 The performance of the Xd-scan method (a & c) and dual d-scan method (b & d) is demonstrated by simulations. The d-scan traces of the Xd-scan method (a) and dual d-scan method (b) are generated synthetically with a high amount of chirp. The fitted Xd-scan (c) and dual d-scan (d) trace show good agreement with the simulated traces. (e) The phases obtained by the Xd-scan (blue) and the dual d-scan method (red) agree well with the imprinted phase (black) across the MIR spectrum (background). In addition, the fitted phase is obtained in a global fit by taking both methods into account (cyan). The fit in all d-scan methods is performed by a sparse approximation with four iterations. It is important to note that the offset of the glass insertion can be arbitrarily chosen. The glass insertion at 0 mm is the centre of the glass wedges in all d-scan traces. The simulated d-scan traces have a noise level of 10%.

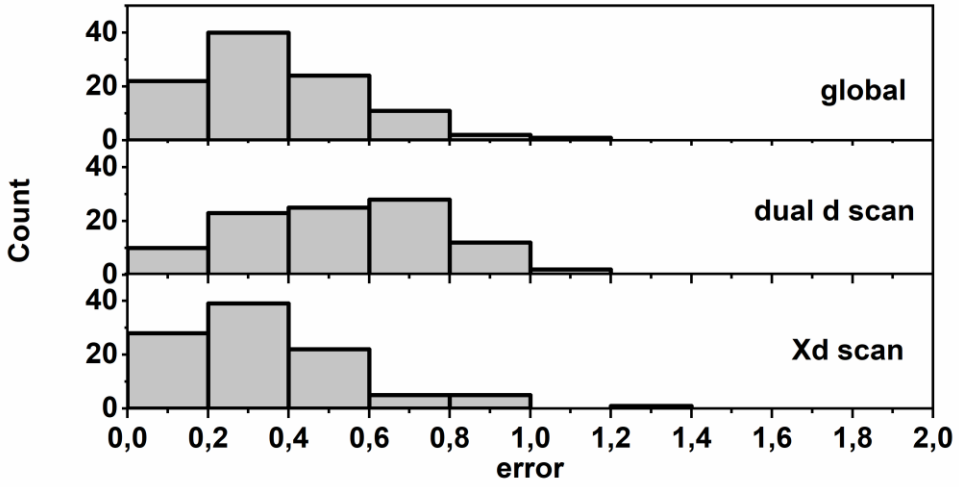

Figure VII.5 Error histogram of the fit performance for the Xd-scan (lower) and dual d-scan (middle) method as well as a global fit of both methods.

3. Experimental details

The potential of the MIR phase retrieval is demonstrated in the non-linear SF microscopy setup (Figure VII.6), as already used and described in chapter VI. It is important to remember that the spectrum of the NIR pulses has a sharp edge at 12500 cm^{-1} via an 800 nm long-pass filter.

The phase of the NIR pulses are determined by the NIR d-scan method, which is implemented by inserting a 20 µm thick beta Barium Borate (BBO) crystal in the focal plane of the microscope which generates the second-harmonic spectra in the point of interest for SF microscopy. These spectra are detected by a fibre spectrometer (Ocean Optics 4000). The scan of the imprinted chirp is made with the previously used liquid crystal pulse shaper.

The two d-scan methods in the MIR region are implemented using a 100 µm thick $LiIO_3$ crystal in the microscope, whose broadband conversion efficiency has been shown experimentally (see appendix section IX.5 i). For the dual d-scan method, a pair of CaF_2 wedges (angle 4°) is inserted into the collinear beam path behind the MIR generation and the scan is accomplished by a resonant piezoelectric motor (Thorlabs ELLK 17). A pair of glass wedges (angle 30') is inserted behind the 800 nm long-pass filter for the Xd-scan, and the thickness of the glass in the NIR-beam path is scanned with a step motor (PI M531 DD1).

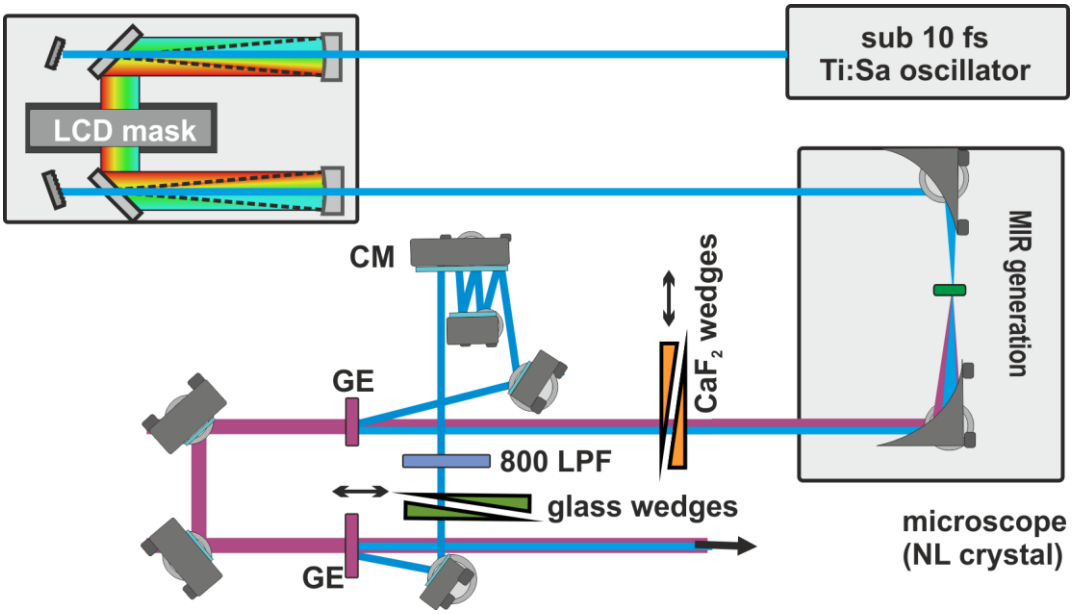

Figure VII.6 Experimental setup of a shaper-based d-scan. The setup of chapter VI (Figure VI.6) is extended to determine the NIR and MIR phases. The NIR pulses are shaped via the pulse shaper inside the 4f setup and generate MIR pulses in a 1 mm thick $LiIO_3$ crystal. Afterwards, the NIR and MIR pulses pass the CaF_2 wedges (4° angle) and are then split on a germanium beam splitter (GE). The NIR pulses pass two chirped mirrors (-1000 fs^2), an 800 nm LPF filter and a pair of glass wedges (angle 30') before they are recombined with the MIR pulses on a second germanium filter. The combined NIR and MIR pulses are guided in the microscope, which have a 20 µm thick BBO and a 100 µm thick $LiIO_3$ in the focal plane for the NIR and MIR d-scan methods, respectively.

The spectra of the fundamental NIR and MIR pulses are also needed for the phase retrieval. While the NIR spectrum is simply obtained with a fibre spectrometer (Ocean Optics 2000+), the broadband MIR spectrum is detected using a single-channel detector in a tuning of a narrowband MIR spectrum. The obtained envelope spectrum is similar to the broadband MIR spectrum (see chapter IV).

4. Experimental application

4 i. Near-infrared phase retrieval

Figure VII.7 shows the phase of the NIR pulses which is experimentally obtained in the microscope. The fitted d-scan trace corresponds well with the measurement, providing a phase which is constant up to 12000 cm^{-1}, as expected. This phase increases tremendously at the edge of the NIR spectrum due to the 800 nm long-pass filter. The direct connection between the filter and the phase change can be corroborated using two considerations. Firstly, NIR pulses not impacted by the 800 nm long-pass filter have a constant phase at

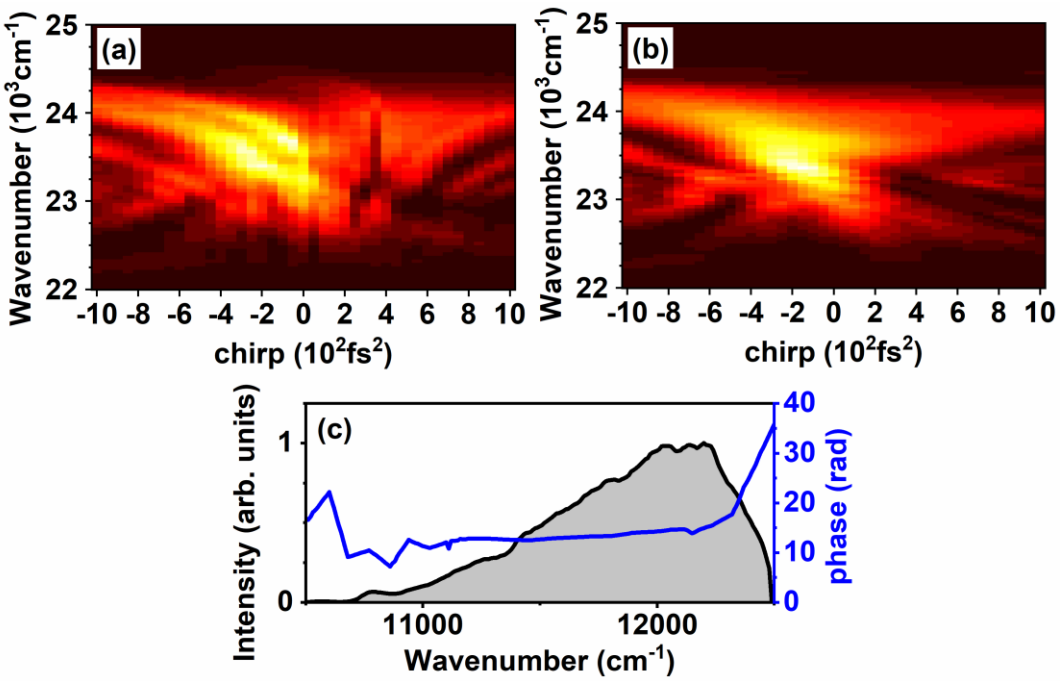

Figure VII.7 Experimental demonstration of the shaper based NIR d-scan method. (a & b) The fitted d-scan trace (b) agrees well to the measured one (a) after performing the fit, which uses the sparse approximation (4 iteration). (c) The fitted phase (blue) has a tremendous increase at the edge of the NIR spectrum (grey background) due to the 800 nm long-pass filter.

800 nm (see appendix Figure IX.5). Secondly, the coated layers of the 800 nm long-pass filter change the transmission at 800 nm by varying the phase at the spectral edge.

4 ii. Mid-infrared phase retrieval

The potential of the dual d-scan and the Xd-scan method is shown experimentally by scanning the glass thickness from -1 mm to 1 mm and -80 µm to 80 µm, respectively (see Figure VII.8a & b). In both scans, the position 0 of the glass insertion is chosen as the centre of the scanning range. In order to probe the same MIR phase in both methods, this position is adjusted for each method during the scan of the other one. Furthermore, these positions are also chosen during the shaper-based NIR d-scan to provide the information of the NIR complex electric field in consideration of the optical wedges.

The fittings are performed separately for the two methods as well as in a global fit (see Figure VII.8c-e). The three fits agree well with the measurements, and the obtained phases coincide between 1800 cm^{-1} and 2800 cm^{-1}. They indicate a positive chirp from 1750 cm^{-1} to 2350 cm^{-1}, an oscillating contribution over the whole spectrum, and a phase jump at 2350 cm^{-1}. Furthermore, they show a discrepancy above 3000 cm^{-1}, which can be traced back to the multidimensional fitting problem (see section 2 iv).

Furthermore, the MIR methods are tested by retrieving the phase imprinted on the laser pulses with an additional substrate. This phase is compared to the one obtained theoretically in consideration of the well-known dispersion from the literature [170]. For this purpose,

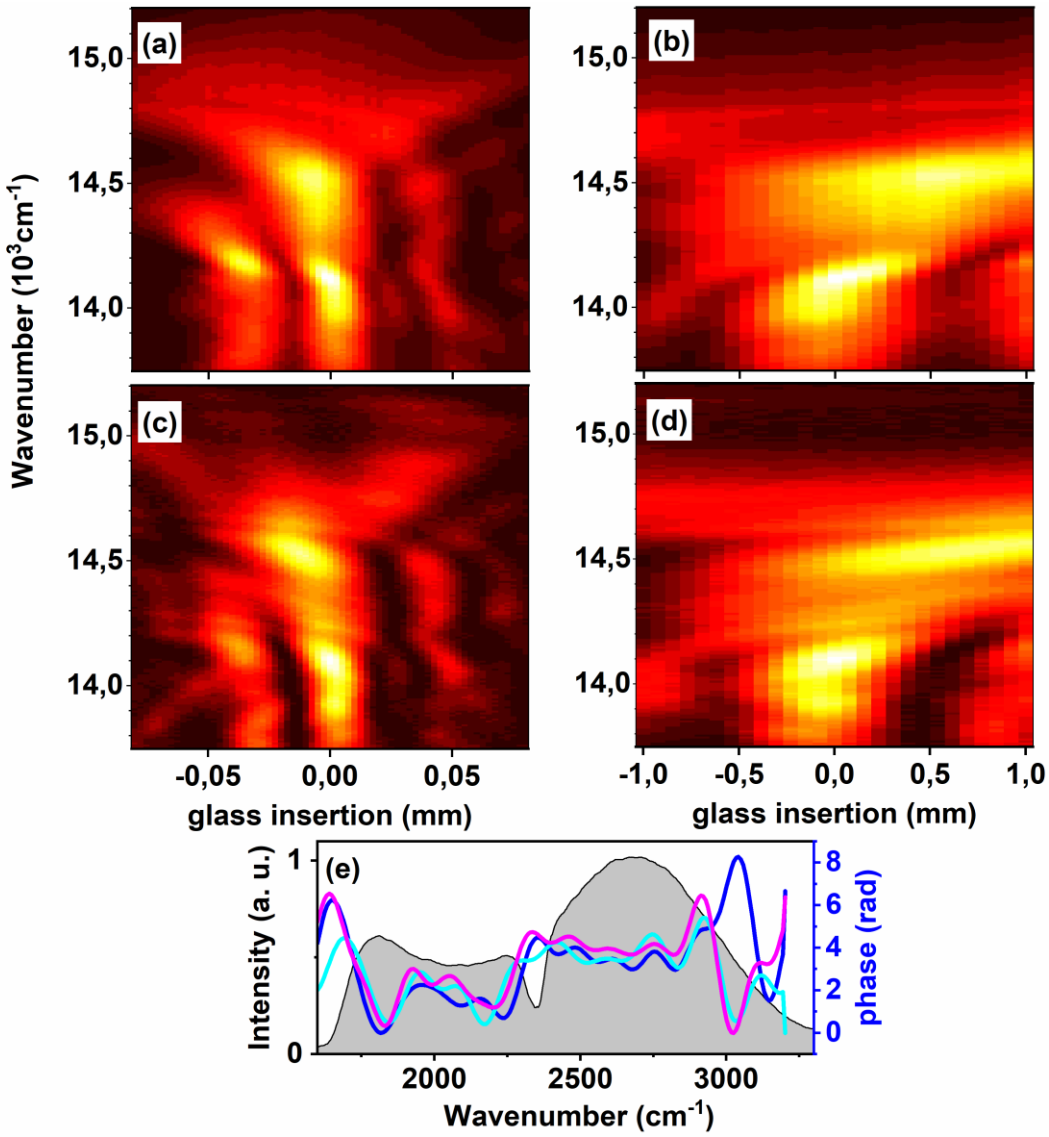

Figure VII.8 MIR phase retrieval via the two MIR d-scan methods. The measured Xd-scan (a) and the dual d-scan (b) traces are fitted with a constant spectral response and two steps in the d-scan algorithm. In the first step, a sparse approximation (using four iterations) is used, and the obtained result is further optimized in the second step by a fit, which expresses the phase in the Fourier base (40 parameters). The fit is performed independently for both methods (not shown) and in a global fit. The fitted Xd-scan (c) and dual d-scan (d) traces are depicted for the global one. (e) The fitted phases (Xd-scan [in blue], dual d-scan [in cyan], and global fit [in purple]) agree with each other between 1800 cm^{-1} and 2800 cm^{-1}. In the background, the MIR spectrum is shown.

CAF_2 substrates are inserted in the MIR-beam path, and the phase of the MIR pulses is retrieved by a global fit of both d-scan traces. After subtracting the original phase of the MIR pulse, the retrieved phase indicates the CaF_2 imprinted phase as well as an additional linear phase. The latter phase corresponds to a time delay and does not contribute to the d-scan traces. This linear contribution is subtracted in order to compare the retrieved phase directly to the literature.

For the test, the phase is retrieved for a reference (without any additional CaF_2 substrate) as well as for a 1 mm and 2 mm thick CaF_2 substrate (see Figure VII.9). The phases agree

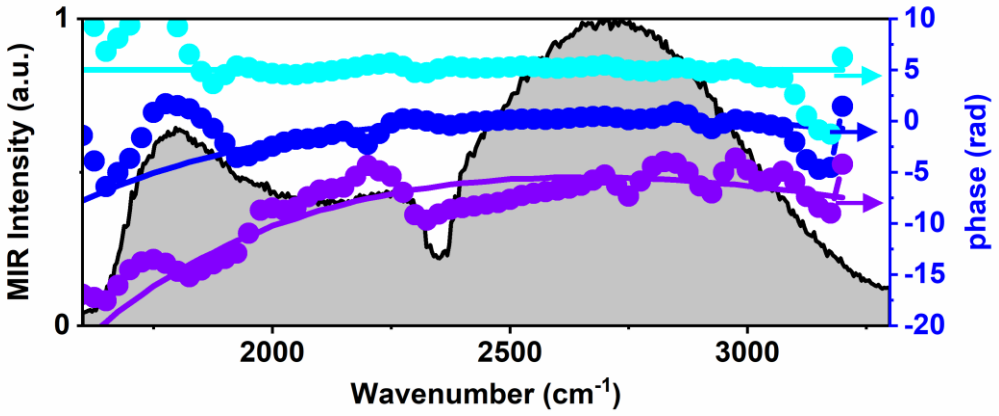

Figure VII.9 The phase of a 0 mm (cyan dots), 1 mm (blue dots) and 2 mm (purple dots) thick CaF_2 substrate is retrieved by the global fit and compared to the theoretical phases (solid lines).

well with the theoretical phase between 1800 cm^{-1} and 3000 cm^{-1}. The retrieved phase of the 2 mm thick CaF_2 substrate shows, however, a jump at 2350 cm^{-1}. This phase jump matches an absorption band of CO_2 and can be directly linked to a phase, which is imprinted by the CO_2 inside the humid air. This interpretation is further corroborated by detecting the MIR vibrational modes of a polystyrene film with phase sensitivity (see Figure IX.6 in appendix).

5. Outlook

As mentioned (see section 2 iv), the multidimensional-fitting character is responsible for the deterioration of the phase retrieval at the edge of the MIR spectrum. Several publications have already addressed this problem. All of them replaced the Nelder-Mead algorithm by a more sophisticated fitting algorithm. Kleinert *et al.* [171] use, for example, deep neural networks as a fitting method. After training a network with many synthetic, generated d-scan traces, it is able to retrieve the phase within a few milliseconds. This network is based on the DenseNet network and solves the fitting as an image recognition task by comparing the fitted and measured d-scan traces. Another interesting approach has been shown by Geib *et al.* [172]. They developed a new pulse retrieval algorithm which exploits the Levenberg-Marquardt algorithm. It is interesting to note that both approaches use gradient-descent-based algorithms, whose potential for the fit of data with Gaussian noise is well-known.

Furthermore, the programmable pulse shaper makes it possible to solve the fitting problem experimentally. The pulse shaper allows one to control the MIR generation by shaping the NIR pulses accordingly. Therefore, it can supress the central part of the MIR spectrum for some SF spectra in the d-scan trace. This relatively enhances the intensities at the edges of the MIR spectrum and their impact on the d-scan trace. Therefore, a fit on this trace can only be accomplished by retrieving the right phase also at the edge of the MIR

spectrum. It is important to note that this approach requires the exact knowledge of the impact of the pulse shaping on the MIR generation since this must be considered in the phase retrieval.

VIII. Summary and outlook

1. Summary and discussion

In this thesis, several vibrational sensitive techniques have been successfully combined in multimodal microscopy. A special attention was given to add techniques in a non-linear Raman microscope, which access molecular vibrations with high spectral and spatial resolution via direct MIR excitations. For that purpose, a new MIR light source was developed and implemented, which provides laser pulses with arbitrary temporal and spectral shape by using flexible pulse shaping. The pulse shaping makes it possible to have five different nonlinear techniques in a compact setup and to control two different laser pulses covering a spectral range over more than 5000 cm^{-1}. The main results of this thesis are summarised below.

Although MIR microscopy is of great interest for material and life sciences, its broad application is hindered by the lack of technical progress of MIR light sources. This has been successfully addressed in this thesis with the development of a new MIR light source for microscopy (chapter IV). This new MIR light source has been implemented in a single-beam setup by inserting a nonlinear crystal in the Raman microscopy setup and by generating MIR pulses in a DF process. The spectral shape of these MIR pulses is arbitrary due to the flexible shaping of the driving pulses. Therefore, broad MIR spectra have been switched to narrowband and tuneable ones simply by changing the imprinted phase on the pulse shaper. In this work, a tuning bandwidth of more than 2000 cm^{-1}, from 1250 up to 3500 cm^{-1}, has been achieved using a thin $LiIO_3$ crystal. Although the choice of the crystal is a crucial issue and determines the spectral bandwidth, the concept of the new MIR light source is universal and not restricted to a specific spectral range.

Another highlight of this work is how it combines MIR transmission and CARS microspectroscopy in one setup (chapter V). By acquiring both signals at the same position in the sample, the spectra and images can be directly compared without any distortion, which would be induced using two separate setups. Furthermore, the combination of CARS and MIR microspectroscopy merges their advantages and overcomes their disadvantages. CARS microscopy, for its part, contributes vibrational resonant images with high spatial resolution. MIR transmission spectroscopy has the advantage of taking spectra with high sensitivity over a broad range at specific positions in the same sample. The combined microspectroscopy was demonstrated in a proof of principle using human dermis and polymers. MIR and CARS microspectroscopy have been implemented solely with the

concept of spectral focusing via the pulse shaper. This concept provides spectral resolution in both processes with a narrowband DF excitation and even enables the arbitrary adjustment of this resolution. This has been demonstrated on the new MIR light source by tuning the spectral width from more than 100 cm^{-1} down to 20 cm^{-1} (see section IV.5 ii). The arbitrary spectral resolution has the advantage of being able to adapt the laser pulses either to spectroscopy, by providing higher spectral resolution, or to microscopy. For microscopy, the spectral width of the DF excitation is tuned to directly match the spectral width of the vibrational mode in order to acquire the highest signal intensities.

SF microspectroscopy thus far has been largely absent from the repertoire of nonlinear techniques inside a microscope. This work has demonstrated several novel variants of SF by arbitrarily exploiting shaped NIR and MIR pulses (chapter VI) This flexible pulse shaping allows the application of a homodyne MIR-scanning and a heterodyne multiplex method, in which the spectral resolution as well as the switching between them depend only on a programmable pulse shaper. The methods have been applied in series to combine the high signal intensities in the homodyne MIR-scanning method with the potential to acquire the whole SF spectrum with only three shots in the heterodyne multiplex method. Furthermore, the latter method has been extended to solve the problem of large non-resonant backgrounds in many samples. An adjustment of the imprinted phase on the pulse shaper has reduced the non-resonant background in the presented example by more than a factor of 20. Both SF methods have shown their potential for analysing molecular vibrations in non-centrosymmetric systems. This was demonstrated on cysteine microcrystals and cholesterol.

Phase shaping is only efficient when the phase is well-known beforehand. This requires a phase retrieval which can be accomplished in a compact setup using the recently developed d-scan method [46]. This method has been extended in the presented work in order to determine even the phases of MIR pulses over more than 1000 cm^{-1} in addition to the NIR phases (chapter VII). The extension of this method is based on the interaction of the MIR and NIR pulses in an SF process. The MIR phase retrieval benefits from this SF process by a detection with highly sensitive detectors in the visible. Furthermore, the intense NIR pulses generate high signal levels which cannot be provided by the second-harmonic process of the MIR pulses. By exploiting these NIR pulses, two independent MIR phase retrieval methods have been developed. Whereas the Xd-scan method relies on a time delay between the NIR and MIR pulses, the dispersion imprinted on both laser pulses is scanned using the dual d-scan method. These d-scan methods have been also combined in a global fit, which retrieves one phase with a better goodness of fit than the individual methods. In accordance with the similarity between the Xd-scan and FROG methods, this global MIR phase retrieval denotes a further step in the implementation of a uniform and powerful method which uses a robust algorithm to analyse the traces of different phase retrieval methods [172]. In addition, two major advantages have been shown with the d-scan methods in the shaper-based microscopy setup. Firstly, the phase retrieval of the NIR pulses is obtained by exploiting the programmable pulse shaper, which provides a simple adjustment of positive as well as negative amounts of chirp. This shaper overcomes the typically static setup in a flexible way and allows for the direct compensation of the retrieved phase.

Secondly, the phase retrieval has been accomplished directly in the focal plane of the microscope and therefore does not require any further optical setup.

In summary, a new MIR light source adds MIR transmission and SF microspectroscopy to a setup, which is also capable of CARS, second-harmonic, and two-photon excited fluorescence microscopy. This light source is based on flexible pulse shaping and offers laser pulses with various MIR spectra.

2. Outlook

Several applications of a tailored MIR light source were already demonstrated in this work. Possible future applications as well as some suggestions for improving the existing setup are discussed in this section.

For nonlinear spectroscopy in general and for the presented setup in particular, low-signal intensities are a critical issue. Therefore, the small intensity of the new MIR light source is the major bottleneck for new applications. More intense MIR pulses can be generated by replacing the Ti:Sa oscillator with a laser system that provides higher pulse energies. Possible candidates are the commercially available optical-parametric-chirped-pulse-amplification (OPCPA) systems, which offer intense NIR pulses with high repetition rates [174]. In an initial test, MIR transmission spectroscopy was successfully applied and an enhancement of the MIR intensity by a factor of 390 was already obtained.

An external local oscillator provides another interesting possibility for increasing the SF signal in the heterodyne multiplex method. This local oscillator can be implemented in the presented setup by using the reflection on the 800 nm long-pass filter due to the perfect overlap of its spectrum with the SF light (Figure VIII.1a). By having much higher signal intensities than the intrinsic local oscillator used in this research, this external oscillator can enhance the signal levels in a simple way. This was already shown in a first test (see in appendix IX.4). The obtained amplification is well above the required amplification factor of 10, which is needed for hyperspectral imaging using the heterodyne multiplex method.[1]

The phase of the MIR pulses is a further critical issue, which has a high impact on the SF generation. In order to enhance the SF signals, this phase should be as flat as possible. Unfortunately, the MIR phase in the presented setup is influenced by oscillating contributions, as shown experimentally (see chapter VII). Future works can address this problem by separating the MIR generation from the NIR pulses used in the SF process (Figure VIII.1b). This can be done by aligning two independent beam paths for the NIR pulses. In the first beam path, MIR pulses are generated by pump and Stokes, which have a small angle between them. This allows for the direct suppression of the NIR pulses by a spatial filter [112]. In the second beam path, a programmable pulse shaper generates shaped NIR pulses. The generated MIR and shaped NIR pulses path parallel at a certain distance to

[1] This factor is estimated by the comparison of the signal levels in the homodyne MIR-scanning and heterodyne multiplex method.

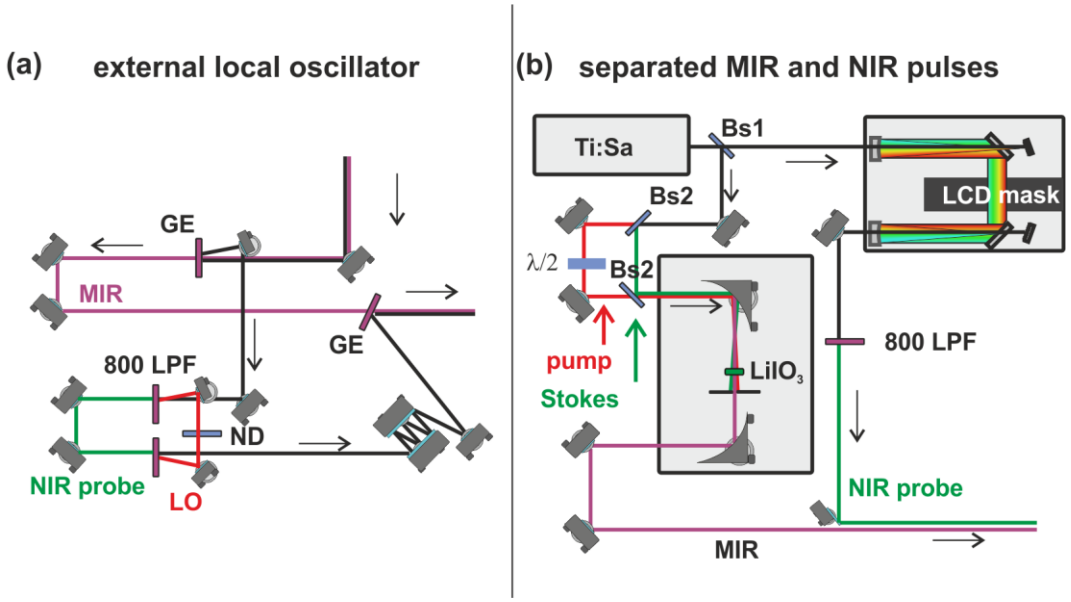

Figure VIII.1 Setups for implementing an external local oscillator for the heterodyne multiplex SF spectroscopy (a) and separating MIR and NIR pulse generation (b). (a) The MIR and NIR pulses are separated on a germanium beam splitter (GE) by transmitting the MIR pulses (purple) and reflecting the NIR pulses (black). The NIR pulses are split on an 800 nm long-pass filter (800 LPF). The transmitted part is the probe part (green) and the reflected part acts as local oscillator after it is reduced by a ND filter (red). The NIR pulses are recombined on another beam splitter (800 LPF). The NIR pulses pass the chirped mirror and are recombined with the MIR pulses on a germanium substrate (GE). (b) NIR pulses are split on a beam splitter (Bs1). The transmitted pulses pass the pulse shaper and the 800 nm long-pass filter (800 LPF). They are guided towards the microscope. The reflected pulses are split in pump (red) and Stokes (green) on a dichroic beam splitter (Bs2). The polarization of the Stokes is rotated around 90° by a λ/2 beam splitter. After the pump and Stokes are recombined on another beam splitter (Bs2), they have a small angle inside the $LiIO_3$ crystal, and the generated MIR light is spatially separated from them. A pin hole only transmits the MIR pulses. They are guided towards the microscope. Notably, the Stokes in (b) and the NIR probe pulse in (a) have the same spectrum.

the objective and first meet inside the sample. This setup has two main benefits. Firstly, the NIR-MIR beam splitters are no longer needed and consequently their dispersion is not imprinted on the MIR pulses. Secondly, this setup allows for the shaping of the NIR pulses independently from the MIR generation. Therefore, the shaped NIR pulses can compensate the MIR phase to generate the SF light efficiently. It is important to note that the presented setup is only suitable for the heterodyne multiplex method and cannot be used for the homodyne MIR-scanning method.

Furthermore, the setup developed in this work can be used for other applications without the need for any major modifications. The generation of multiple MIR and NIR pulses as well as the development of a universal shaping method are presented below.

Multiple MIR and NIR pulse generation: Time resolved spectroscopy is a powerful method for investigating the molecular dynamics of new materials [175, 176]. The short and ultrabroadband NIR and MIR pulses in the presented setup allow new applications in time resolved spectroscopy by giving access to the dynamics of molecular vibrations. A first application could be a NIR pump and MIR probe experiment. However, the intrinsic

temporal overlap between NIR and MIR pulses must be overcome to establish the arbitrary time delay between these pulses. This can be accomplished by splitting the NIR pulse into two pulses and controlling the polarisation of the two NIR pulses. In the use of the shaping method ‘multiple-independent-comb-shaping (MICS)’ [177], the polarisation is chosen in a way that only one of the NIR pulses generates a MIR pulse in accordance with phase matching. After the NIR pulses have passed several filters and polarisers, one NIR and one time-delayed MIR pulse are generated. Therefore, a NIR pump and MIR probe experiment is created. This can be used, for example, to investigate the thermal properties of graphene [178-180]. Additionally, the MICS concept can be exploited to generate more than two laser pulses. Three MIR pulses and a delayed NIR pulse can be obtained in a specific configuration of the NIR polarisation. These laser pulses can be used in multidimensional time-resolved spectroscopy in order to access the coupling between vibrational modes [181, 182]. The three MIR pulses subsequently generate coherences in the molecules, which build up a photon echo. This can be detected using a heterodyne method via an SF process by interacting with the NIR pulse.

Development of a universal shaping method: The development of a universal and global shaping method has been a long-standing dream in shaper-based microscopy. Such a method combines several advantages of different methods by applying more complex phase functions. With the flexibility of the presented multimodal microscopy setup on the one hand and the recent success of deep neural networks on the other [171, 183, 184], the development of a global shaping method is possible. In SF spectroscopy, for example, this is achieved by training the neural networks in supervised learning with synthetic data. These data can be acquired by modelling the measurement precisely in simulations as already demonstrated in section VI. Afterwards, the trained network is able to retrieve the SF spectra within a few milliseconds. Furthermore, the analysis can be done simultaneously with an iterative measurement by using neural networks. The network analyses the data after each measurement step and predict the phase function of the shaper for the next measurement step. Therefore, the network directly controls the data acquisition and has the potential to speed up the measurement while increasing the sensitivity.

Ultimately, combining pulse shapers and neural networks represents a promising connection helping pave the way towards quantum control.

IX. Appendix

1. List of abbreviations

eq.	equation
CARS	coherent anti-Stokes Raman scattering
SF	sum-frequency
DF	Difference-frequency
MIR	mid-infrared
NIR	near-infrared
IFD	instantaneous frequency difference
IRF	instrument response function
MRF	molecular response function
BBO	beta Barium Borate
CCD	charged coupled device
FWHM	full width half maximum
MEM	maximum entropy method
NA	numerical aperture
PE	polyethylene
GDD	group-delay-dispersion
LO	local oscillator

2. Spectral focusing concept in the time domain

A full derivation of the spectral focusing concept can be derived in time domain by imprinting the temporal parabolic phases $\frac{1}{2\beta}t^2$ on the electric field $E_i(\mathrm{t})$ of pump and Stokes ($i \in \{p, S\}$). Pump and Stokes are highly stretched in time (Figure IX.1a);

$$E_i(\mathrm{t}) = E_{i,o}(t) \cdot e^{i\left\{\omega_i + \frac{1}{2\beta}t\right\}\cdot t} \text{ with } i\epsilon\{p, S\}. \qquad \text{IX.1}$$

By generating a DF excitation $A(t)$ with pump and Stokes, the interference of the stretched pump and Stokes generate a beating:

$$A(t) \propto \left|E_p\left(t - \frac{\tau}{2}\right)\right| \left|E_S^*\left(t + \frac{\tau}{2}\right)\right| e^{i\Delta\phi(t)}, \qquad \text{IX.2}$$

$$\Delta\phi(t) = \left(\omega_p - \omega_S - \frac{1}{\beta}\tau\right) \cdot t. \qquad \text{IX.3}$$

This beating is exemplarily shown in Figure IX.1b: For an imprinted amount of chirp of 3500 fs^2 and no additional time delay, the pump and the Stokes interfere constructively with the periodicity of T=16,6 fs. This is linked to a narrowband excitation at 2000 cm^{-1} [7]

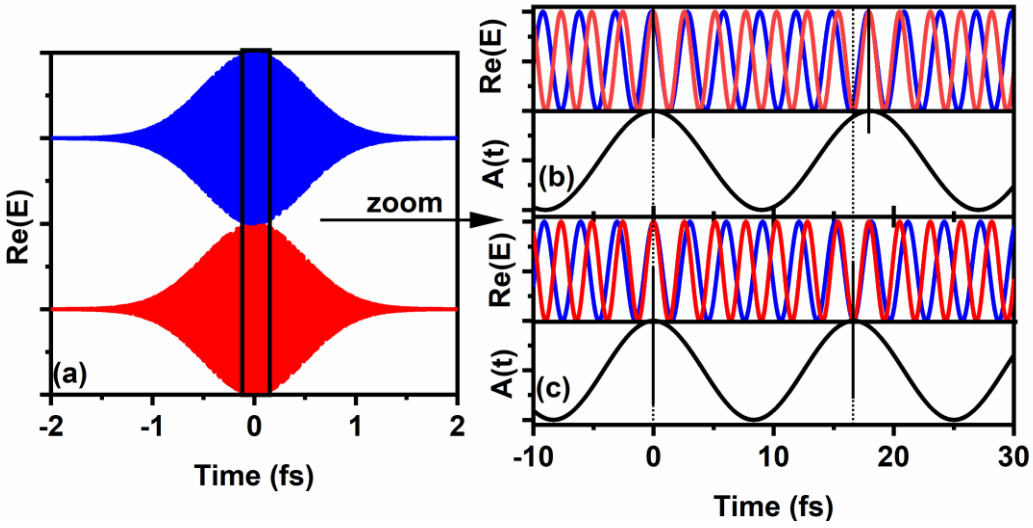

Figure IX.1 Demonstration of the spectral focusing concept in time: (a) The pump with a frequency of 13000 cm^{-1} (blue) and the Stokes (11000 cm^{-1}; red) are stretched by a chirp of 3500 fs^2 in time. (b) A zoom shows that pump and Stokes interfere with a constant *IFD* . This *IFD* is observed in the DF excitation *A(t)* (black). (c) A temporal shift of the pump with respect to the Stokes detunes the constructive and destructive interference of pump and Stokes. The *IFD* of *A(t)* is changed.

[7] $\Omega = \frac{1}{T \cdot c}[\mathrm{cm}^{-1}]$

This narrowband excitation can be tuned to $\Omega = \omega_p - \omega_S - \tau/\beta$ by an additional time delay τ between pump and Stokes shifting the constructive interferences (Figure IX.1c).

3. Focusing condition for MIR generation

In order to increase the power of MIR pulses, the focusing of the driving pulses into the crystal can be varied. By reducing the focal length of the mirrors, the spot size in the crystal is decreased, which increases on its turn the MIR generation. However, there are several aspects, which hinder the use of too small focal lengths. The two main limitations are the damage threshold and the phase matching condition of the crystal. Moreover, the anisotropy of the crystals hinders by the so-called spatial walk-off the use of too short focal lengths. In order to understand this, it is important to know that the pump pulse polarized in extraordinary axis is shifted spatially by the distance $\delta = L\tan(\varphi)$, while traversing the crystal. Therefore, MIR generation cannot take place over the whole crystal length L due to vanishing temporal overlap between pump and Stokes. This takes especially place in the use of extreme small spatial spots of pump and Stokes.

This is quantitatively analysed in the following by calculating the spatial walk-off and the MIR generation in consideration of the spatial overlap between pump and Stokes.

The spatial walk-off δ depends via the deflection angle φ on the phase matching angle θ and the refractive index $n_{eo}(\theta)$ of the crystal [58]. For the $LiIO_3$ crystal the spatial walk-off is $\frac{\delta}{L} \approx 56\ \frac{\mu m}{mm}$;

$$\tan(\varphi) = -\frac{\frac{\partial n_{eo}}{\partial \theta}}{n_{eo}}. \qquad \text{IX.4}$$

The impact of the spatial walk-off on the MIR generation is numerically analysed. In accordance, a Gaussian beam (w=1 mm) is focused inside a crystal and generates the MIR intensity in the interaction area A(x,y) of the pump and Stokes over the crystal length L[58]:

$$I_{MIR}(L) \sim \int_0^L \left(\frac{1}{A(x,y,z)}\right)^2 dz. \qquad \text{IX.5}$$

This simple model is used to analyse the dependence of the generated MIR intensity on the crystal length (i) as well as on the focal length (ii).

(i) Assuming an ideal DF generation- without any spatial walk-off $A(x,y,z) = A(z)$ and an infinite focal length $A(z) = A$ – the MIR intensity increases quadratically with increasing crystal length. This situation changes by taking the spatial walk-off into account. In this case, the Gaussian beams of pump and Stokes are split spatially by δ and the spatial overlap as well as the MIR generation vanishes inside the crystal. Therefore, the quadratic dependence of the MIR generation on the crystal length is deteriorated. The MIR generation in a 1 mm thick $LiIO_3$ crystal, for example, is only 20 times of the MIR generation in a 100 µm thick $LiIO_3$. The simulated results are supported by experimental results, taken with a 100 µm, 500 µm and 1 mm thick crystal (Figure IX.2a).

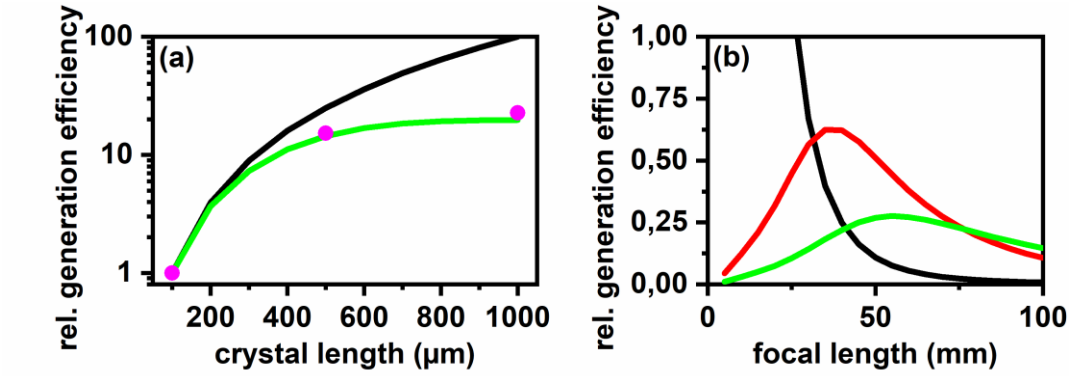

Figure IX.2 The theoretical conversion efficiency in 2nd order nonlinear processes for collinear beams is quadratic (black). In the presence of a spatial walk-off of 56 µm/mm ($LiIO_3$) and a focused Gaussian beam (f=10 cm), the conversion efficiency is reduced (green) and describes well the measurements of a narrowband MIR generation in a $LiIO_3$ crystal (purple dots). (b) In the presence of spatial walk-off, the optimal focal length, which generates in 100 µm (black), 500 µm (red) and 1000 µm (green) thick $LiIO_3$ crystals the highest MIR power, increase with the crystal thickness.

(ii) In the second case, the focal length is varied and the MIR generation is analysed on its dependence. Considerations of Boyd and Kleinman [185] take the properties of Gaussian beams into account and result in an optimum focusing well below 2 cm. This focal length is underestimated due to the missing spatial walk-off. By taking it into account, an optimal focal length of 4 cm for a 500 µm thick crystal is provided (Figure IX.2b). However, this focal length is also underestimated by taking only geometrical properties of Gaussian beams and the spatial walk-off into account. In contrast, the phase matching angle should be additionally considered, which would only be provided in extensive stochastic simulations. Instead, the optimal focal length was experimentally determined by testing the MIR generation in consideration of a 5 cm, 10 cm, 15 cm, 20 cm focal length. In the experimental benchmarking, the NIR pulses are focused inside the 100 µm thick crystal and the generated MIR light is detected. A parabolic mirror with f=10 cm is in agreement with literature [102, 186, 187].

4. First demonstration of an external local oscillator in the heterodyne multiplex method

An external local oscillator enhances the signal in the heterodyne SF spectroscopy method. The presented SF microscopy setup indicates a simple way to implement an external local oscillator (see Figure VIII.1a). This is accomplished by exploiting the unused blue part of the NIR spectrum as an external local oscillator after reducing its intensity. In a first test, the SF signal is generated in crystalline cholesterol and enhanced by the local oscillator. The dependence of the detected signal on the local oscillator is tested by varying its phase (i) and intensity (ii).

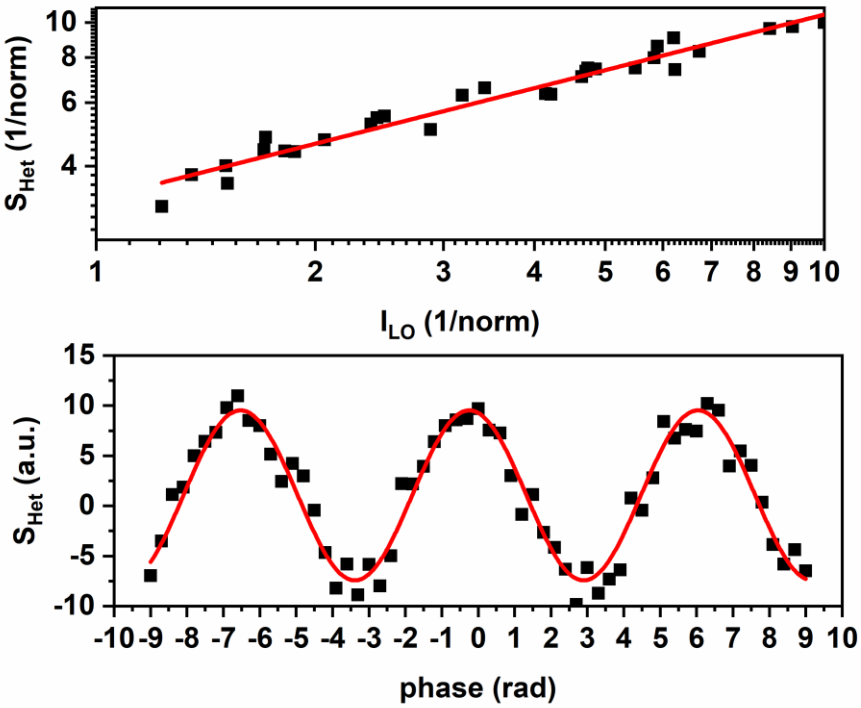

Figure IX.3 The principle of an external local oscillator is demonstrated by varying its amplification (upper) and phase (lower). In accordance to eq. VI.5, the heterodyne signal S_{Het} is enhanced or supressed. The measured date (black) agrees well with the theoretical expectations (red).

(i) The phase is varied by the imprinting an additional phase on the small phase gate via the pulse shaper (Figure IX.3b). This variation can be well described by a cosine-function.

(ii) The amplification factor is also controlled by varying the intensity of the local oscillator. It shows the expected square-root dependence and is fitted well by a linear function (slope $0{,}51 \pm 0{,}01$) in the log-log scale (Figure IX.3b).

5. Appendix of the MIR phase retrieval

5 i. Conversion efficiency of SF process

The 100 µm $LiIO_3$ crystal has a broad collinear phase matching in the MIR as shown in section IV.3. However, the situation is different by using the LiO_3 crystal inside microscope due to the broad aperture angle. Therefore, a constant conversion efficiency is not a priori provided. Since a wavelength-independent SF generation is essential for the determination of the MIR phase directly in the microscope (see section VII), an experimental test is performed. In this purpose, the SF spectrum is obtained by inserting a $LiIO_3$ crystal in the microscope and exploiting the homodyne MIR-scanning method. This SF spectrum is compared with the MIR spectrum detected in the MIR directly.

The MIR and SF spectra agree well to each other over a broad spectral range (Figure IX.2). However, a small deviation at the edge of the spectrum can be observed. By varying the temporal overlap of the NIR and MIR pulses, these deviations vanish either at the low or high frequency edge and exclude an impact of the phase matching. It is important to note, that the temporal overlap is considered in the d-scan fit and does not reduce the quality of the fit.

5 ii. NIR phase retrieval of broadband NIR spectra

The phase of the NIR pulses is determined without any impact of spectral filtering. In accordance, the 20 µm thick BBO crystal is inserted directly behind the MIR generation and the shaper-based NIR d-scan method is used to retrieve the phase of the broadband NIR pulses. This phase shows a constant phase over the broad NIR spectrum as well as a phase

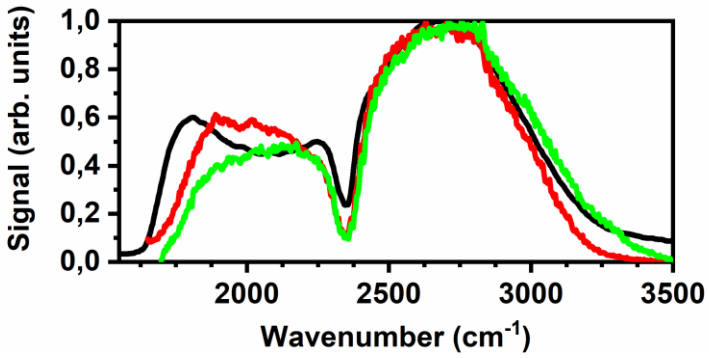

Figure IX.4 The MIR (black) and SF spectrum (coloured) are obtained by the narrowband, tuneable MIR light source via the concept of spectral focusing. The MIR spectrum is detected directly in the MIR and the SF spectra, which differ slightly due to the temporal overlap of the NIR and MIR pulses, are generated in the $LiIO_3$ crystal located in the microscope. Both spectra agree with each other and prove a constant conversion efficiency.

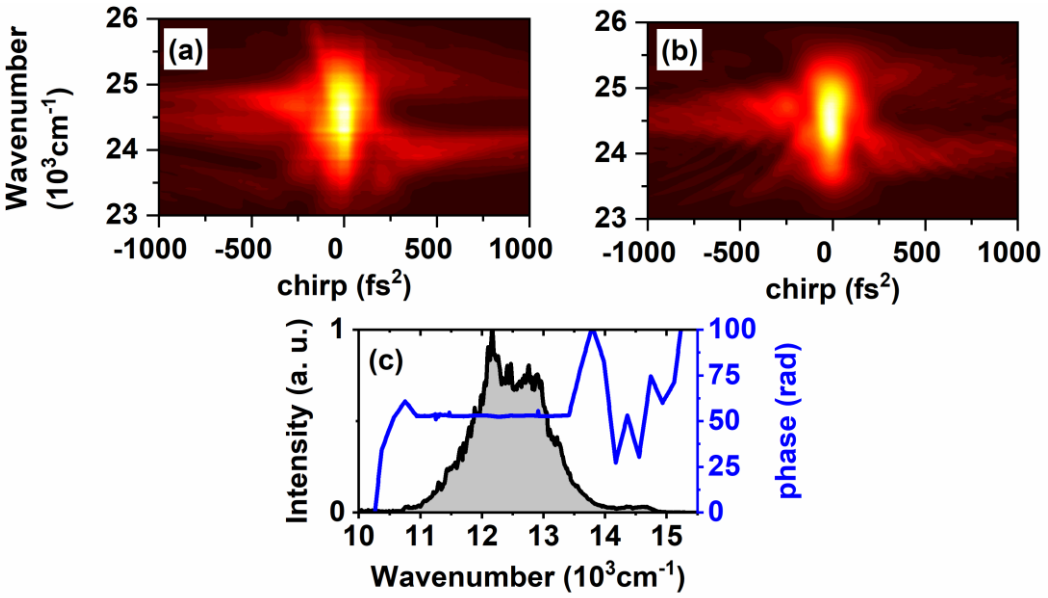

Figure IX.5 Experimental MIR phase retrieval of an ultrabroadband NIR pulse: (a&b) Measured (a) and fitted (b) d-scan trace; (c) NIR spectrum (grey background) and retrieved spectral phase (blue).

variation at the edge of the spectrum (14000 cm^{-1}), which has been already discussed (see section VII.5)

5 iii. Phase-sensitive MIR spectroscopy

The MIR phase retrieval also provides the potential to determine the phase of vibrational modes. This is demonstrated on a polystyrene film. In accordance, the phases of MIR pulses are determined via a global fit of the Xd-scan and dual d-scan traces. These phases are determined for two different considerations. A reference phase is obtained in a first d-scan without any additional substrate and in a second scan the phase of the MIR pulse is

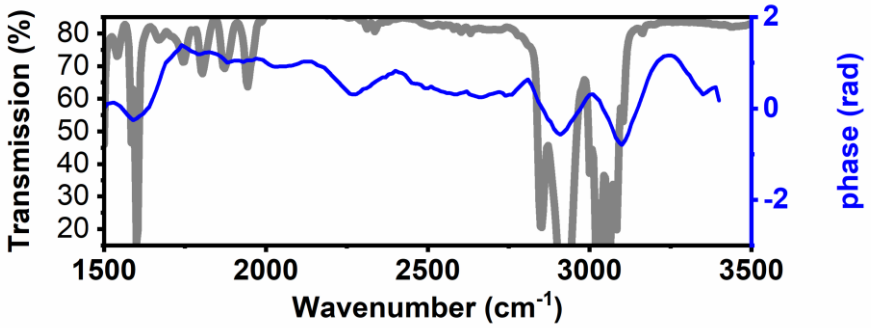

Figure IX.6 Demonstration of the phase sensitivity of the d-scan method by detecting the vibrational modes of a polystyrene film. The film is inserted in the NIR beam path and the fitted phase (blue) is obtained like in Figure VII.9. It shows the same vibrational modes as the absorption (grey).

determined with the polystyrene film in the beam path. After subtracting the reference, the latter phase indicates the phase of the vibrational modes. As depicted in Figure IX.6, this phase shows the same vibrational modes as the MIR absorption spectrum.

List of publications

Parts of this work have been published or prepared in the following references:

- Lukas Brückner, Niklas Müller, and Marcus Motzkus,
  "Flexible and broadly tunable infrared light source based on shaped sub-10-fs pulses for a multimodal microscopy setup"
  Opt. Lett. **43**, 2054-2057 (2018)
- Niklas Müller, Lukas Brückner, and Marcus Motzkus,
  “Invited Article: Coherent Raman and mid-IR microscopy using shaped pulses in a single-beam setup”
  APL Photonics **3**(9) 092406 (2018)
- Niklas Müller, Lukas Brückner, and Marcus Motzkus
  “Shaper-based infrared spectroscopy in a nonlinear Raman setup”
  EPJ Web Conf. 205 03016 (2019)
- Niklas Müller, Tiago Buckup, and Marcus Motzkus,
  "Flexible pulse shaping for sum frequency microspectroscopies,"
  J. Opt. Soc. Am. B **37**, 117-126 (2020)
- Niklas Müller, and Tiago Buckup “Broadband mid-infrared phase reconstruction in the focal plane of a microscope”
  In preparation

References

1. N. Müller, L. Brückner, and M. Motzkus, "Invited Article: Coherent Raman and mid-IR microscopy using shaped pulses in a single-beam setup," APL Photonics, 2018. **3**(9): p. 092406.
2. N. Müller, T. Buckup, and M. Motzkus, "Flexible pulse shaping for sum frequency microspectroscopies," Journal of the Optical Society of America B, 2020. **37**(1): p. 117-126.
3. L. Brückner, N. Müller, and M. Motzkus, "Flexible and broadly tunable infrared light source based on shaped sub-10-fs pulses for a multimodal microscopy setup," Optics Letters, 2018. **43**(9): p. 2054-2057.
4. B. Huang, M. Bates, and X. Zhuang, "Super-Resolution Fluorescence Microscopy," Annual Review of Biochemistry, 2009. **78**(1): p. 993-1016.
5. S.W. Hell, "Far-Field Optical Nanoscopy," Science, 2007. **316**(5828): p. 1153.
6. M.J. Rust, M. Bates, and X. Zhuang, "Sub-diffraction-limit imaging by stochastic optical reconstruction microscopy (STORM)," Nature methods, 2006. **3**(10): p. 793-795.
7. F. Balzarotti, Y. Eilers, K.C. Gwosch, A.H. Gynnå, V. Westphal, F.D. Stefani, J. Elf, and S.W. Hell, "Nanometer resolution imaging and tracking of fluorescent molecules with minimal photon fluxes," Science, 2017. **355**(6325): p. 606.
8. M. Hesse, H. Meier, and B. Zeeh, "Spektroskopische Methoden in der organischen Chemie." 2005: Thieme.
9. P.J. Larkin, "IR and Raman: principles in spectral interpretations." 2012, Elservier: Elservier.
10. N. Gierlinger and M. Schwanninger, "Chemical Imaging of Poplar Wood Cell Walls by Confocal Raman Microscopy," Plant Physiology, 2006. **140**(4): p. 1246.
11. H. Keisaku, F. Katsumasa, S. Nicholas Isaac, K. Minoru, I. Yasushi, and K. Satoshi, "Raman microscopy for dynamic molecular imaging of living cells," Journal of Biomedical Optics, 2008. **13**(4): p. 1-4.
12. G.D. Smith and R.J.H. Clark, "Raman microscopy in archaeological science," Journal of Archaeological Science, 2004. **31**(8): p. 1137-1160.
13. S. Prati, E. Joseph, G. Sciutto, and R. Mazzeo, "New Advances in the Application of FTIR Microscopy and Spectroscopy for the Characterization of Artistic Materials," Accounts of Chemical Research, 2010. **43**(6): p. 792-801.
14. P. Bassan, M.J. Weida, J. Rowlette, and P. Gardner, "Large scale infrared imaging of tissue micro arrays (TMAs) using a tunable Quantum Cascade Laser (QCL) based microscope," Analyst, 2014. **139**(16): p. 3856-3859.
15. N. Kröger-Lui, N. Gretz, K. Haase, B. Kränzlin, S. Neudecker, A. Pucci, A. Regenscheit, A. Schönhals, and W. Petrich, "Rapid identification of goblet cells in unstained colon thin sections by means of quantum cascade laser-based infrared microspectroscopy," Analyst, 2015. **140**(7): p. 2086-2092.
16. P.D. Maker and R.W. Terhune, "Study of Optical Effects Due to an Induced Polarization Third Order in the Electric Field Strength," Physical Review, 1965. **137**(3A): p. A801-A818.
17. C.L. Evans and X.S. Xie, "Coherent Anti-Stokes Raman Scattering Microscopy: Chemical Imaging for Biology and Medicine," Annual Review of Analytical Chemistry, 2008. **1**(1): p. 883-909.

18. C.L. Evans, E.O. Potma, M. Puoris'haag, D. Côté, C.P. Lin, and X.S. Xie, "Chemical imaging of tissue in vivo with video-rate coherent anti-Stokes Raman scattering microscopy," Proceedings of the National Academy of Sciences of the United States of America, 2005. **102**(46): p. 16807.
19. A. Zumbusch, G.R. Holtom, and X.S. Xie, "Three-Dimensional Vibrational Imaging by Coherent Anti-Stokes Raman Scattering," Physical Review Letters, 1999. **82**(20): p. 4142-4145.
20. S. Yue, M.N. Slipchenko, and J.X. Cheng, "Multimodal nonlinear optical microscopy," Laser & Photonics Reviews, 2011. **5**(4): p. 496-512.
21. I. Pope, W. Langbein, P. Watson, and P. Borri, "Simultaneous hyperspectral differential-CARS, TPF and SHG microscopy with a single 5 fs Ti:Sa laser," Optics Express, 2013. **21**(6): p. 7096-7106.
22. K. König, H.G. Breunig, A. Batista, A. Schindele, M. Zieger, and M. Kaatz, "Translation of two-photon microscopy to the clinic: multimodal multiphoton CARS tomography of in vivo human skin," Journal of Biomedical Optics, 2020. **25**(1): p. 014515.
23. M.E.P. Didier, O.B. Tarun, P. Jourdain, P. Magistretti, and S. Roke, "Membrane water for probing neuronal membrane potentials and ionic fluxes at the single cell level," Nature Communications, 2018. **9**(1): p. 5287.
24. A. Lukic, S. Dochow, H. Bae, G. Matz, I. Latka, B. Messerschmidt, M. Schmitt, and J. Popp, "Endoscopic fiber probe for nonlinear spectroscopic imaging," Optica, 2017. **4**(5): p. 496-501.
25. V. Schweikhard, A. Baral, V. Krishnamachari, W.C. Hay, and M. Fuhrmann, "Label-free characterization of Amyloid-β-plaques and associated lipids in brain tissues using stimulated Raman scattering microscopy," bioRxiv, 2019: p. 789248.
26. T. Gottschall, T. Meyer, M. Baumgartl, B. Dietzek, J. Popp, J. Limpert, and A. Tünnermann, "Fiber-based optical parametric oscillator for high resolution coherent anti-Stokes Raman scattering (CARS) microscopy," Optics Express, 2014. **22**(18): p. 21921-21928.
27. L. Ebner and A. Zumbusch, "Yb fiber based laser source for tunable, narrow bandwidth picosecond pulses in the visible," Optics Letters, 2019. **44**(9): p. 2290-2293.
28. Y. Han, J. Hsu, N.-H. Ge, and E.O. Potma, "Polarization-Sensitive Sum-Frequency Generation Microscopy of Collagen Fibers," The Journal of Physical Chemistry B, 2015. **119**(8): p. 3356-3365.
29. M. Brinkmann, A. Fast, T. Hellwig, I. Pence, C.L. Evans, and C. Fallnich, "Portable all-fiber dual-output widely tunable light source for coherent Raman imaging," Biomedical Optics Express, 2019. **10**(9): p. 4437-4449.
30. N. Dudovich, D. Oron, and Y. Silberberg, "Single-pulse coherently controlled nonlinear Raman spectroscopy and microscopy," Nature, 2002. **418**(6897): p. 512-514.
31. D. Oron, N. Dudovich, and Y. Silberberg, "Femtosecond Phase-and-Polarization Control for Background-Free Coherent Anti-Stokes Raman Spectroscopy," Physical Review Letters, 2003. **90**(21): p. 213902.
32. D. Zeidler, S. Frey, W. Wohlleben, M. Motzkus, F. Busch, T. Chen, W. Kiefer, and A. Materny, "Optimal control of ground-state dynamics in polymers," The Journal of Chemical Physics, 2002. **116**(12): p. 5231-5235.
33. B. von Vacano, T. Buckup, and M. Motzkus, "Highly sensitive single-beam heterodyne coherent anti-Stokes Raman scattering," Optics Letters, 2006. **31**(16): p. 2495-2497.
34. A. Wipfler, J. Rehbinder, T. Buckup, and M. Motzkus, "Full characterization of the third-order nonlinear susceptibility using a single-beam coherent anti-Stokes Raman scattering setup," Optics Letters, 2012. **37**(20): p. 4239-4241.

35. L. Brückner, T. Buckup, and M. Motzkus, "Exploring the potential of tailored spectral focusing," Journal of the Optical Society of America B, 2016. **33**(7): p. 1482-1491.
36. B. von Vacano and M. Motzkus, "Time-resolved two color single-beam CARS employing supercontinuum and femtosecond pulse shaping," Optics Communications, 2006. **264**(2): p. 488-493.
37. A. Wipfler, T. Buckup, and M. Motzkus, "Multiplexing single-beam coherent anti-stokes Raman spectroscopy with heterodyne detection," Applied Physics Letters, 2012. **100**(7): p. 071102.
38. L.J. Richter, T.P. Petralli-Mallow, and J.C. Stephenson, "Vibrationally resolved sum-frequency generation with broad-bandwidth infrared pulses," Optics Letters, 1998. **23**(20): p. 1594-1596.
39. X. Su, L. Lianos, Y.R. Shen, and G.A. Somorjai, "Surface-Induced Ferroelectric Ice on Pt(111)," Physical Review Letters, 1998. **80**(7): p. 1533-1536.
40. Y.R. Shen, "Surfaces probed by nonlinear optics," Surface Science, 1994. **299-300**: p. 551-562.
41. W. Sung, D. Kim, and Y.R. Shen, "Sum-frequency vibrational spectroscopic studies of Langmuir monolayers," Current Applied Physics, 2013. **13**(4): p. 619-632.
42. C.M. Lee, K. Kafle, S. Huang, and S.H. Kim, "Multimodal Broadband Vibrational Sum Frequency Generation (MM-BB-V-SFG) Spectrometer and Microscope," The Journal of Physical Chemistry B, 2016. **120**(1): p. 102-116.
43. A. Hanninen, M.W. Shu, and E.O. Potma, "Hyperspectral imaging with laser-scanning sum-frequency generation microscopy," Biomedical Optics Express, 2017. **8**(9): p. 4230-4242.
44. D. Zheng, L. Lu, Y. Li, K.F. Kelly, and S. Baldelli, "Compressive Broad-Band Hyperspectral Sum Frequency Generation Microscopy to Study Functionalized Surfaces," The Journal of Physical Chemistry Letters, 2016. **7**(10): p. 1781-1787.
45. M. Flörsheimer, C. Brillert, and H. Fuchs, "Chemical Imaging of Interfaces by Sum Frequency Microscopy," Langmuir, 1999. **15**(17): p. 5437-5439.
46. M. Miranda, T. Fordell, C. Arnold, A. L'Huillier, and H. Crespo, "Simultaneous compression and characterization of ultrashort laser pulses using chirped mirrors and glass wedges," Optics Express, 2012. **20**(1): p. 688-697.
47. B. Weigelin, G.-J. Bakker, and P. Friedl, "Third harmonic generation microscopy of cells and tissue organization," Journal of Cell Science, 2016. **129**(2): p. 245.
48. G. Cox, "Biological applications of second harmonic imaging," Biophysical Reviews, 2011. **3**(3): p. 131.
49. G. Steinmeyer, D.H. Sutter, L. Gallmann, N. Matuschek, and U. Keller, "Frontiers in Ultrashort Pulse Generation: Pushing the Limits in Linear and Nonlinear Optics," Science, 1999. **286**(5444): p. 1507.
50. E.A. Seddon, J.A. Clarke, D.J. Dunning, C. Masciovecchio, C.J. Milne, F. Parmigiani, D. Rugg, J.C.H. Spence, N.R. Thompson, K. Ueda, S.M. Vinko, J.S. Wark, and W. Wurth, "Short-wavelength free-electron laser sources and science: a review," Reports on Progress in Physics, 2017. **80**(11): p. 115901.
51. C. Manzoni and G. Cerullo, "Design criteria for ultrafast optical parametric amplifiers," Journal of Optics, 2016. **18**(10): p. 103501.
52. C. Gaida, M. Gebhardt, F. Stutzki, C. Jauregui, J. Limpert, and A. Tünnermann, "Thulium-doped fiber chirped-pulse amplification system with 2 GW of peak power," Optics Letters, 2016. **41**(17): p. 4130-4133.
53. C. Rulliere, "Femtoseconds Laser Pulses." Vol. second edition. 2003, Springer.
54. B.E.A. Saleh and M.C. Teich, "Fumdamentals of Photonics." Wiley Series in Pura and Applied Optics, ed. B.E.A.Saleh. 2007, Wiley.
55. A. Monmayrant, S. Weber, and B. Chatel, "A newcomer's guide to ultrashort pulse shaping and characterization," Journal of Physics B: Atomic, Molecular and Optical Physics, 2010. **43**(10): p. 103001.

56. T. Brixner, I.V. Stiopkin, and G.R. Fleming, "Tunable two-dimensional femtosecond spectroscopy," Optics Letters, 2004. **29**(8): p. 884-886.
57. J. Köhler, M. Wollenhaupt, T. Bayer, C. Sarpe, and T. Baumert, "Zeptosecond precision pulse shaping," Optics Express, 2011. **19**(12): p. 11638-11653.
58. R.W. Boyd, "Nonlinear Optics." 2008: Academic Press.
59. R.A. Kaindl, F. Eickemeyer, M. Woerner, and T. Elsaesser, "Broadband phase-matched difference frequency mixing of femtosecond pulses in GaSe: Experiment and theory," Applied Physics Letters, 1999. **75**(8): p. 1060-1062.
60. A. Wipfler, "Phd-thesis: Nichtlinear optische Mikroskopie mit geformten Femtosekundenlaserimpulses." 2014, University Heidelberg.
61. L. Ren, I. Hurwitz, D. Raanan, P. Oulevey, D. Oron, and Y. Silberberg, "Terahertz coherent anti-Stokes Raman scattering microscopy," Optica, 2019. **6**(1): p. 52-55.
62. A.F. Pegoraro, A.D. Slepkov, A. Ridsdale, D.J. Moffatt, and A. Stolow, "Hyperspectral multimodal CARS microscopy in the fingerprint region," Journal of Biophotonics, 2014. **7**(1-2): p. 49-58.
63. L. Brückner, T. Buckup, and M. Motzkus, "Enhancement of coherent anti-Stokes Raman signal via tailored probing in spectral focusing," Optics Letters, 2015. **40**(22): p. 5204-5207.
64. J.-X. Cheng and X.S. Xie, "Coherent Anti-Stokes Raman Scattering Microscopy: Instrumentation, Theory, and Applications," The Journal of Physical Chemistry B, 2004. **108**(3): p. 827-840.
65. Y. Liu, Y.J. Lee, and M.T. Cicerone, "Fast extraction of resonant vibrational response from CARS spectra with arbitrary nonresonant background," Journal of Raman Spectroscopy, 2009. **40**(7): p. 726-731.
66. E.M. Vartiainen, T. Asakura, and K.E. Peiponen, "Generalized noniterative maximum entropy procedure for phase retrieval problems in optical spectroscopy," Optics Communications, 1993. **104**(1): p. 149-156.
67. V. Kumar, R. Osellame, R. Ramponi, G. Cerullo, and M. Marangoni, "Background-free broadband CARS spectroscopy from a 1-MHz ytterbium laser," Optics Express, 2011. **19**(16): p. 15143-15148.
68. J.D. Miller, M.N. Slipchenko, and T.R. Meyer, "Probe-pulse optimization for nonresonant suppression in hybrid fs/ps coherent anti-Stokes Raman scattering at high temperature," Optics Express, 2011. **19**(14): p. 13326-13333.
69. C. Stiebing, T. Meyer, I. Rimke, C. Matthäus, M. Schmitt, S. Lorkowski, and J. Popp, "Real-time Raman and SRS imaging of living human macrophages reveals cell-to-cell heterogeneity and dynamics of lipid uptake," Journal of Biophotonics, 2017. **10**(9): p. 1217-1226.
70. J.-x. Cheng, A. Volkmer, L.D. Book, and X.S. Xie, "Multiplex Coherent Anti-Stokes Raman Scattering Microspectroscopy and Study of Lipid Vesicles," The Journal of Physical Chemistry B, 2002. **106**(34): p. 8493-8498.
71. C. Pohling, T. Buckup, A. Pagenstecher, and M. Motzkus, "Chemoselective imaging of mouse brain tissue via multiplex CARS microscopy," Biomedical Optics Express, 2011. **2**(8): p. 2110-2116.
72. G. Veitas and R. Danielius, "Generation of narrow-bandwidth tunable picosecond pulses by difference-frequency mixing of stretched pulses," Journal of the Optical Society of America B, 1999. **16**(9): p. 1561-1565.
73. T. Hellerer, A.M.K. Enejder, and A. Zumbusch, "Spectral focusing: High spectral resolution spectroscopy with broad-bandwidth laser pulses," Applied Physics Letters, 2004. **85**(1): p. 25-27.
74. W. Langbein, D. Regan, I. Pope, and P. Borri, "Invited Article: Heterodyne dual-polarization epi-detected CARS microscopy for chemical and topographic imaging of interfaces," APL Photonics, 2018. **3**(9): p. 092402.
75. W. Langbein, I. Rocha-Mendoza, and P. Borri, "Single source coherent anti-Stokes Raman microspectroscopy using spectral focusing," Applied Physics Letters, 2009. **95**(8): p. 081109.

76. L. Brückner, "PhD thesis: Exploring the Potential of Nonlinear Optical Microscopy with Tailored Femtosecond Pulses," in Chemistry Department. 2016, University of Heidelberg.
77. J. Rebinder, "Phd thesis: Quick and specific non-linear microscopy using shaped pulses with durations down to 10fs," in Chemistry Department. 2013, University of Heidelberg.
78. J. Bradley, I. Pope, F. Masia, R. Sanusi, W. Langbein, K. Swann, and P. Borri, "Quantitative imaging of lipids in live mouse oocytes and early embryos using CARS microscopy," Development, 2016. **143**(12): p. 2238.
79. B. Liu, H. Bromberger, A. Cartella, T. Gebert, M. Först, and A. Cavalleri, "Generation of narrowband, high-intensity, carrier-envelope phase-stable pulses tunable between 4 and 18THz," Optics Letters, 2017. **42**(1): p. 129-131.
80. F. Helmchen and W. Denk, "Deep tissue two-photon microscopy," Nature Methods, 2005. **2**(12): p. 932-940.
81. D.E. Spence, P.N. Kean, and W. Sibbett, "60-fsec pulse generation from a self-mode-locked Ti:sapphire laser," Optics Letters, 1991. **16**(1): p. 42-44.
82. A. Stingl, M. Lenzner, C. Spielmann, F. Krausz, and R. Szipöcs, "Sub-10-fs mirror-dispersion-controlled Ti:sapphire laser," Optics Letters, 1995. **20**(6): p. 602-604.
83. Femtolasers, "Manual: Fusion 800 Pro." 2009.
84. A. Präkelt, M. Wollenhaupt, A. Assion, C. Horn, C. Sarpe-Tudoran, M. Winter, and T. Baumert, "Compact, robust, and flexible setup for femtosecond pulse shaping," Review of Scientific Instruments, 2003. **74**(11): p. 4950-4953.
85. S. De Bruyne, M.M. Speeckaert, and J.R. Delanghe, "Applications of mid-infrared spectroscopy in the clinical laboratory setting," Critical Reviews in Clinical Laboratory Sciences, 2018. **55**(1): p. 1-20.
86. J. Haas and B. Mizaikoff, "Advances in Mid-Infrared Spectroscopy for Chemical Analysis," Annual Review of Analytical Chemistry, 2016. **9**(1): p. 45-68.
87. C. Krafft, K. Thümmler, S.B. Sobottka, G. Schackert, and R. Salzer, "Classification of malignant gliomas by infrared spectroscopy and linear discriminant analysis," Biopolymers, 2006. **82**(4): p. 301-305.
88. M. Brandstetter, A. Genner, K. Anic, and B. Lendl, "Tunable external cavity quantum cascade laser for the simultaneous determination of glucose and lactate in aqueous phase," Analyst, 2010. **135**(12): p. 3260-3265.
89. C. Vrančić, A. Fomichova, N. Gretz, C. Herrmann, S. Neudecker, A. Pucci, and W. Petrich, "Continuous glucose monitoring by means of mid-infrared transmission laser spectroscopyin vitro," Analyst, 2011. **136**(6): p. 1192-1198.
90. K. Isensee, N. Müller, A. Pucci, and W. Petrich, "Towards a quantum cascade laser-based implant for the continuous monitoring of glucose," Analyst, 2018. **143**(24): p. 6025-6036.
91. S. Primpke, C. Lorenz, R. Rascher-Friesenhausen, and G. Gerdts, "An automated approach for microplastics analysis using focal plane array (FPA) FTIR microscopy and image analysis," Analytical Methods, 2017. **9**(9): p. 1499-1511.
92. A. Käppler, D. Fischer, S. Oberbeckmann, G. Schernewski, M. Labrenz, K.-J. Eichhorn, and B. Voit, "Analysis of environmental microplastics by vibrational microspectroscopy: FTIR, Raman or both?," Analytical and Bioanalytical Chemistry, 2016. **408**(29): p. 8377-8391.
93. L. Mariey, J.P. Signolle, C. Amiel, and J. Travert, "Discrimination, classification, identification of microorganisms using FTIR spectroscopy and chemometrics," Vibrational Spectroscopy, 2001. **26**(2): p. 151-159.
94. L.B. Mostaço-Guidolin and L. Bachmann, "Application of FTIR Spectroscopy for Identification of Blood and Leukemia Biomarkers: A Review over the Past 15 Years," Applied Spectroscopy Reviews, 2011. **46**(5): p. 388-404.
95. J. Faist, F. Capasso, D.L. Sivco, C. Sirtori, A.L. Hutchinson, and A.Y. Cho, "Quantum Cascade Laser," Science, 1994. **264**(5158): p. 553.

96. F. Seifert, V. Petrov, and M. Woerner, "Solid-state laser system for the generation of midinfrared femtosecond pulses tunable from 3.3 to 10 μm," Optics Letters, 1994. **19**(23): p. 2009-2011.
97. D. Brida, C. Manzoni, G. Cirmi, M. Marangoni, S. Bonora, P. Villoresi, S. De Silvestri, and G. Cerullo, "Few-optical-cycle pulses tunable from the visible to the mid-infrared by optical parametric amplifiers," Journal of Optics, 2009. **12**(1): p. 013001.
98. C. Erny, C. Heese, M. Haag, L. Gallmann, and U. Keller, "High-repetition-rate optical parametric chirped-pulse amplifier producing 1-μJ, sub-100-fs pulses in the mid-infrared," Optics Express, 2009. **17**(3): p. 1340-1345.
99. A. Lohner, P. Kruck, and W.W. Rühle, "Generation of 200 femtosecond pulses tunable between 2.5 and 5.5 μm," Applied Physics B, 1994. **59**(2): p. 211-213.
100. J.M. Fraser, D. Wang, A. Haché, G.R. Allan, and H.M. van Driel, "Generation of high-repetition-rate femtosecond pulses from 8 to 18 μm," Applied Optics, 1997. **36**(21): p. 5044-5047.
101. M.R.X. de Barros, R.S. Miranda, T.M. Jedju, and P.C. Becker, "High-repetition-rate femtosecond mid-infrared pulse generation," Optics Letters, 1995. **20**(5): p. 480-482.
102. T. Zentgraf, R. Huber, N.C. Nielsen, D.S. Chemla, and R.A. Kaindl, "Ultrabroadband 50-130 THz pulses generated via phase-matched difference frequency mixing in LiIO3," Optics Express, 2007. **15**(9): p. 5775-5781.
103. K.L. Vodopyanov, "Mid-infrared optical parametric generator with extra-wide (3–19-μm) tunability: applications for spectroscopy of two-dimensional electrons in quantum wells," Journal of the Optical Society of America B, 1999. **16**(9): p. 1579-1586.
104. V. Petrov, F. Rotermund, and F. Noack, "Generation of high-power femtosecond light pulses at 1 kHz in the mid-infrared spectral range between 3 and 12 μm by second-order nonlinear processes in optical crystals," Journal of Optics A: Pure and Applied Optics, 2001. **3**(3): p. R1-R19.
105. A. Zheltikov, "Springer Handbook of Laser and Optics," F. Träger, Editor. 2012, Springer: Heidelberg.
106. M.M. Choy and R.L. Byer, "Accurate second-order susceptibility measurements of visible and infrared nonlinear crystals," Physical Review B, 1976. **14**(4): p. 1693-1706.
107. Eksma-Optics, " Information of crystal manufacturer." 2016.
108. D. Gerz, "Master thesis: Shaping and characterization of tunable few-optical-cycle mid-infrared pulses," in Phyics Department. 2017, University of Heidelberg.
109. E. Hendrickson, E.C. Minor, and K. Schreiner, "Microplastic Abundance and Composition in Western Lake Superior As Determined via Microscopy, Pyr-GC/MS, and FTIR," Environmental Science & Technology, 2018. **52**(4): p. 1787-1796.
110. Z. Movasaghi, S. Rehman, and D.I. ur Rehman, "Fourier Transform Infrared (FTIR) Spectroscopy of Biological Tissues," Applied Spectroscopy Reviews, 2008. **43**(2): p. 134-179.
111. K. Hashimoto, V.R. Badarla, A. Kawai, and T. Ideguchi, "Complementary vibrational spectroscopy," Nature Communications, 2019. **10**(1): p. 4411.
112. M. Joffre, A. Bonvalet, A. Migus, and J.L. Martin, "Femtosecond diffracting Fourier-transform infrared interferometer," Optics Letters, 1996. **21**(13): p. 964-966.
113. N. Pavillon, K. Fujita, and N. Isaac Smith, "Multimodal label-free microscopy," Journal of Innovative Optical Health Sciences, 2013. **07**(05): p. 1330009.
114. C.L. Evans, X. Xu, S. Kesari, X.S. Xie, S.T.C. Wong, and G.S. Young, "Chemically-selective imaging of brain structures with CARS microscopy," Optics Express, 2007. **15**(19): p. 12076-12087.

115. F. Ganikhanov, C.L. Evans, B.G. Saar, and X.S. Xie, "High-sensitivity vibrational imaging with frequency modulation coherent anti-Stokes Raman scattering (FM CARS) microscopy," Optics Letters, 2006. **31**(12): p. 1872-1874.
116. C. Brackmann, A. Bengtsson, M.L. Alminger, U. Svanberg, and A. Enejder, "Visualization of β-carotene and starch granules in plant cells using CARS and SHG microscopy," Journal of Raman Spectroscopy, 2011. **42**(4): p. 586-592.
117. R. Galli, O. Uckermann, E.F. Andresen, K.D. Geiger, E. Koch, G. Schackert, G. Steiner, and M. Kirsch, "Intrinsic Indicator of Photodamage during Label-Free Multiphoton Microscopy of Cells and Tissues," PLOS ONE, 2014. **9**(10): p. e110295.
118. D.S. Hall, D.J. Lockwood, S. Poirier, C. Bock, and B.R. MacDougall, "Raman and Infrared Spectroscopy of α and β Phases of Thin Nickel Hydroxide Films Electrochemically Formed on Nickel," The Journal of Physical Chemistry A, 2012. **116**(25): p. 6771-6784.
119. X. Lu, H.M. Al-Qadiri, M. Lin, and B.A. Rasco, "Application of Mid-infrared and Raman Spectroscopy to the Study of Bacteria," Food and Bioprocess Technology, 2011. **4**(6): p. 919-935.
120. Y.-S. Li, J.S. Church, and A.L. Woodhead, "Infrared and Raman spectroscopic studies on iron oxide magnetic nano-particles and their surface modifications," Journal of Magnetism and Magnetic Materials, 2012. **324**(8): p. 1543-1550.
121. M. Szymańska-Chargot, J. Cybulska, and A. Zdunek, "Sensing the Structural Differences in Cellulose from Apple and Bacterial Cell Wall Materials by Raman and FT-IR Spectroscopy," Sensors, 2011. **11**(6).
122. C. Pohling, "PhD thesis: Multiplex-CARS-Mikroskopie zur schnellen und Raman-äquivalenten Charakterisierung biologischer Proben." 2012, University Heidelberg.
123. P. Garidel and H. Schott, "Fourier-Transform Midinfrared Spectroscopy for Analysis and Screening of Liquid Protein Formulations Part 2 : Detailed Analysis and Applications," 2006.
124. K. Belbachir, R. Noreen, G. Gouspillou, and C. Petibois, "Collagen types analysis and differentiation by FTIR spectroscopy," Analytical and Bioanalytical Chemistry, 2009. **395**(3): p. 829-837.
125. R. Lüllmann-Rauch, "Taschenbuch Histologie," 3 ed. 2006, Thieme.
126. T. Wilson, "Resolution and optical sectioning in the confocal microscope," Journal of Microscopy, 2011. **244**(2): p. 113-121.
127. G. Cox and C.J.R. Sheppard, "Practical limits of resolution in confocal and non-linear microscopy," Microscopy Research and Technique, 2004. **63**(1): p. 18-22.
128. J. Squier and M. Müller, "High resolution nonlinear microscopy: A review of sources and methods for achieving optimal imaging," Review of Scientific Instruments, 2001. **72**(7): p. 2855-2867.
129. F. Crisafi, V. Kumar, A. Perri, M. Marangoni, G. Cerullo, and D. Polli, "Multimodal nonlinear microscope based on a compact fiber-format laser source," Spectrochimica Acta Part A: Molecular and Biomolecular Spectroscopy, 2018. **188**: p. 135-140.
130. M. Cicerone, "Molecular imaging with CARS micro-spectroscopy," Current Opinion in Chemical Biology, 2016. **33**: p. 179-185.
131. I. Rocha-Mendoza, D.R. Yankelevich, M. Wang, K.M. Reiser, C.W. Frank, and A. Knoesen, "Sum Frequency Vibrational Spectroscopy: The Molecular Origins of the Optical Second-Order Nonlinearity of Collagen," Biophysical Journal, 2007. **93**(12): p. 4433-4444.
132. H.C. Hieu, N.A. Tuan, H. Li, Y. Miyauchi, and G. Mizutani, "Sum Frequency Generation Microscopy Study of Cellulose Fibers," Applied Spectroscopy, 2011. **65**(11): p. 1254-1259.
133. X.D. Zhu, H. Suhr, and Y.R. Shen, "Surface vibrational spectroscopy by infrared-visible sum frequency generation," Physical Review B, 1987. **35**(6): p. 3047-3050.

134. K. Locharoenrat, H. Sano, and G. Mizutani, "Demonstration of confocal sum frequency microscopy," physica status solidi c, 2009. **6**(1): p. 304-306.
135. V. Raghunathan, Y. Han, O. Korth, N.-H. Ge, and E.O. Potma, "Rapid vibrational imaging with sum frequency generation microscopy," Optics Letters, 2011. **36**(19): p. 3891-3893.
136. H. Segawa, Y. Kaji, P. Leproux, V. Couderc, T. Ozawa, T. Oshika, and H. Kano, "Multimodal and multiplex spectral imaging of rat cornea ex vivo using a white-light laser source," Journal of Biophotonics, 2015. **8**(9): p. 705-713.
137. L. Zhang, Z. Lu, L. Velarde, L. Fu, Y. Pu, S.-Y. Ding, A.J. Ragauskas, H.-F. Wang, and B. Yang, "Vibrational spectral signatures of crystalline cellulose using high resolution broadband sum frequency generation vibrational spectroscopy (HR-BB-SFG-VS)," Cellulose, 2015. **22**(3): p. 1469-1484.
138. C.M. Lee, K. Kafle, Y.B. Park, and S.H. Kim, "Probing crystal structure and mesoscale assembly of cellulose microfibrils in plant cell walls, tunicate tests, and bacterial films using vibrational Sum Frequency Generation (SFG) spectroscopy," Physical Chemistry Chemical Physics, 2014. **16**(22): p. 10844-10853.
139. X. Wei, P.B. Miranda, C. Zhang, and Y.R. Shen, "Sum-frequency spectroscopic studies of ice interfaces," Physical Review B, 2002. **66**(8): p. 085401.
140. N. Ji, V. Ostroverkhov, C.-Y. Chen, and Y.-R. Shen, "Phase-Sensitive Sum-Frequency Vibrational Spectroscopy and Its Application to Studies of Interfacial Alkyl Chains," Journal of the American Chemical Society, 2007. **129**(33): p. 10056-10057.
141. P.B. Miranda and Y.R. Shen, "Liquid Interfaces: A Study by Sum-Frequency Vibrational Spectroscopy," The Journal of Physical Chemistry B, 1999. **103**(17): p. 3292-3307.
142. L. Lepetit, G. Chériaux, and M. Joffre, "Linear techniques of phase measurement by femtosecond spectral interferometry for applications in spectroscopy," Journal of the Optical Society of America B, 1995. **12**(12): p. 2467-2474.
143. B. Li, W.S. Warren, and M.C. Fischer, "Phase-cycling coherent anti-Stokes Raman scattering using shaped femtosecond laser pulses," Optics Express, 2010. **18**(25): p. 25825-25832.
144. H. Wang, T. Gao, and W. Xiong, "Self-Phase-Stabilized Heterodyne Vibrational Sum Frequency Generation Microscopy," ACS Photonics, 2017. **4**(7): p. 1839-1845.
145. S. Nihonyanagi, S. Yamaguchi, and T. Tahara, "Direct evidence for orientational flip-flop of water molecules at charged interfaces: A heterodyne-detected vibrational sum frequency generation study," The Journal of Chemical Physics, 2009. **130**(20): p. 204704.
146. A.D. Curtis, S.R. Burt, A.R. Calchera, and J.E. Patterson, "Limitations in the Analysis of Vibrational Sum-Frequency Spectra Arising from the Nonresonant Contribution," The Journal of Physical Chemistry C, 2011. **115**(23): p. 11550-11559.
147. M. Jurna, J.P. Korterik, C. Otto, and H.L. Offerhaus, "Shot noise limited heterodyne detection of CARS signals," Optics Express, 2007. **15**(23): p. 15207-15213.
148. Y.R. Shen, "Phase-Sensitive Sum-Frequency Spectroscopy," Annual Review of Physical Chemistry, 2013. **64**(1): p. 129-150.
149. H.-F. Wang, L. Velarde, W. Gan, and L. Fu, "Quantitative Sum-Frequency Generation Vibrational Spectroscopy of Molecular Surfaces and Interfaces: Lineshape, Polarization, and Orientation," Annual Review of Physical Chemistry, 2015. **66**(1): p. 189-216.
150. L. Velarde, X.-y. Zhang, Z. Lu, A.G. Joly, Z. Wang, and H.-f. Wang, "Communication: Spectroscopic phase and lineshapes in high-resolution broadband sum frequency vibrational spectroscopy: Resolving interfacial inhomogeneities of “identical” molecular groups," The Journal of Chemical Physics, 2011. **135**(24): p. 241102.

151. A.D. Curtis, M.C. Asplund, and J.E. Patterson, "Use of Variable Time-Delay Sum-Frequency Generation for Improved Spectroscopic Analysis," The Journal of Physical Chemistry C, 2011. **115**(39): p. 19303-19310.
152. I.V. Stiopkin, H.D. Jayathilake, C. Weeraman, and A.V. Benderskii, "Temporal effects on spectroscopic line shapes, resolution, and sensitivity of the broad-band sum frequency generation," The Journal of Chemical Physics, 2010. **132**(23): p. 234503.
153. J. Knorr, P. Rudolf, and P. Nuernberger, "A comparative study on chirped-pulse upconversion and direct multichannel MCT detection," Optics Express, 2013. **21**(25): p. 30693-30706.
154. M.J. Nee, R. McCanne, K.J. Kubarych, and M. Joffre, "Two-dimensional infrared spectroscopy detected by chirped pulse upconversion," Optics Letters, 2007. **32**(6): p. 713-715.
155. J. Zhu, T. Mathes, A.D. Stahl, J.T.M. Kennis, and M.L. Groot, "Ultrafast mid-infrared spectroscopy by chirped pulse upconversion in 1800-1000cm−1 region," Optics Express, 2012. **20**(10): p. 10562-10571.
156. Y.-P. Tseng, C. Pedersen, and P. Tidemand-Lichtenberg, "Upconversion detection of long-wave infrared radiation from a quantum cascade laser," Optical Materials Express, 2018. **8**(5): p. 1313-1321.
157. D. Oron, N. Dudovich, D. Yelin, and Y. Silberberg, "Narrow-Band Coherent Anti-Stokes Raman Signals from Broad-Band Pulses," Physical Review Letters, 2002. **88**(6): p. 063004.
158. V.V. Lozovoy, I. Pastirk, and M. Dantus, "Multiphoton intrapulse interference. IV. Ultrashort laser pulse spectral phase characterization and compensation," Optics Letters, 2004. **29**(7): p. 775-777.
159. D.J. Kane and R. Trebino, "Characterization of arbitrary femtosecond pulses using frequency-resolved optical gating," IEEE Journal of Quantum Electronics, 1993. **29**(2): p. 571-579.
160. T. Witte, D. Zeidler, D. Proch, K.L. Kompa, and M. Motzkus, "Programmable amplitude- and phase-modulated femtosecond laser pulses in the mid-infrared," Optics Letters, 2002. **27**(2): p. 131-133.
161. B.A. Richman, M.A. Krumbügel, and R. Trebino, "Temporal characterization of mid-IR free-electron-laser pulses by frequency-resolved optical gating," Optics Letters, 1997. **22**(10): p. 721-723.
162. G. Taft, A. Rundquist, M.M. Murnane, I.P. Christov, H.C. Kapteyn, K.W. DeLong, D.N. Fittinghoff, M.A. Krumbugel, J.N. Sweetser, and R. Trebino, "Measurement of 10-fs laser pulses," IEEE Journal of Selected Topics in Quantum Electronics, 1996. **2**(3): p. 575-585.
163. T.S. Clement, A.J. Taylor, and D.J. Kane, "Single-shot measurement of the amplitude and phase of ultrashort laser pulses in the violet," Optics Letters, 1995. **20**(1): p. 70-72.
164. T. Nagy and P. Simon, "Single-shot TG FROG for the characterization of ultrashort DUV pulses," Optics Express, 2009. **17**(10): p. 8144-8151.
165. M. Miranda, C.L. Arnold, T. Fordell, F. Silva, B. Alonso, R. Weigand, A. L'Huillier, and H. Crespo, "Characterization of broadband few-cycle laser pulses with the d-scan technique," Optics Express, 2012. **20**(17): p. 18732-18743.
166. M. Canhota, F. Silva, R. Weigand, and H.M. Crespo, "Inline self-diffraction dispersion-scan of over octave-spanning pulses in the single-cycle regime," Optics Letters, 2017. **42**(15): p. 3048-3051.
167. B. Alonso, Í.J. Sola, and H. Crespo, "Self-calibrating d-scan: measuring ultrashort laser pulses on-target using an arbitrary pulse compressor," Scientific Reports, 2018. **8**(1): p. 3264.
168. J.A. Nelder and R. Mead, "A Simplex Method for Function Minimization," The Computer Journal, 1965. **7**(4): p. 308-313.

169. E. Escoto, A. Tajalli, T. Nagy, and G. Steinmeyer, "Advanced phase retrieval for dispersion scan: a comparative study," Journal of the Optical Society of America B, 2018. **35**(1): p. 8-19.
170. H.H. Li, "Refractive index of alkaline earth halides and its wavelength and temperature derivatives," Journal of Physical and Chemical Reference Data, 1980. **9**(1): p. 161-290.
171. S. Kleinert, A. Tajalli, T. Nagy, and U. Morgner, "Rapid phase retrieval of ultrashort pulses from dispersion scan traces using deep neural networks," Optics Letters, 2019. **44**(4): p. 979-982.
172. N.C. Geib, M. Zilk, T. Pertsch, and F. Eilenberger, "Common pulse retrieval algorithm: a fast and universal method to retrieve ultrashort pulses," Optica, 2019. **6**(4): p. 495-505.
173. M. Miranda, J. Penedones, C. Guo, A. Harth, M. Louisy, L. Neoričić, A. L'Huillier, and C.L. Arnold, "Fast iterative retrieval algorithm for ultrashort pulse characterization using dispersion scans," Journal of the Optical Society of America B, 2017. **34**(1): p. 190-197.
174. D. Strickland and G. Mourou, "Compression of amplified chirped optical pulses," Optics Communications, 1985. **56**(3): p. 219-221.
175. P.P. Roy, Y. Kato, R. Abe-Yoshizumi, E. Pieri, N. Ferré, H. Kandori, and T. Buckup, "Mapping the ultrafast vibrational dynamics of all-trans and 13-cis retinal isomerization in Anabaena Sensory Rhodopsin," Physical Chemistry Chemical Physics, 2018. **20**(48): p. 30159-30173.
176. N. Wollscheid, J.L. Pérez Lustres, O. Kefer, S. Hahn, V. Brosius, U.H.F. Bunz, M. Motzkus, and T. Buckup, "Oxygen-catalysed sequential singlet fission," Nature Communications, 2019. **10**(1): p. 5202.
177. D. Pestov, V.V. Lozovoy, and M. Dantus, "Multiple Independent Comb Shaping (MICS): Phase-only generation of optical pulse sequences," Optics Express, 2009. **17**(16): p. 14351-14361.
178. S. Winnerl, F. Göttfert, M. Mittendorff, H. Schneider, M. Helm, T. Winzer, E. Malic, A. Knorr, M. Orlita, M. Potemski, M. Sprinkle, C. Berger, and W.A. de Heer, "Time-resolved spectroscopy on epitaxial graphene in the infrared spectral range: relaxation dynamics and saturation behavior," Journal of Physics: Condensed Matter, 2013. **25**(5): p. 054202.
179. M. Wagner, *et al.*, "Ultrafast and Nanoscale Plasmonic Phenomena in Exfoliated Graphene Revealed by Infrared Pump–Probe Nanoscopy," Nano Letters, 2014. **14**(2): p. 894-900.
180. P. Guo, R.D. Schaller, J.B. Ketterson, and R.P.H. Chang, "Ultrafast switching of tunable infrared plasmons in indium tin oxide nanorod arrays with large absolute amplitude," Nature Photonics, 2016. **10**(4): p. 267-273.
181. J.P. Kraack and T. Buckup, "Introduction to State-of-the-Art Multidimensional Time-Resolved Spectroscopy Methods," in Multidimensional Time-Resolved Spectroscopy, T. Buckup and J. Léonard, Editors. 2019, Springer International Publishing: Cham. p. 1-25.
182. S.-H. Shim and M.T. Zanni, "How to turn your pump–probe instrument into a multidimensional spectrometer: 2D IR and Vis spectroscopiesvia pulse shaping," Physical Chemistry Chemical Physics, 2009. **11**(5): p. 748-761.
183. X. Lin, Y. Rivenson, N.T. Yardimci, M. Veli, Y. Luo, M. Jarrahi, and A. Ozcan, "All-optical machine learning using diffractive deep neural networks," Science, 2018. **361**(6406): p. 1004.
184. T. Zahavy, A. Dikopoltsev, D. Moss, G.I. Haham, O. Cohen, S. Mannor, and M. Segev, "Deep learning reconstruction of ultrashort pulses," Optica, 2018. **5**(5): p. 666-673.
185. G.D. Boyd and D.A. Kleinman, "Parametric Interaction of Focused Gaussian Light Beams," Journal of Applied Physics, 1968. **39**(8): p. 3597-3639.

186. R.A. Kaindl, D.C. Smith, M. Joschko, M.P. Hasselbeck, M. Woerner, and T. Elsaesser, "Femtosecond infrared pulses tunable from 9 to 18 μm at an 88-MHz repetition rate," Optics Letters, 1998. **23**(11): p. 861-863.
187. E.J. Heilweil, "Ultrashort-pulse multichannel infrared spectroscopy using broadband frequency conversion in LiIO3," Optics Letters, 1989. **14**(11): p. 551-553.

Danksagung

An erster Stelle möchte ich mich bei Herrn Prof. Dr. Marcus Motzkus bedanken. Seine Begeisterung für nichtlineare Mikroskopie und Impulsformung waren immer ansteckend und eine große Motivation. Des Weiteren wäre diese Arbeit in der vorliegenden Form ohne sein fachliches Wissen und seine Weitsicht nicht möglich gewesen. Sie hinterlassen sowohl fachlich als auch menschlich eine große Lücke an der Universität Heidelberg.

Ein großer Dank gilt auch Frau Prof. Dr. Annemarie Pucci für die Übernahme der Erstbegutachtung und für Ihre große Unterstützung in allen Belangen. Ich möchte mich zudem bei Herr Dr. Robert Moshammer für die Zweitbegutachtung bedanken.

Bei Prof. Dr. Ulrich Schwarz und Prof. Dr. Selim Jochim bedanke ich mich für die Bereitschaft, Teil meines Prüfungskomitees zu sein.

Ich möchte mich zudem besonders bei Dr. Tiago Buckup bedanken. Du hast durch dein fachliches Wissen maßgeblich zum Gelingen dieser Arbeit beigetragen. Vielen Dank für all die wissenschaftlichen als auch nicht-wissenschaftlichen Diskussionen, die Hilfe beim Schreiben von Manuskripten, die vielen neuen Ideen über Impulsformung und vieles mehr.

Zudem möchte ich mich bei meinem Vorgänger Dr. Lukas Brückner bedanken. Du hast mir in der kurzen gemeinsamen Zeit sehr geholfen mich schnell in das Experiment einzuarbeiten.

Ich bedanke mich auch bei Herrn Prof. Dr. Hans-Robert Volpp. Deine vielen interessanten Anekdoten werden mir im Gedächtnis bleiben.

Ein weiterer Dank geht an all die Begleiter der letzten drei Jahre. Ich möchte mich bei Nikolaus Wollscheid, Nicoló Alagna, Florian Nicolai, Dr. Zhuoran Kuang, Dr. Ashkan Roozbeh, Dr. Amiya Barik, Martin Maier, Oskar Kefer, Felix Hainer, Dr. Yang Li und Dr. Luis Lustres bedanken. Ich möchte mich für all die fachlichen Diskussionen und Hilfestellungen bedanken. Ich habe unsere gemeinsamen Freizeitaktivitäten und die gemeinsamen Mittagessen sehr genossen.

Ein weiterer Dank geht an Marina Sommer und Angelika Neuner für die geduldige Hilfe bei allem Organisatorischem. Des Weiteren möchte ich mich sowohl bei Uwe Branczyk und Gerhard Schodt für die Hilfe bei allen elektronischen Problemen als auch bei Klaus Schmitt und seinem ganzen Team in der Feinmechanikwerkstatt bedanken.

Ein Weiterer Dank geht an all meine Mitstreiter aus dem Physikstudium. Vielen Dank für die tolle Zeit. Obwohl so mancher Übungszettel uns einige schlaflose Nächte beschert hat, haben wir es gemeinsam doch immer hinbekommen. Ich bin sehr dankbar, dass wir uns weiterhin treffen und eine tolle Zeit gemeinsam haben.

Zuletzt möchte ich meiner ganzen Familie und insbesondere meiner Frau, Hanna Müller, danken. Danke für eure große Unterstützung und euren Rückhalt. Danke für euer Verständnis, wenn ich mit den Gedanken mal wieder noch im Labor war. Danke, dass ihr mir immer den Rücken freihaltet.